GDAŃSK UNIVERSITY
OF TECHNOLOGY
Technical Physics and Applied
Mathematics

The author of the PhD dissertation: Wojciech Mróz
Scientific discipline: physics

DOCTORAL DISSERTATION

Title of PhD dissertation: Photophysical processes in the selected white organic light-emitting diodes

Title of PhD dissertation (in Polish): Procesy fotofizyczne w wybranych organicznych białych diodach elektroluminescencyjnych

Supervisor W. Stampor *signature*	Second supervisor *signature*
dr hab. inż. Waldemar Stampor, prof. nadzw. PG	
Auxiliary supervisor *signature*	Cosupervisor Chiara Botta *signature*
	Ph.D. Chiara Botta

Gdańsk, year 2017

"There are three ways of gaining wisdom and knowledge:

By intellectual inquiry - the most noble,

By reproducing work of others - the most inferior,

And by experience - the most bitter."

...

1. ABSTRACT

The concept of present dissertation involves a discussion of photophysical processes occurring in the selected types of organic white light-emitting diodes (WOLEDs). Such devices are difficult to develop since the involvement of a variety of mechanisms governing their work has to be considered, such as the injection and transport of electrical charges of both signs, energy transfer processes, charge trapping, as well as the phenomena responsible for reduction of emission efficiency.

The thesis has been divided into two main parts. The first one presents in brief the history of investigation on electroluminescence of organic emitters and the state of the art of WOLEDs. Subsequently, the purpose and the scope of the work are listed. To give a reader a background for detailed description of the author's research, some physical phenomena determining the work of organic molecular systems are considered. As for technological aspects of fabrication of the WOLEDs, the types of their architectures are presented together with examples of functioning devices known from the literature. Finally, a description of technical parameters used for characterization of the light-emitting diodes has been included.

The second part has been based mainly on the author's own research. Chapter 7 describes the materials applied for the investigated WOLEDs and the details of the techniques used for preparation of the samples. Then, the measuring systems applied for examination of the samples are described. Finally, the author's experimental results are given in three subsequent sections of chapter 8.

In section 8.1 the results obtained for the OLEDs based on the emission from dendrons with pyrene antennae are presented. A dendronic part of the molecules serves in these devices as an emitter of blue and green light and, simultaneously, as an energy donor for the red emitting acceptor. The suitable chromophore concentration allowed to obtain white light as a combination of the emissions from the pyrene excimer and acceptor moiety.

Section 8.2 describes investigations on the diodes containing tetrakis β-diketonate complexes of terbium and europium and includes a discussion of the results received for a green OLED (with the terbium complex), a red one (containing the europium complex) and a system emitting white light. In this section the mechanism of energy transfer from materials forming the matrix of the white light emitting OLED to the europium complex is also discussed and diffusion coefficients of singlet excitons in the matrix together with lengths of their diffusion paths are determined.

In section 8.3 experiments on diodes with organic platinum complexes are presented. For the most efficient OLED the mechanisms responsible for a decrease in device quantum efficiency are discussed and the outcomes of measurements are compared with predictions of relevant theoretical models. As a result, the annihilation constant was determined for triplet-triplet annihilation process, being identified as the main reason for reduction of the quantum efficiency observed with increasing device current density. Finally, construction and characteristics of a double-layer WOLED employing monomer and excimer emission of the

platinum complex is described.

The thesis ends with a summary and conclusions together with two appendixes and a list of references.

2. CONTENTS

3. INTRODUCTION

In the first part of this chapter the milestones of organic electroluminescence are highlighted in order to give a reader the historical background of the field. Then the most perspective directions in current research of OLEDs are described and the state of the art of present WOLEDs, and also commercial products, are reported. Finally, few words about this thesis are given.

3.1. History of organic electroluminescence

The first electroluminescence (EL) from an organic dye was observed by Bernanose and co-workers in 1953 [1, 2] and since that time a magnificent improvement of materials and devices has been achieved allowing construction of light sources based on organic emitters which today are available commercially.

At first stage the research was focused on organic crystals due to high mobility values of at least one type of charge carriers in those materials as well as the well-known crystal structure, these features allowing a better understanding of device processes. The most important in that time, however, was a lack of other kinds of materials being suitable for successful construction of light-emitting devices. In 1963 the Pope's group observed electroluminescence from a single, pure crystal of anthracene and anthracene doped with tetracene. Nevertheless, the emission mechanism was ascribed to the field-accelerated electron excitation of the molecules [3].

The first reported observation of EL in organic crystal resulting from double injection recombination electroluminescence was made by Helfrich and Schneider with the use of anthracene crystal supplied with electron and hole injecting electrodes [4]. Yet, working with organic crystals had a big drawback from the applicative point of view: since their thickness was of the order of microns it was necessary to apply a potential difference of hundreds of volts to achieve the emission.

This obstacle has been removed by employment of small molecules which create amorphous layers during thermal evaporation process performed in vacuum. In 1987 Tang and VanSlyke published a famous paper describing the first organic light-emitting diode (OLED) based on a heterostructure [5]. The device utilized two organic layers: the hole transporting of diamine and the electron transporting and emitting one consisting of tris(8-hydroxyquinoline) aluminium(III) (Alq_3). This diode achieved 1% of the external quantum efficiency at operating voltage lower than 10V and luminance as high as 100 cd/m^2, paving a way to the commercial application of organic emitters. Two years later an OLED with a host-guest configuration was presented, constituting a concept being well established today *i.e.* the assignment of transporting and emissive functions to the properties of specialized materials [6]. Therefore, the well-transporting (but not necessary well-emitting) materials could be applied in such devices together with efficient dyes of not necessary good carrier transporting abilities. In this configuration a dye could be excited directly by charge trapping on emitting sites or indirectly by energy transfer from a matrix.

In the meantime, intensive research was performed on the polymers. The first EL from a polymer film of poly(N-vinylcarbazole) sandwiched between two charge injecting electrodes was reported by Partridge in 1983 [7-10]. In 1990 Burroughes *et al.* published their paper describing a device based on a 100 nm thick film of a green-light-emitting conjugated polymer poly(p-phenylene vinylene) of a decent efficiency [11]. The era of solution-processable large-area devices has started.

The above results made it possible to build the first white OLED (WOLED) having a reasonable efficiency (Kido and co-workers in 1994 [12]).

The next breakthrough took place in 1998 when Baldo *et al.* reported a diode with a phosphorescent emitter [13]. It should be noted that till that time all dyes used in devices were the fluorescent emitters, which limited their internal quantum efficiency up to 25% under electrical excitation, assuming a 100% emission quantum yield of a dye. With application of organometallic complexes containing a heavy atom with bonded organic ligands the spin-orbit coupling was introduced to the molecule which activated radiative transitions from the triplet states. In this way the emission of excitons having both multiplicities could be harvested in an electroluminescent device which in turn (for a perfectly efficient dye) increased the internal quantum efficiency of OLEDs up to 100%. Today, the best organic light-emitting diodes approach to their theoretical limits proving validity of this concept.

Few years ago a new class of efficient emitters was presented which utilize the thermally activated delayed fluorescence (TADF) [14-16]. In these materials the emission consists of prompt fluorescence and a delayed component, the latter originating from the reversed intersystem crossing from the triplet to singlet states. Such a transition is possible due to a small (≤ 0.1 eV) difference between the singlet and triplet levels, hence it can be activated by thermal energy. It is expected that emitters based on TADF mechanism will compete with phosphorescent emitters as dyes in OLEDs [17].

Another interesting approach employing the so-called hybridized excited state was presented recently in reference [18]. Such a kind of states represents a mixture of charge transfer (CT) component of small singlet-triplet energy splitting and locally excited (LE) state which in turn ensures high quantum yield of emission. By balancing the contributions of both types of components of the mixture a new class of materials has been created possessing advantages of both counterparts. It should be noted here that an emitter containing hybridized excited states exhibits emission mechanism different than that of an emitter based on TADF. In the latter case the prompt and delayed fluorescences are observed while for a dye with hybridized excited states the delayed component is absent.

Materials employing TADF and containing hybridized excited states reveal also their advantage when used as a host for fluorescent dyes. Particularly, since the emission of both singlets and triplets are harvested in such systems, energy of all excitons created in an emissive layer can be transferred to the dye molecules which allows to boost the internal quantum efficiency above the fluorescent-diode-theoretical limit being as high as 25%.

The efficiency of a device can be enhanced significantly if transition dipole moments of the emitter are oriented in its plane. In this way the creation of waveguide modes is avoided and more light can be outcoupled from an emitting structure. Though the arrangement of dipoles of luminescent molecules depends greatly on material utilized, it was shown in the literature that this concept has a great potential to improve light sources [19, 20].

3.2. White light organic sources - state of the art

In figure 3.1 luminous power efficacy progress in the academic research of organic lighting sources during years is presented. It is clear that WOLEDs built these days in laboratories possess higher efficiency than incandescent bulbs and even fluorescent lamps based on gas vapours, the record of luminous power efficacy belongs to Panasonic with 128 lm/W at 1000 cd/m^2 [21]. The main reasons why organic light sources still are not applied universally for the illumination purposes are high manufacturing costs related to small capacities of production lines and limitations of lifetime of the final products.

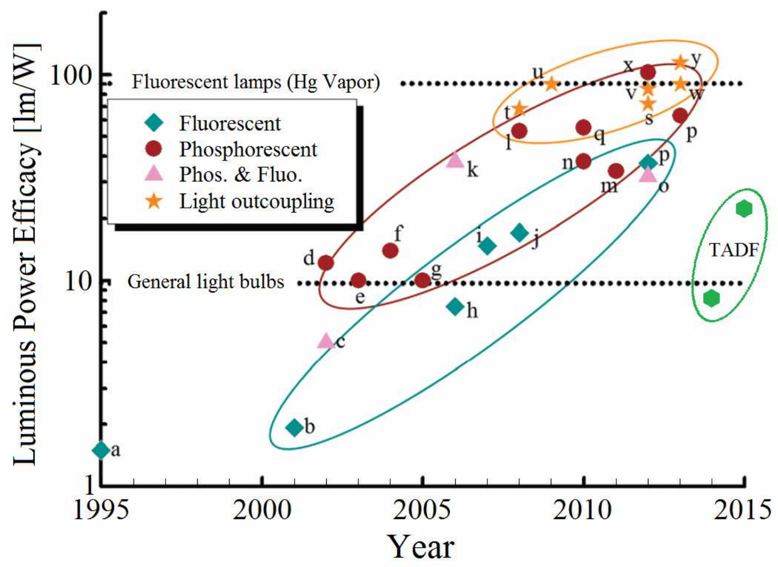

Figure 3.1. Progress in luminous power efficacy with different types of materials and techniques, for the meaning of each letter see [21]. Values for WOLEDs with TADF materials were taken from [22] and [23]

Despite the above, the quality of organic panels and also the quantity of the final products using them is constantly increasing. In table 3.1 the basic data of some commercially available organic light sources are gathered. The average luminous power efficacy now offered is around 45 lm/W, which is enough for some applications. Usually CCT of organic panels available today corresponds to warm hues of white.

The biggest white light-emitting panel offered to date is produced by LGChem with the emission area dimensions 300mm x 300mm. The same supplier provides flexible panels with the active area 41mm x 188mm and the bending radius of 30mm. COMEDD built sources able to emit light through bottom and top electrodes, which are transparent when the device is off.

Table 3.1 Performance data of commercially available organic panels

	Philips	LGChem	Lumiotec	MC Pioneer	OLEDWorks
Luminous power efficacy [lm/W]	40 - 50	55 - 80	27 - 40	31 - 52	45
LT70 [10^3 hrs]	10 - 50	30 - 50	5 - 60	8 - 20	10-20
CRI	80	90	80 - 90	84 - 87	>80
CCT [K]	3000, 4000	3000, 4000	2800, 4000, 4700	1200-6500*	3000, 3500

* These panels can change emission colour

The above few examples show that organic lighting sources start to enter a broad market and it is just a matter of time they conquer its significant part due to development of cheaper production methods and growth of efficiency. It will be a successful finish of the race that started more than sixty years ago.

3.3. About this thesis

This thesis has been divided into two main parts. The first one (chapters 3 - 6) introduces the reader in the world of WOLEDs, describes physical phenomena involved in OLEDs' operation, presents possible types of architectures of devices and the strategies to obtain white light, and finally gives a specification of parameters describing white light sources. The second part (chapters 7 and 8) is based on the work of the author (and co-workers) and presents three different approaches to obtain white light: fluorescence from dendrons with pyrene antennae, phosphorescence of lanthanide complexes of terbium and europium, and phosphorescence from organic platinum complexes exploiting monomer and excimer emission. In the last two cases theoretical models were applied to get a better understanding of the processes taking place in the devices and the parameters describing kinetics of the phenomena (the diffusion coefficients, the diffusion path lengths, the annihilation constants of excitons) were found.

A list below presents all publications of the author:

1. Giorgio Grisci, **Wojciech Mróz**, Marinella Catellani, Erika Kozma, Francesco Galeotti “Off-on fluorescence response of a cysteine-based perylene diimide for mercury detection in water” **Chemistry Select**, 1 (2016) 3033
2. Erika Kozma, **Wojciech Mróz**, Francesca Villafiorita-Monteleone, Francesco Galeotti, Marinella Catellani, Chiara Botta “Perylene diimide derivatives as red and deep red-emitters for fully solution processable OLEDs” **RSC Advances** 6 (2016) 61175
3. Giorgio Grisci, Erika Kozma, **Wojciech Mróz**, Katiuscia Pagano, Laura Ragona, Francesco Galeotti “Self-assembly of a water soluble perylene and surfactant into fluorescent supramolecular ensembles sensitive to acetylcholinesterase activity” **RSC Advances** 6 (2016) 64374

4. **Wojciech Mróz**, Marina Babushkina, Natalia Kushakova, Aleksei Kovalev, Olga Antonova, Vladislav Kaplin, Mariacecilia Pasini, Francesco Galeotti, Silvia Destri, Umbreto Giovanella, Irina Khotina “Hyperbranched 3D oligophenylenes for blue electroluminescence” **Mendeleev Comm.** 26 (2016) 347

5. Francesco Galeotti, **Wojciech Mróz**, Marinella Catellani, Bogmila Kutrzeba-Kotowska, Erika Kozma „Tailorable perylene-loaded fluorescent nanostructures: a multifaceted approach enabling application in white hybrid LEDs” **J. Mater. Chem. C** 4 (2016) 5407

6. Sagar Kesarkar, **Wojciech Mróz**, Marta Penconi, Mariacecilia Pasini, Silvia Destri, Patrizia R. Mussini, Clara Baldoli, Umberto Giovanella, Alberto Bossi “NIR-emitting Ir(III) complexes with heteroaromatic β-diketonate ancillary ligands for efficient solution processed OLEDs: structure-property correlations” **Angewandte Chemie Int. Ed.** 55 (2016) 2714

7. Erika Kozma, Giorgio Grisci, **Wojciech Mróz**, Marinella Catellani, Anita Eckstein-Andicsovà, Katiuscia Pagano, Francesco Galeotti “Water-soluble aminoacid functionalized perylene diimides: the effect of aggregationon the optical properties in organic and aqueous media” **Dyes and Pigments** 125 (2016) 201

8. Andrea Cappelli, Vincenzo Razzano, Giuseppe Fabio, Marco Paolino, Giorgio Grisci, Germano Giuliani, Alessandro Donati, Raniero Mendichi, **Wojciech Mróz**, Francesca Villafiorita-Monteleone, Chiara Botta “Side chain engineering in π-stacked polybenzofulvene derivatives bearing electron-rich chromophores for OLED applications” **RSC Advances** 5 (2015) 101377

9. Andrea Capelli, Vincenzo Razzano, Marco Paolino, Giorgio Grisci, Germano Giuliani, Alessandro Donati, Roberto Mendichi, Filippo Samperi, Salvatore Battiato, Antonella Boccia, Andrea Mura, Giovanni Bongiovanni, **Wojciech Mróz**, Chiara Botta “Bithiophene-based polybenzofulvene derivatives with high stacking and hole mobility” **Polymer Chemistry** 6 (2015) 7355

10. **Wojciech Mróz**, Roberta Ragni, Francesco Galeotti, Ernesto Mesto, Chiara Botta, Luisa De Cola, Gianluca Maria Farinola, Umberto Giovanella “Influence of electronic and steric effects of substituted ligands coordinated to Ir(III) complexes on the solution processed OLED properties” **J. Mater. Chem. C** 3 (2015) 7506

11. Giorgio Grisci, **Wojciech Mróz**, Umberto Giovanella, Katiuscia Pagano, William Porzio, Laura Ragona, Filippo Samperi, Simona Tomaselli, Francesco Galeotti, Silvia Destria “Acetylcholinesterase-induced fluorescence turn-off of an oligothiophene-grafted quartz surface sensitive to myristoylcholine” **J. Mater. Chem. B** 3 (2015) 4892

12. Francesco Galeotti, Erika Kozma, **Wojciech Mróz**, Bogumila Kutrzeba-Kotowska "Single-step shaping of fluorescent polymer beads by reverse breath figures approach" **RSC Advances** 5 (2015) 36315

13. Erika Kozma, **Wojciech Mróz**, Francesco Galeotti “A polystyrene bearing perylene diimide pendants with enhanced solid state emission for white hybrid light-emitting diodes” **Dyes and Pigments** 114 (2015) 138

14. **Wojciech Mróz**, Francesca Villafiorita-Monteleone, Mariacecilia Pasini, Giorgio Grisci, Marco Paolino, Vincenzo Razzano, Andrea Cappelli, and Chiara Botta “π-Stacked polybenzofulvene derivatives as hosts for yellow and red emitting OLEDs” **Mater. Lett.** 142 (2015) 197

15. Umberto Giovanella, Giuseppe Leone, Francesco Galeotti, **Wojciech Mróz**, Francesco Meinardi, Chiara Botta “FRET-assisted deep-blue electroluminescence in intercalated polymer hybrids” **Chem. Mater.** 26 (2014) 4572

16. Enrico Marchi, Mirko Locritani, Massimo Baroncini, Giacomo Bergamini, Riccardo Sinisi, Magda Monari, Chiara Botta, **Wojciech Mróz**, Marco Bandini, Paola Ceroni, Vincenzo Balzani “Blue and highly emitting [Ir(IV)] complexes by an efficient photoreaction of yellow luminescent [Ir(III)] complexes” **J. Mater. Chem. C** 2 (2014) 4461

17. Fabio Cucinotta, Aurélie Guenet, Claudia Bizzarri, **Wojciech Mróz**, Chiara Botta, Begoña Miliàn-Medina, Johannes Gierschner, Luisa De Cola “Energy transfer at the zeolite L boundaries: towards photo- and electroresponsive materials” **ChemPlusChem** 79 (2014) 45

18. **Wojciech Mróz**, Karol Falkowski, Maciej Miśnik, Ester Rossi, Marcella Balordi, Waldemar Stampor "Electromodulation of monomer and excimer phosphorescence in vacuum-evaporated films of platinum (II) complexes of 1,3-di(2-pyridyl)benzenes" **Org. Electron** 14 (2013) 2880

19. Francesco Galeotti, **Wojciech Mróz**, Guido Scavia, Chiara Botta "Microlens arrays for light extraction enhancement in organic light-emitting diodes: a facile approach" **Org. Electron.** 14 (2013) 212

20. Maciej Miśnik, Karol Falkowski, **Wojciech Mróz**, Waldemar Stampor "Electromodulation of photoluminescence in vacuum-evaporated films of bathocuproine" **Chem. Phys.** 410 (2013) 45

21. Andrea Cappelli, Marco Paolino, Giorgio Grisci, Germano Giuliani, Alessandro Donati, Raniero Mendichi, Antonella Caterina Boccia, Chiara Botta, **Wojciech Mróz**, Filippo Samperi, Andrea Scamporrino, Gianluca Giorni, Salvatore Vomero "Synthesis and characterization of charge-transporting π-stacked polybenzofulvene derivatives" **J. Mater. Chem.** 22 (2012) 9611

22. **Wojciech Mróz**, Chiara Botta, Umberto Giovanella, Ester Rossi, Alessia Colombo, Claudia Dragonetti, Dominique Roberto, Renato Ugo, Adriana Valore, J. A. Gareth Williams "Cyclometallated platinum(II) complexes of 1.3-di(2-pyridyl) benzenes for solution-processable WOLEDs exploiting monomer and excimer phosphorescence" **J. Mater. Chem.** 21 (2011) 8653

23. Francesco Galeotti, **Wojciech Mróz**, Alberto Bolognesi „CdTe nanocrystal assemblies guided by breath figure templates" **Soft Matter** 7 (2011) 3832

24. Alberto Bolognesi, Francesco Galeotti, **Wojciech Mróz**, Valeria Gancheva, Levon Terlemezyan "Towards semiconducting graft copolymers: switching from ATRP to "Click" approach" **Macromol. Chem. Phys.** 211 (2010) 1488

25. Umberto Giovanella, **Wojciech Mróz**, Paolo Foggi, Pierangelo Fabbrizzi, Stefano Cicchi, Chiara Botta „Multi-colour electroluminescence of dendronic antennae containing pyrenes as light harvesters" **ChemPhysChem** 11 (2010) 683

26. Jakub Mężyk, **Wojciech Mróz**, Agnieszka Mech, Umberto Giovanella, Francesco Meinardi, Chiara Botta, Barbara Vercelli, Riccardo Tubino, "Diffusion-mediated resonant energy transfer in lanthanide-based polymer white light emitting diodes" **Phys. Chem. Chem. Phys.** 11 (2009) 10152

27. **Wojciech Mróz**, Jean Philippe Bombenger, Chiara Botta, Alessio Orbelli Biroli, Maddalena Pizzotti, Filippo De Angelis, Leonardo Belpassi, Riccardo Tubino, Francesco Meinardi "Oligothiophenes nano-organized on a cyclotetrasiloxane scaffold as a model of a silica-bound monolayer: evidence for intramolecular excimer formation" **Chem. Eur. J.** 15 (2009) 12791

28. Waldemar Stampor, **Wojciech Mróz**, "Electroabsorption in triphenylamine-based hole-transporting materials for organic light-emitting diodes" **Chem. Phys.** 331 (2007) 261

4. ELECTRONIC EXCITED STATES IN ORGANIC MOLECULAR SYSTEMS - THEIR CREATION AND PATHS OF DECAY

In this chapter basic physical concepts involved in operation of organic light-emitting diodes are described.

4.1. Conjugation in organic molecules

We start from a description of the electronic structure of a conjugated organic system. An example is benzene molecule consisting of six carbon atoms arranged in a ring, shown in figure 4.1. A carbon atom in the ground state possesses six electrons organized as $1s^2 2s^2 2p^2$. In benzene molecule the atomic orbitals of neighbour carbon atoms overlap each other creating chemical bonds. 2*s* orbital is mixed with p_x and p_y (all in the plane of the molecule) creating three new hybridized sp^2 orbitals. Two of such orbitals originating from two near carbon atoms overlap with each other forming a strong σ-bond between adjacent atoms and in this way fixing the ring configuration of the molecule. Remaining sp^2 orbital binds hydrogen atom to the benzene ring.

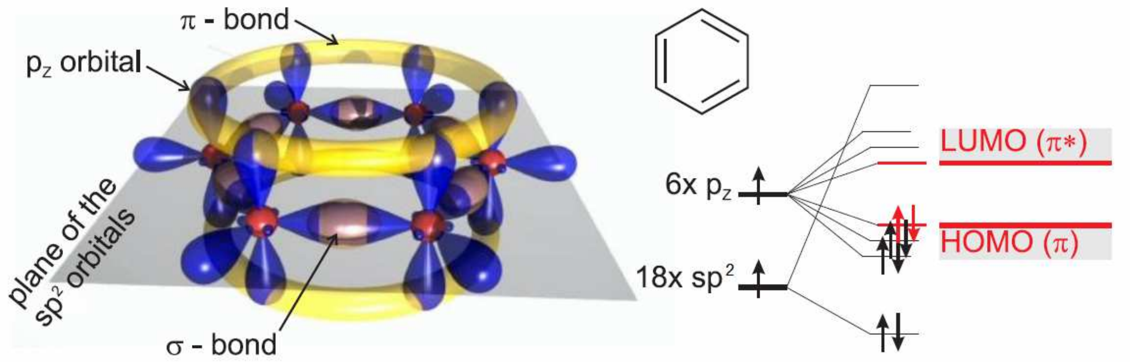

Figure 4.1. Benzene molecule structure, its molecular orbitals and electronic energy levels [24]

The p_z orbital extends perpendicularly above and below the plane of benzene molecule. The orbital from each atom again overlaps with the ones next to them, creating π-bond. Since this bond type is relatively weak, it allows a delocalisation of the electron distribution around all benzene ring, giving rise to the conjugated π-electron system.

Let us consider a molecular system consisting of two atoms. We can define it by the linear combination of atomic orbitals $\phi_a(\vec{r})$ and $\phi_b(\vec{r})$. Since there can be constructive or destructive interference of atomic orbitals, we obtain two possible terms describing the molecule

$$\Phi_+ = N_+\left[\phi_a(\vec{r}) + \phi_b(\vec{r})\right], \qquad \Phi_- = N_-\left[\phi_a(\vec{r}) - \phi_b(\vec{r})\right]. \tag{4.1}$$

Now we calculate the electron orbital density for the both cases

$$P_+ = \left|\Phi_+\right|^2 = N_+^2\left[\phi_a^2\left(\vec{r}\right) + \phi_b^2\left(\vec{r}\right) + 2\phi_a\left(\vec{r}\right)\phi_b\left(\vec{r}\right)\right], \tag{4.2a}$$

$$P_- = \left|\Phi_-\right|^2 = N_-^2\left[\phi_a^2\left(\vec{r}\right) + \phi_b^2\left(\vec{r}\right) - 2\phi_a\left(\vec{r}\right)\phi_b\left(\vec{r}\right)\right]. \tag{4.2b}$$

We notice that P_+ has higher value than the sum $\phi_a^2\left(\vec{r}\right) + \phi_b^2\left(\vec{r}\right)$ of densities of separate atomic orbitals, which makes Φ_+ energetically more favourable and so a bonding orbital. On the other hand, P_- is smaller than the sum and thereby Φ_- orbital is of antibonding character. The product $\phi_a\left(\vec{r}\right)\phi_b\left(\vec{r}\right)$ is called the overlap density.

Though the above example is very simple, it sustains its validity for more complex molecules. Therefore, in benzene and other organic molecules a splitting into bonding and anti-bonding orbitals is also observed. Because p_z carbon orbitals overlap less with themselves as compared to sp^2 orbitals, the splitting between the π bonding and π* anti-bonding orbitals is smaller than between the σ and σ*. As a consequence, in most conjugated organic compounds the highest occupied molecular orbital (HOMO) is the π orbital and the lowest unoccupied molecular orbital (LUMO) is the π* orbital (see fig. 4.1).

4.2. Multiplicity of states

Upon excitation of a molecular system unpaired electrons from π and π* orbitals create a two-particle system. Electrons have the angular momentum quantum number (spin) s=1/2 and from the above we conclude there are two possible values of the spin magnetic quantum number: m_s= 1/2 and m_s= -1/2. We denote the state of single electron $\left|s, m_s\right\rangle$ = $\left|1/2, +1/2\right\rangle$ as α, while the state $\left|1/2, -1/2\right\rangle$ as β.

Considering two particles we denote the total spin of a system as S and the spin magnetic quantum number as M_s. For the system under discussion we get the singlet (S=0) state in the form of spin wavefunctions

$$\frac{1}{\sqrt{2}}\left\{\alpha_1\beta_2 - \beta_1\alpha_2\right\} \tag{4.3}$$

and three triplet (S=1) states:

$$\beta_1\beta_2 \qquad \text{for } M_s=-1, \tag{4.4}$$

$$\frac{1}{\sqrt{2}}\left\{\alpha_1\beta_2 + \beta_1\alpha_2\right\} \qquad \text{for } M_s=0, \tag{4.5}$$

$$\alpha_1\alpha_2 \qquad \text{for } M_s=1. \tag{4.6}$$

The indexes of α and β refer to particle 1 and 2. We notice that for the case S=0 there is only one value of M_s=0 and as a consequence this arrangement is called singlet. If S=1 there are three possible values of M_s = -1, 0, 1 and therefore the name triplet is assigned. A vectorial representation of the system is shown in fig. 4.2.

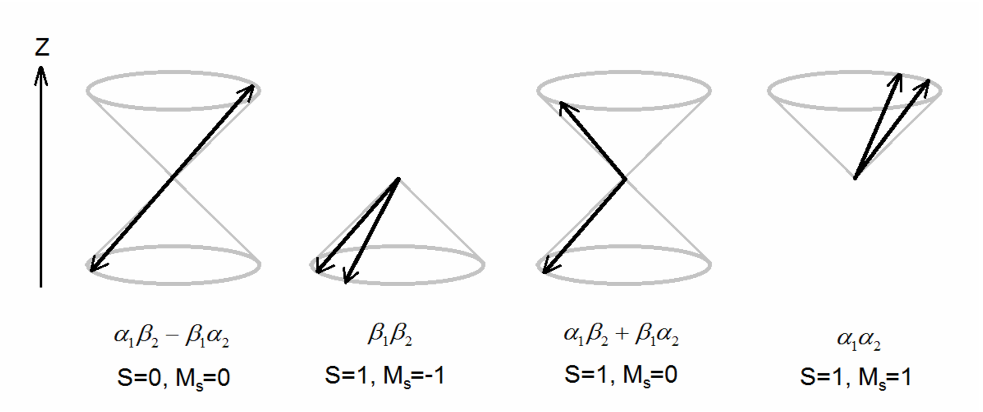

Figure 4.2. Vector diagram showing orientations of two electron spins for singlet and triplet states

In singlet state spins are 180° out of phase ("-" in formula 4.3) while for triplet states they are always in phase.

4.3. Singlet and triplet energy levels

After we have defined the HOMO and LUMO energy levels of a molecule as well as their singlet and triplet configurations, now we are able to determine the mutual position of the energy levels of singlet and triplet states. We introduce two quantities, the first one is named the Coulomb integral

$$J_{ia} = \frac{e^2}{4\pi\varepsilon_0}\iint \psi_i^*(r_1)\psi_a^*(r_2)\left(\frac{1}{r_{12}}\right)\psi_i(r_1)\psi_a(r_2)d^3r_1d^3r_2 \tag{4.7}$$

and describes the total contribution to the potential energy arising from a hole $-e\left|\psi_i(r_1)\right|^2$ and an electron $-e\left|\psi_a(r_2)\right|^2$ in the two orbitals. The second quantity is the exchange integral

$$K_{ia} = \frac{e^2}{4\pi\varepsilon_0}\iint \psi_i^*(r_1)\psi_a^*(r_2)\left(\frac{1}{r_{12}}\right)\psi_a(r_1)\psi_i(r_2)d^3r_1d^3r_2\,, \tag{4.8}$$

describing quantum mechanical correction to the Coulomb integral.

It can be shown that the energy corresponding to the orbital wavefunctions symmetric under the particle interchange is [25]

$$E_S = J_{ia} + K_{ia}\,, \tag{4.9}$$

while for the orbital wavefunctions that are antisymmetric under the interchange of the names of electrons is equal to

$$E_T = J_{ia} - K_{ia}\;. \tag{4.10}$$

It is known that singlets have the symmetric orbital wavefunctions states and the antisymmetric orbital wavefunctions states are ascribed to triplets, thus we conclude that E_S determines the energy of singlet state and E_T describes the triplet state energy. Because J_{ia} and K_{ia} are both positive quantities, the energy of the triplet state is lower than the energy of the singlet state. From the above we can also see that the energy difference between the singlet and the triplet level of a molecule is proportional to the double exchange integral

$$\Delta E_{ST} = 2K_{ia}\,. \tag{4.11}$$

Since the exchange integral describes overlap of the HOMO and LUMO, the smaller overlap between the orbitals the smaller the difference in energy between the singlet and the triplet state of the molecule.

4.4. The Jablonski diagram

In figure 4.3 the Jablonski diagram is presented, showing most of possible photophysical processes in an isolated molecule. After photon absorption the molecule goes from the electronic ground state S_0 to the electronic excited state or its vibrational level. Since typically the ground state possesses singlet multiplicity, only transitions to the singlet excited states are allowed due to the multiplicity conservation rule. In the case of highly phosphorescent materials, the transition $S_0 \rightarrow T_n$ is possible but still is much less efficient than between singlet states. On the other hand, if the molecule is in the first triplet excited state T_1, transitions to the higher triplet states are allowed (T-T absorption).

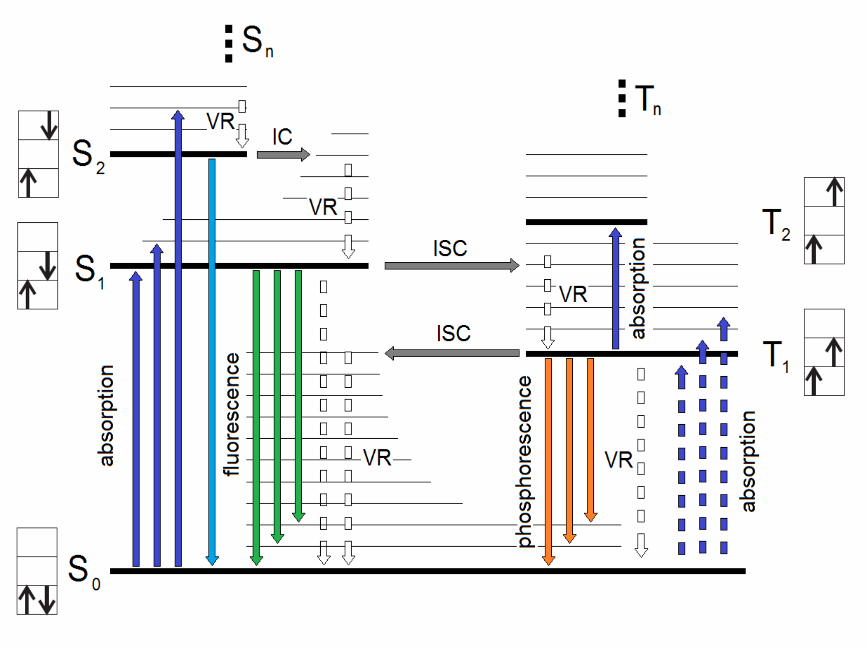

Figure 4.3. The Jablonski diagram

Once the molecule is in the vibrationally "hot" electronic excited state, vibrational relaxation (VR) occurs finishing on the lowest vibrational level of the excited state. Vibrational relaxation is a very fast process (10^{-12} s) and during transitions to lower vibrational levels the energy is dissipated to the surroundings of the molecule. When the molecule is in the lowest vibrational level of the excited state three competitive processes may occur.

The first one is a transition to the ground state with simultaneous photon emission. Depending on whether the transition is between the states of the same or different multiplicity, the decay to the ground state $S_1 \rightarrow S_0 + h\nu$ is called fluorescence, while $T_1 \rightarrow S_0 + h\nu$ is phosphorescence, respectively. Fluorescence is a fast process (10^{-9} s), while phosphorescence requires much longer time (10^{-6} - 10^{-3} s).

The second possible process is the intersystem crossing (ISC), *i.e.* a radiationless, isoenergetic transition between the states having different multiplicity. The transition rules forbid this path, but at favourable conditions like vibronic coupling or presence of a heavy atom, the ISC becomes partially allowed.

The third possibility is the internal conversion (IC) from the ground vibrational level of the higher excited state to the hot vibrational level of the lower excited state (both having the same multiplicity). This nonradiative process is much faster (10^{-12} s) than a radiative decay to the electronic ground state. As a consequence, excited molecules typically relax *via* IC and VR to the lowest vibrational levels of the lowest electronic exited state before photon emission (Kasha's rule). However, it still may happen that a molecule being in the lowest excited state will relax vibrationally to the ground state rather than emit photon. This is typically the case if an excitation of a fluorescent molecule was transferred by the ISC process to the first excited triplet level.

4.5. Quantum yield of photoluminescence

Perhaps the most important quantity describing any emitter is its quantum yield (η_{PL}), defined as the ratio of the number of emitted photons to the number of photons that were absorbed. The quantum yield can also be derived on the basis of the Jablonski diagram as the ratio of the radiative rate constant k_r to the sum of the rate constants of all decay pathways

$$\eta_{PL} = \frac{k_r}{k_r + k_{nr}}, \tag{4.12}$$

where k_{nr} denotes the total rate constant for nonradiative decay that depopulates the excited states without emission of photons.

4.6. Excitons

Excitation in a molecular material may transfer an electron from one site into another one at various distances. Depending on the intermolecular interactions, holes and electrons created in this way become either free carriers or excitons, *i.e.* a bound state of a hole and an electron, which are attracted to each other by the Coulomb force. Three types of excitons are observed, depending on their radius, as shown in figure 4.4. The type of an exciton is determined by properties of the material in which it has been created.

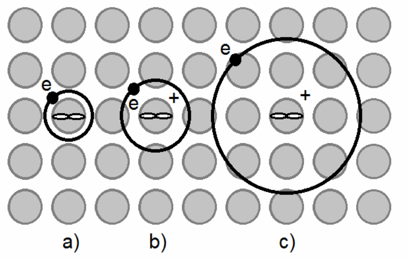

Figure 4.4. Classification of excitons: a) Frenkel exciton, b) charge-transfer exciton, c) Mott-Wannier exciton

In inorganic semiconductors atoms are linked by strong covalent or ionic bonds. Consequently, the valence and conductive bands are wide and charge carriers may travel within them without scattering at long distances (of many lattice constants). Moreover, these materials possess dielectric constants ε_r of the order of 10. Due to the high dielectric constant, the value of the coulombic capture radius

$$r_c = \frac{e^2}{4\pi\varepsilon_0\varepsilon_r kT}, \tag{4.13}$$

defined as the distance at which the coulombic bonding energy is equal to kT, is small at room temperature. For example, at 295K the capture radius is 4.7 nm in crystalline silicon ($\varepsilon_r = 12$). At distances higher than r_c a hole and an electron become free charge carriers. As a result, in inorganic semiconductors free holes in a valence band and free electrons in a conductive band are created at room temperature. With temperature decreasing the coulombic capture radius increases allowing a formation of weakly bound, large radius Mott-Wannier excitons. For example, in GaAs (ε_r = 13) the bonding energy is equal to 4.2 meV at ~2K [26] and the coulombic capture radius is 26 nm.

In organic solids the situation is fundamentally different. Weak van der Waals forces between the molecules lead to narrow valence and conductive bands in crystals or even lack of bands in amorphous materials. In consequence, the physical properties of molecular organic solids are similar to the properties of molecules they are built of. Dielectric constant of organic materials is typically 3 ÷ 4 which determines rather considerable coulombic capture radius. For a material having $\varepsilon_r = 3$, the coulombic capture radius is 19 nm at T = 295K. Because of the reasons mentioned above the electronic excitations in organic materials have a form of tightly bound excitons. In the case that an exciton resides on the molecule it is called Frenkel exciton, after Yakov Frenkel, who proposed such a concept in 1931 [27]. If an electron - hole pair is localized at the adjacent molecules the exciton is classified as the charge transfer one.

In organic materials the distance between a hole and an electron in the exciton is small, which provides strong overlap of their wavefunctions. This determines significant values of the exchange energy (formula 4.8) and, consequently, the spin of charge carriers that create the exciton is of high importance in these materials. In inorganic solids the radius of exciton is significant and the difference between the singlet and triplet energy levels is negligible.

All types of excitons are able to move through a solid and, consequently, to transport energy. In typical organic materials at room temperature the exciton movement takes a form of hops from one molecule to the adjacent one. From hereafter we define this type of energy transfer as the diffusion mediated energy transfer, in opposite to the other types of energy transfer that are defined below.

4.7. Mechanisms of energy transfer

The first energy transfer mechanism we discuss is a trivial case of reabsorption of an emitted photon by another molecule

$$D^* \to D + h\nu$$

$$h\nu + A \to A^*,$$

where *D* and *A* are the energy donor and the energy acceptor, respectively, and asterisk denotes the excited state. Probability of radiative energy transfer between two different or the same molecules (energy migration) is given approximately by formula [28]

$$k_{ET}^{rad} \approx \frac{2.303 c_A x}{\eta_{PL}^{D}} \int_0^\infty f_D(\bar{\nu}) \varepsilon_A(\bar{\nu}) d\bar{\nu}, \tag{4.14}$$

where c_A is the molar concentration of acceptors, x is the specimen thickness, η_{PL}^{D} denotes the quantum yield of the donor and $f_D(\bar{\nu})$ and $\varepsilon_A(\bar{\nu})$ stand for the emission spectrum of the donor and the absorption spectrum of the acceptor, respectively. Except this two-step energy transfer process mediated by photons another two single-step energy transfer mechanisms exist which are frequently present in organic materials.

The Förster-type resonant dipole-dipole long range energy transfer is a radiationless phenomenon shown schematically in figure 4.5. To occur it requires that the emission spectrum of a donor overlaps the absorption spectrum of an acceptor, however the overlap of their wavefunctions is not necessary.

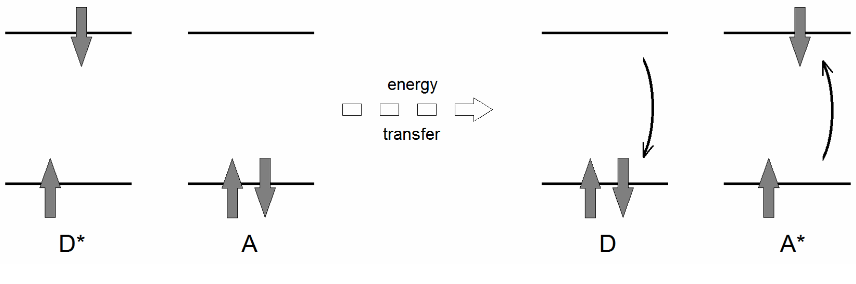

Figure 4.5. The Förster-type energy transfer. Thick arrows represent spins at the ground and the exited state of molecules

In this process the spin is not changed in either participant. Therefore, following transitions

$$^1D^* + {}^1A \to {}^1D + {}^1A^* \text{ and}$$

$$^1D^* + {}^3A \to {}^1D + {}^3A^*$$

are allowed. The rate constant of transfer process is described by formula [29, 30]

$$k_{ET}^{Forster} = \frac{9(\ln 10)\kappa^2}{128\pi^5 n^4 N_A \tau_D^i R^6} \int_0^\infty \frac{f_D(\bar{\nu})\varepsilon_A(\bar{\nu})}{\bar{\nu}^4} d\bar{\nu}\,, \tag{4.15}$$

where $\bar{\nu}$ is the wavenumber, n - the refractive index of the environment, N_A - Avogadro's number, τ_D^i - the intrinsic (radiative) lifetime of the excited donor, R - the distance between the donor and the acceptor, $\varepsilon_A(\bar{\nu})$ - the acceptor extinction coefficient (in cm^{-1}M^{-1}), $f_D(\bar{\nu})$ - the normalized spectral distribution of the donor's luminescence $\left(\int_0^\infty f_D(\bar{\nu})d\bar{\nu} = 1\right)$ and κ^2 the orientation factor. For an isotropic distribution of dipoles κ^2=2/3.

Formula (4.15) can be rewritten in a different form as

$$k_{ET}^{Forster} = \frac{1}{\tau_D}\left(\frac{R_0}{R}\right)^6, \tag{4.16}$$

where τ_D is the mean lifetime of the donor (in the absence of energy transfer), being connected with the donor PL quantum yield, η_{PL}^D, and the intrinsic lifetime by $\tau_D = \eta_{PL}^D \cdot \tau_D^i$. R_0 is the Förster radius

$$R_0^6 = \frac{9(\ln 10)\kappa^2 \eta_{PL}^D}{128\pi^5 n^4 N_A} \int_0^\infty \frac{f_D(\bar{\nu})\varepsilon_A(\bar{\nu})}{\bar{\nu}^4} d\bar{\nu}\,. \tag{4.17}$$

The Förster radius corresponds to the distance at which the excitation transfer and all other competing deactivation processes are equally probable. Although the energy transfer depends on the sixth power of the distance, it is usually relevant up to 100Å.

The second possibility of single-step energy transfer is known as the Dexter-type transfer. Since it is based on an exchange of electrons between a donor and an acceptor, in addition to the spectral overlap of the donor emission and the acceptor absorption, the overlap of their wavefunctions is also required. Therefore, the proximity of energy transfer participants is necessary and the Dexter transfer operates in the range 10 ÷ 20Å.

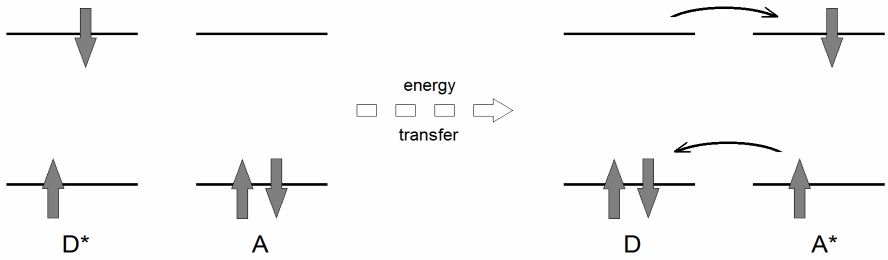

Figure 4.6. Dexter-type energy transfer

In figure 4.6 the process of Dexter energy transfer is shown schematically. Differently than in the Förster-type energy transfer where the spin of the donor and acceptor is unchanged, in the Dexter exchange energy transfer only the total spin of the system is conserved, therefore a transfer of singlets and triplets between molecules is possible

$$^1D^* + {}^1A \rightarrow {}^1D + {}^1A^*$$

$$^3D^* + {}^1A \rightarrow {}^1D + {}^3A^* .$$

For the transfers between the states with allowed transitions (with the donor and the acceptor as singlet states), the Dexter transfer is typically overwhelmed by the longe-range Förster process. The rate constant of the exchange energy transfer is given by

$$k_{ET}^{Dexter} = A \exp\left(-\frac{2R_{DA}}{L}\right)\int_0^\infty f_D(\bar{\nu})\varepsilon_A(\bar{\nu})d\bar{\nu} , \tag{4.18}$$

where *A* is the constant related to the specific orbital interactions, $f_D\left(\bar{\nu}\right)$ is the normalized emission spectrum of the donor, $\varepsilon_A\left(\bar{\nu}\right)$ is the normalized absorption spectrum of the acceptor and R_{DA} is the donor-acceptor separation relative to the effective average Bohr radius of the excited donor and unexcited acceptor states, *L* [31, 32].

4.8. Excimers

Till now we have considered excited states created in organic solids involving mainly a single molecule. However, in a material composed of identical molecules bimolecular excited states may be also present due to resonant interactions between the excited molecule and the neighbour molecule in the ground state. Such new states are called excimers. Resonant interaction between the molecules creating an excimer has both energy exchange contribution and charge exchange character. The first mechanism leads to the locally-excited excimers (local or LE excimers) while the second one to the charge-transfer excimers (CT excimers). The existence of excimer possessing only one type of resonance is not possible [28], therefore a contribution of each term is described by the amplitudes *a* and *b* (formula 4.19). Excimers may have either singlet or triplet multiplicity.

$$^{1,3}\left|M^*M\right\rangle_{excimer} = a_1\,^{1,3}\left|M_1^*M_2\right\rangle + a_2\,^{1,3}\left|M_1M_2^*\right\rangle + b_1\,^{1,3}\left|M_1^+M_2^-\right\rangle + b_2\,^{1,3}\left|M_1^-M_2^+\right\rangle = \tag{4.19}$$

$$a^{1,3}\left|M^*M\right\rangle_{loc} + b^{1,3}\left|M^+M^-\right\rangle_{CT}$$

The intrinsic property of excimers is that they are dimers which are associative in an electronic excited state but dissociative in the ground state. In figure 4.7 the potential well of a bound excimer and the repulsive potential of the ground state are shown. Such a shape of the potential energy curves determines the excimer emission spectrum being typically observed as a broad featureless band red-shifted with respect to the monomer emission.

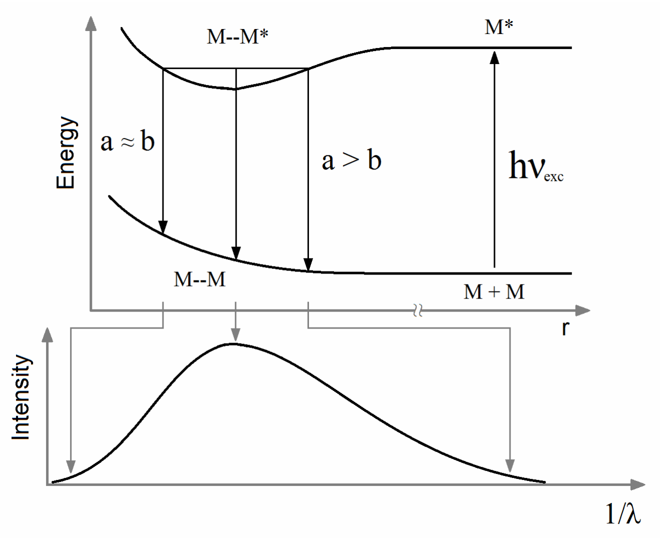

Figure 4.7. The potential energy curves of molecules M creating an excimer (top), the emission spectrum of the excimer (bottom). Letters *a* and *b* are the amplitudes from formula (4.19)

The higher energy transitions of the excimer emission correspond to larger influence of the local excimer ($a > b$), while the lower energy transitions correspond to substantial contribution of CT excimer ($a \approx b$). Since the excimers do not exist in the ground state, a transition from the ground to the excited state, *i.e.* absorption, is not observed for these species. Usually excimers possess low quantum yields due to increased radiationless relaxation introduced by phonons interacting with an extended bi-molecular system and due to the small overlap of proper wavefunctions of the excited and the ground states of excimer forming molecules (Fermi's golden rule).

Excimer formation requires a close proximity of molecules, typically of 3 ÷ 4 Å, above this distance they lose their excimer features.

4.9. Exciplexes

Bimolecular excited states can be created not only between identical molecules but also with participation of two different ones. Such a two-component system is called exciplex. Typically, such states are easily created in blends composed of electron donor and electron acceptor molecules. An example is shown in figure 4.8 presenting the energy levels of polymer TPD (donor), PBD (acceptor) and exciplex formation mechanism.

Like excimers, exciplexes possess a mixed character of energy and charge resonance (see formula 4.19) and a high proximity of participating molecules is necessary to create such states. Emission spectrum is again a broad, structureless band red-shifted from the monomer spectra of the donor and the acceptor. An example of the emission spectrum of electrically excited exciplex is presented in figure 4.9. Other authors obtained similar results for the same molecules [33].

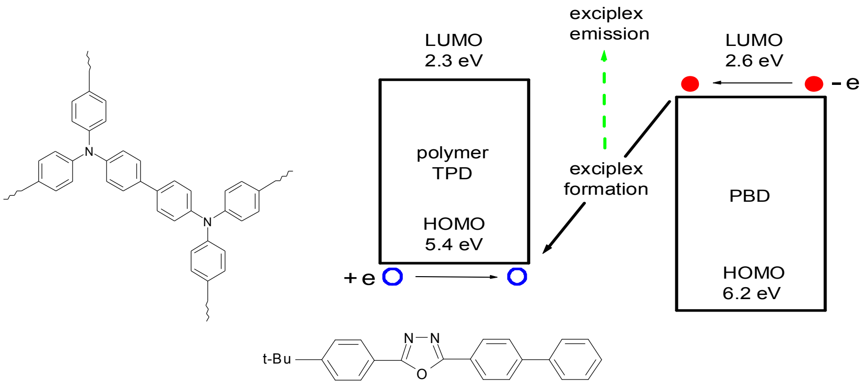

Figure 4.8. Exciplex formation mechanism for polymer TPD donor and PBD acceptor

Emission maximum of an exciplex can be calculated from the relation between the electron affinity of the acceptor (E_a), the ionization energy of the donor (E_i) and the Coulombic energy of attraction between an electron and a hole (E_c)

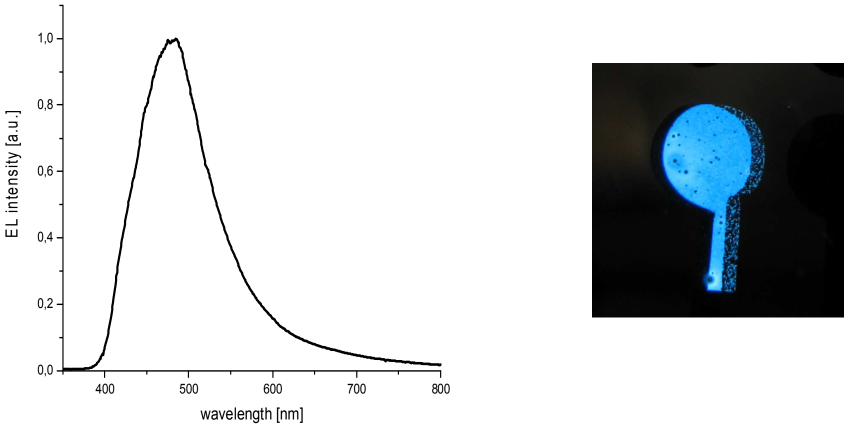

Figure 4.9. Electroluminescence spectrum of 65% polymer TPD : 35% PBD device at 5V (left). A photograph of the emitting device (right)

$$h\nu_{exciplex}^{\max} \approx E_i - E_a - E_c, \tag{4.20}$$

$$E_c = \frac{e^2}{4\pi\varepsilon_0 \varepsilon r}. \tag{4.21}$$

Formula (4.20) is derived under the assumption of a dominant role of the charge transfer terms in formula (4.19).

4.10. Spin-orbit coupling

Interaction between the magnetic moment created by an oscillating electron in an orbit and spin of the same electron is called the spin-orbit coupling and is responsible for enhanced intersystem crossing between the singlet and triplet states. The energy of interaction between the magnetic field generated by an electron, $\vec{B}$, and a magnetic dipole, $\vec{m}$, has a form of $-\vec{m}\cdot\vec{B}$. Since magnetic field is created by an electron oscillating in the circular orbit it can be related to the angular momentum $\vec{l}$ of the electron and, as a consequence, the spin-orbit interaction is proportional to $\vec{l}\cdot\vec{s}$. It can be shown that the hamiltonian of spin-orbit interaction has a form [25]

$$H_{so} = \frac{e}{2m_e^2 rc^2}\frac{d\phi}{dr}\vec{l}\cdot\vec{s}, \tag{4.22}$$

where *e* is the elementary charge, m_e denotes the mass of an electron, *r* stands for the orbit radius, *c* denotes the speed of light and $\phi(r)$ designates the isotropic potential. For hydrogenic atom, the potential of a nucleus carrying *Ze* charge is $\phi = Ze/4\pi\varepsilon_0 r$. After substitution we obtain

$$H_{so} = -\frac{Ze^2}{8\pi\varepsilon_0 m_e^2 r^3 c^2}\vec{l}\cdot\vec{s}. \tag{4.23}$$

The expectation value of r^{-3} for hydrogenic orbitals is proportional to Z^3 thus finally we get

$$H_{so} = -\frac{Z^4 e^2}{8\pi\varepsilon_0 m_e^2 c^2}\vec{l}\cdot\vec{s}. \tag{4.24}$$

We notice that the spin-orbit coupling is proportional to Z^4 and, consequently, is much more significant in heavy atoms.

Now we show an example of how spin-orbit interaction mixes singlet and triplet states in a two electron configuration. We write

$$H_{so} = \xi_1\vec{l_1}\cdot\vec{s_1} + \xi_2\vec{l_2}\cdot\vec{s_2} =$$

$$\frac{1}{2}\left(\xi_1\vec{l_1} + \xi_2\vec{l_2}\right)\cdot\left(\vec{s_1} + \vec{s_2}\right) + \frac{1}{2}\left(\xi_1\vec{l_1} - \xi_2\vec{l_2}\right)\cdot\left(\vec{s_1} - \vec{s_2}\right). \tag{4.25}$$

Since the $\vec{s_1} + \vec{s_2}$ operator commutes with the total spin operator, S^2, it cannot mix states of different multiplicity. On the other hand, the $\vec{s_1} - \vec{s_2}$ operator does not commute with S^2 and so this component of the operator is responsible for the singlet-triplet mixing. Therefore, we consider

$$\left\langle 1, M_s \middle| H_{so} \middle| 0,0 \right\rangle = \frac{1}{2}\left\langle 1, M_s \middle| \left(\xi_1\vec{l_1} - \xi_2\vec{l_2}\right)\cdot\left(\vec{s_1} - \vec{s_2}\right) \middle| 0,0 \right\rangle. \tag{4.26}$$

The *z*-component of the spin operator, $s_{1z} - s_{2z}$, is relevant and its action is to convert a singlet to a M_S=0 triplet state as follows

$$\left(s_{1z} - s_{2z}\right)\left|0,0\right\rangle = \left(s_{1z} - s_{2z}\right)\frac{1}{\sqrt{2}}\left\{\alpha_1\beta_2 - \beta_1\alpha_2\right\} = \frac{\hbar}{\sqrt{2}}\left\{\frac{1}{2}\alpha_1\beta_2 + \frac{1}{2}\beta_1\alpha_2 + \frac{1}{2}\alpha_1\beta_2 + \frac{1}{2}\beta_1\alpha_2\right\} =$$

$$= \frac{\hbar}{\sqrt{2}} \{\alpha_1\beta_2 + \beta_1\alpha_2\} = \hbar |1,0\rangle \tag{4.27}$$

The remaining orbital operator part of the spin-orbit coupling hamiltonian is

$$\langle 1,0|H_{so}|0,0\rangle = \frac{\hbar}{2}(\xi_1 l_{1z} - \xi_2 l_{2z}). \tag{4.28}$$

4.11. Emission mechanisms in β-diketonate complexes containing $Tb^{3+}$and Eu^{3+}

Terbium and europium belong to a group of elements named lanthanides, their position in the periodic table is in the "footnote", *c.f.* figure 4.10. Lanthanides are unique among other elements (except actinides) in resembling so much each other. This is well understood on the basis of electronic configuration of their ions which essentially exist in the trivalent state Ln^{III} ([Xe] $4f^n$, $n = 0 \sim 14$). Since the outer filled 5p and 5s shells effectively shield the inner 4f shell from surroundings, the last one does not play a role in chemical bonding between an ion and a matrix or organic ligand. In consequence, transitions within the 4f shell of a lanthanide (organic) complex are similar to those of a free ion. In figure 4.11 interactions within the lanthanide ion that split energy levels are shown, using as an example Eu^{3+}.

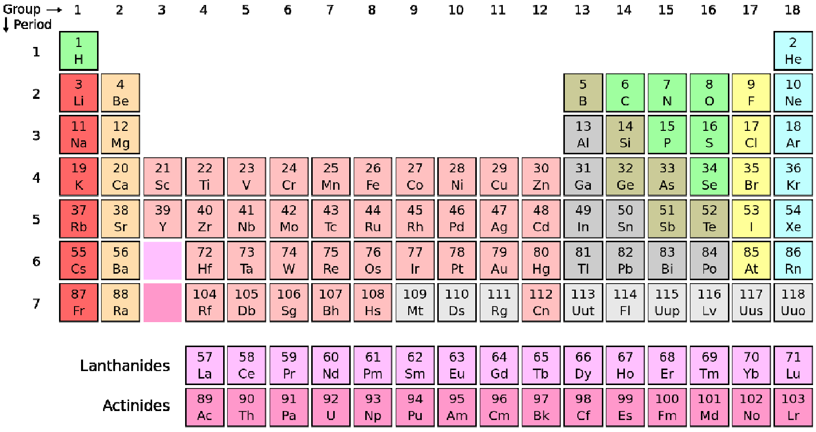

Period	1	2	3	4	5	6	7	8	9	10	11	12	13	14	15	16	17	18
1	1 H																	2 He
2	3 Li	4 Be											5 B	6 C	7 N	8 O	9 F	10 Ne
3	11 Na	12 Mg											13 Al	14 Si	15 P	16 S	17 Cl	18 Ar
4	19 K	20 Ca	21 Sc	22 Ti	23 V	24 Cr	25 Mn	26 Fe	27 Co	28 Ni	29 Cu	30 Zn	31 Ga	32 Ge	33 As	34 Se	35 Br	36 Kr
5	37 Rb	38 Sr	39 Y	40 Zr	41 Nb	42 Mo	43 Tc	44 Ru	45 Rh	46 Pd	47 Ag	48 Cd	49 In	50 Sn	51 Sb	52 Te	53 I	54 Xe
6	55 Cs	56 Ba		72 Hf	73 Ta	74 W	75 Re	76 Os	77 Ir	78 Pt	79 Au	80 Hg	81 Tl	82 Pb	83 Bi	84 Po	85 At	86 Rn
7	87 Fr	88 Ra		104 Rf	105 Db	106 Sg	107 Bh	108 Hs	109 Mt	110 Ds	111 Rg	112 Cn	113 Uut	114 Fl	115 Uup	116 Lv	117 Uus	118 Uuo
Lanthanides				57 La	58 Ce	59 Pr	60 Nd	61 Pm	62 Sm	63 Eu	64 Gd	65 Tb	66 Dy	67 Ho	68 Er	69 Tm	70 Yb	71 Lu
Actinides				89 Ac	90 Th	91 Pa	92 U	93 Np	94 Pu	95 Am	96 Cm	97 Bk	98 Cf	99 Es	100 Fm	101 Md	102 No	103 Lr

Figure 4.10. The periodic table. Lanthanides have atomic numbers from 57 to 71

The strongest interaction between electrons within 4f orbital is of repulsion character due to Coulombic interaction. It determines the mutual positions of terms of the ion which are separated on energy scale in the order of 10^4cm^{-1}. Since lanthanide ions possess heavy nuclei, the spin-orbit coupling plays an important role in splitting the terms into J-levels with separation of the order of 10^3cm^{-1}. The terms created in this way are described by symbol $^{2S+1}L_J$, where 2S+1 represents the total spin multiplicity, L specifies the total orbital angular momentum and J - the total angular momentum of the f electrons.

Terms described till now correspond to free ion levels. In the case of an ion placed in a coordination environment, like a crystal or an organic ligand, further splitting of J-levels is observed due to electric field of the matrix. These splittings are of the order of 10^2cm^{-1} and are usually referred to as crystal field splitting. The splitting pattern is determined by the symmetry of the coordination polyhedron around the lanthanide ion and by the crystal field strength. Because these levels have superfine structure their presence in the spectrum depends on resolution of the spectrometer.

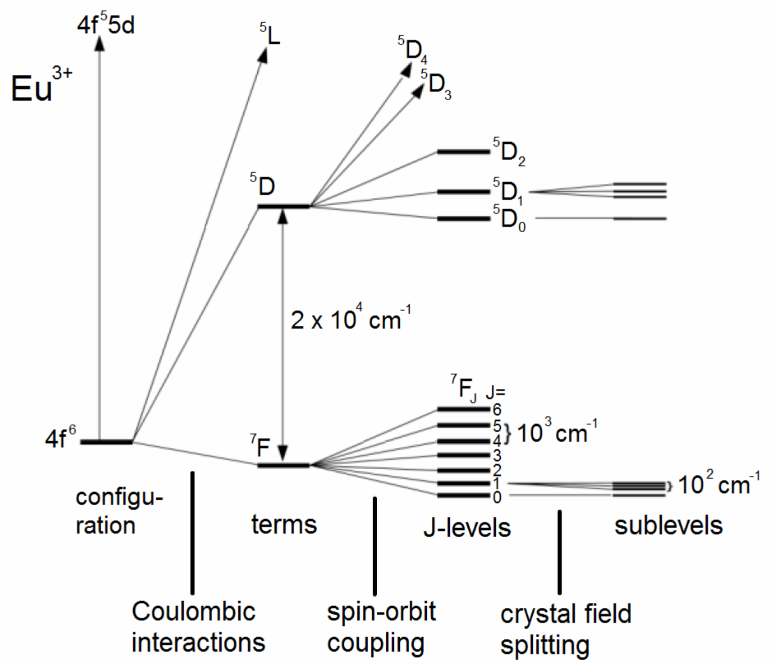

Figure 4.11. The interactions within Eu^{3+}, having configuration [Xe] $4f^6\,5d^0$, leading to the splitting of the electronic energy levels

Although luminescence of lanthanide ions is an efficient process they suffer from weak light absorption. Typical extinction coefficients are in the order of 1 M^{-1}cm^{-1} with bandwidths of less than 0.2 nm. In order to apply lanthanide ions as light-emitting species it was necessary to find a way of their efficient excitation. In 1942 Weissman discovered that intense metal-centred luminescence can be observed for lanthanide complexes with organic ligands, when they are excited in the absorption band of a ligand [34]. Since organic ligands possess broad intense absorption bands, they are able to work as an antenna that harvests excitation energy and subsequently transfers it to the ion of the complex. The scheme of such a process is shown in figure 4.12.

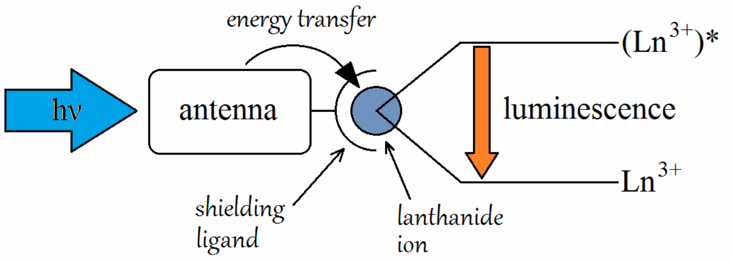

Figure 4.12. The scheme of emission mechanism in organic complexes of lanthanides

Upon UV light irradiation of a complex the electronic transition occurs at the ligand from the ground state to the vibrational level of the first singlet excited state. After VR the ligand is in the lowest vibrational level of the first singlet excited state. Due to the influence of a heavy ion the inter-system crossing takes place from the singlet state S_1 to the triplet state T_1 of the ligand and, subsequently, energy is transferred to an energy level of the ion. It is important to notice that the triplet level of a ligand should be higher on the energy scale than the resonance level (emitting level) of an ion, otherwise the transfer is not possible (or will not cause luminescence of the ion). If the ligands triplet level is equal to the lanthanide resonant one, back transfer may occur from the ion to the ligand. In this case phosphorescence of the ligand often may be observed.

The second important role of a ligand in lanthanide complexes is to shield an ion from the environmental surroundings and prevent it in this way from a radiationless deactivation. The most important reason for a lanthanide ion radiationless decay is vibrational coupling with a ligand or solvent molecules.

In the face of the above discussion the tetrakis β-diketonate complexes are a promising alternative for the lanthanide tris coordination compounds, exhibiting higher luminescence quantum yields due to better shielding of a lanthanide ion, larger cross-sections for photon absorption and charge carrier trapping.

As already mentioned, emission of lanthanide complexes is similar to those of an ion and exhibits sharp-line spectra corresponding to the transitions between the ion energy levels. The energy levels of trivalent ions of terbium and europium as well as an example of PL spectra of their complexes are presented in figure 4.13.

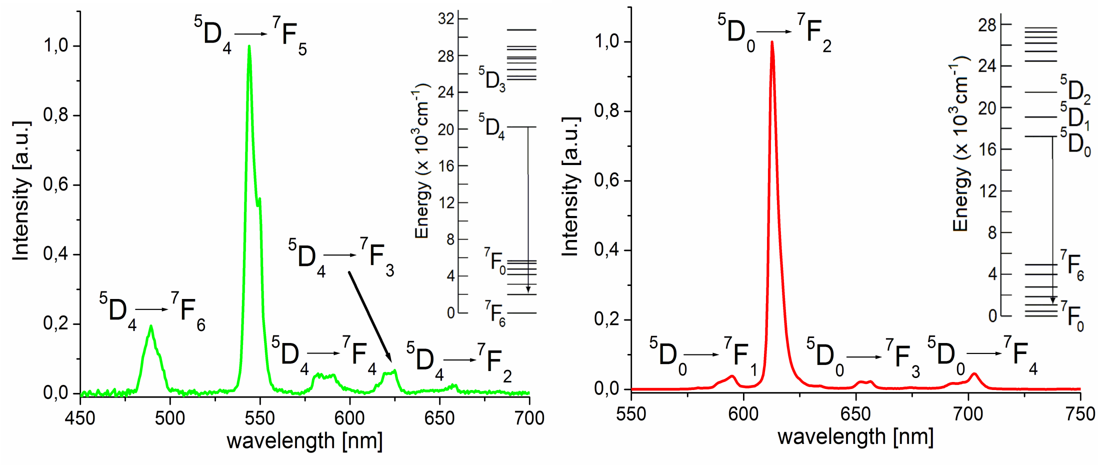

Figure 4.13. Emission spectra of Tb^{3+} (left) and Eu^{3+} (right) in Tb(hfa)$_4$P(Ph)$_4$ and Eu(tta)$_4$P(Ph)$_4$ complexes, respectively. In the insets energy levels of Tb^{3+} and Eu^{3+} ions and the most intense transitions between the proper energy levels are denoted. For molecular structures of the complexes see section 7.1.2

4.12. Ionic states in organic solid

Till now we have discussed excited states in organic systems considering only isolated molecules. However, when molecules are closely packed, as in a solid, interaction between them modifies the positions of their energy levels, as shown in figure 4.14.

In the figure singlet and triplet energy levels of a molecule are denoted as S and T, respectively, and ionization energy as I_G and electron affinity as A_G. Due to electrostatic interaction between dipole moments of the molecules in the solid state the relevant energy levels of excited states decrease in comparison to an isolated molecule. Additionally,

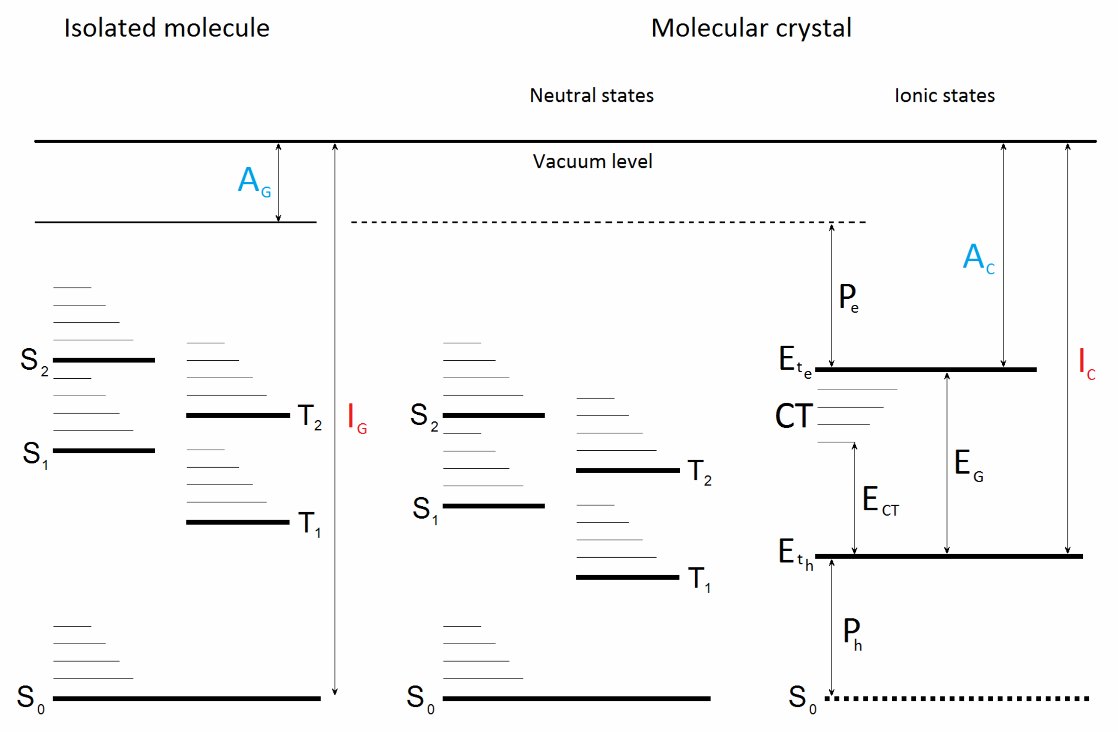

Figure 4.14. The positions of energy levels for an isolated molecule and a molecular crystal. For the meaning of each symbol see the text

interaction between molecules in crystals creates energy bands being responsible for charge transport. Interaction between molecules is also the cause that ionization energy of a crystal (I_C) diminishes with respect to I_G of an isolated molecule by a factor P_h referred to as the hole polarization energy. Similarly, electron affinity in a crystal (A_C) is deeper than in an isolated molecule (A_G) and the difference P_e is called the electron polarization energy. The energy level denoted as E_{te} corresponds here to the narrow (due to weak intermolecular interactions) band responsible for transport of excessive electron within an organic crystal while the energy level E_{th} to the relevant band transporting excessive hole. These levels are separated by the energy gap E_G which must be surpassed in order to create a pair of charge carriers. Levels E_{th} and E_{te} are often referred to as the HOMO and LUMO ones, respectively, though the two latter terms are associated essentially with isolated molecules.

Below E_{te} level the charge-transfer states are localized, separated from E_{th} with the energy gap E_{CT} which is smaller than E_G.

4.13. Onsager model of charge pair dissociation

Figure 4.15 shows possible processes in an organic material involving generation of bound charge pairs (e-h). In the scheme, the (e-h) pair creation under optical as well as electrical excitation are presented in order to maintain generality of the discussion.

Absorbing a photon a molecule becomes excited from the ground state E_0 to a "hot" excitonic state E*. This state can either relax vibrationally to the first excited state E_1 with probability $1-\eta_0$ and subsequently deactivate radiatively or nonradiatively to the ground state, or with probability of η_0 become a bound geminate charge pair (e-h). This entity is referred to as geminate (e-h) pair or charge-transfer (CT) state and was described earlier in more detail. A geminate pair (e-h) can recombine to state E_1 with probability *R* (geminate recombination) or dissociate to free charge carriers with probability Ω.

In the case of an electrical excitation, charge carriers injected from proper electrodes meet together in a bulk of an organic material and form an intermediate (e-h) pair state. This pair can create emissive state E_1 or dissociate. The last process is highly sensitive to the external electric field, with Ω probability increasing with the field strength. Therefore, the external quantum efficiency of an OLED may depend on electric field applied to the device.

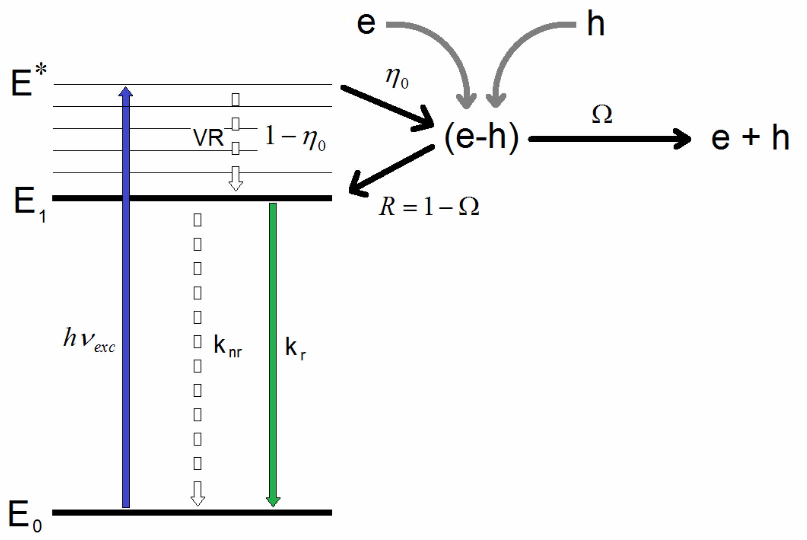

Figure 4.15. Processes leading to creation of a bound charge pair (e-h) in an organic material

The formula, derived by Onsager [35], describing the dissociation probability Ω of a charge pair in the presence of external electric field *F* has the form

$$\Omega(E)=1-\frac{r_c}{2Er_0}\sum_{j=0}^{\infty}W_j\left(\frac{r_c}{r_0}\right)W_j\left(\frac{2Er_0}{r_c}\right). \tag{4.29}$$

The symbol *E* is here a dimensionless quantity describing the electric field

$$E=\frac{eFr_c}{2kT},\quad F=\frac{U}{d}, \tag{4.30}$$

r_c is the so-called Onsager radius, *i.e.* the distance at which coulombic interaction between charges forming an (e-h) pair is equal to the thermal energy *kT* (see formula 4.13) and r_0 is the initial distance between charges at a pair creation moment. The functions $W_j(x)$ of order *j* are here determined by the following recurrence

$$W_0(x) = 1 - \exp(-x),\; W_{j+1}(x) = W_j(x) - \frac{x^j \exp(-x)}{j!}. \tag{4.31}$$

4.14. Triplet-triplet annihilation

The triplet-triplet annihilation (TTA) is usually the main reason for the efficiency roll-off in OLEDs employing phosphorescent emitters. It is so due to two factors: i) triplet lifetimes are in the range of microseconds while lifetimes of singlet excitons are in the nanosecond range, ii) during electrical excitation the probability of triplet exciton creation is of 75% whereas there is only the 25% chance of creation of an exciton with singlet multiplicity. These two facts imply that the concentration of triplets in OLEDs is usually much higher than that of singlets and, hence, the interaction between triplets will be dominant.

When two triplet states with random orientation of spins encounter, there exist three possible ways the spins can combine without breaking the spin conservation rules, as shown in table 4.1 [36].

Table 4.1 Spin statistics for the interaction of two triplets

	T_n	T_n	Total Spin $S = T_n + T_n$	Arrow Notation	Multiplicity = (2S + 1)	Final State, Symbol
Case 1	T_+ (↑↑)	T_- (↓↓)	0	↑↓↑↓	1	Singlet, S
Case 2	T_+ (↑↑)	T_0 (↓↑)	+1	↑↑↓↑	3	Triplet, T
Case 3	T_+ (↑↑)	T_+ (↑↑)	+2	↑↑↑↑	5	Quintet, Q

According to the table, the first combination produces a singlet state, the second creates a triplet state and the third one produces a quintet. However, quintet excitons do not contribute to the luminescence of organic materials. This is because in order to create an excited quintet state in TTA process the energy sum of two participating triplets must be at least equal to the energy of the quintet. This situation is rare in organic electroluminescent materials [37]. Additionally, even if the encounter complex acquires a quintet multiplicity, the separation is more probable than the annihilation, or it returns to be excited triplet [38, 39]. Therefore, the two most typical mechanisms of TTA in a diode are as presented in a scheme below.

$$T_1 + T_1 \leftrightarrow {}^{1,3,5}(T_1 - T_1) \xrightarrow{k_{TTA}} \begin{cases} \xrightarrow{25\%} S_n + S_0 \to S_1 + S_0 \left(\xrightarrow{k_{isc}} T_1 + S_0 \right) \\ \xrightarrow{75\%} T_n + S_0 \to T_1 + S_0 \end{cases}$$

In the annihilation process of two triplet states (T_1) an intermediate state (T_1 - T_1) is created which subsequently can be transformed either into a hot singlet state (S_n) (with probability 25%), or into a hot triplet state (T_n) (with probability 75%), and the ground state singlet (S_0). Then, the hot excited state relaxes to the first excited state (S_1 or T_1). If we deal with a phosphorescent emitter the S_1 state changes the multiplicity to T_1 due to intersystem crossing (k_{isc}) (bracket in the upper row in the scheme). As a result, from two triplet excitons existing before the annihilation one triplet or one singlet exciton remains after TTA process. The above scheme shows that while for phosphorescent emitters the TTA is an undesired phenomenon that leads to the decrease of internal quantum efficiency of OLEDs, in the case of a diode with fluorescent emitter it may improve performance of the device.

4.15. Triplet-polaron annihilation

Another possible annihilation process is that due to interaction between triplet excitons and charge carriers, as shown in the scheme below. Typically, the number of trapped charges greatly surpasses the amount of free ones, therefore we can write [40]

$$T_1 + e_t^- \xrightarrow{k_{Te}} S_0 + e^- ,$$

$$T_1 + h_t^+ \xrightarrow{k_{Th}} S_0 + h^+ ,$$

where the subscript t denotes a trapped charge. As a result of the annihilation of triplet T_1 with a trapped electron e_t^- or a trapped hole h_t^+, a singlet ground state S_0 and a hot electron e^- or a hot hole h^+ can be created. Considering multiplicity of the participants of this triplet-polaron (Tq) annihilation we obtain a scheme presented below.

$$T_1 + D \leftrightarrow {}^{2,4}(T_1 - D) \xrightarrow{k_{Te}, k_{Th}} S_0 + D*$$

During Tq annihilation process a complex of a triplet exciton and a doublet (charge carrier) is created. This complex may possess either the doublet or quartet multiplicity, available from the total six possible spin mixtures. Since in Tq annihilation a charge takes energy from a triplet the latter will be converted into the singlet ground state. The charge carrier after the annihilation process receives the excess of energy and can either relax in its trap or becomes a free charge carrier.

5. ORGANIC LIGHT-EMITTING DIODES (OLEDs)

In this chapter the basic architectures used in organic electroluminescent diodes are presented from the simplest to the most sophisticated one. In the first section the stress is put on explaining the function of each layer of a device while in the second one different strategies to obtain white emission are shown. The reader searching for more information and examples of white light-emitting diodes can refer to S. Reineke, M. Thomshke, B. Lüssem, K. Leo, Rev. Mod. Phys. 85 (2013) 1245

5.1. Basic types of OLEDs

All organic light-emitting diodes consist of organic layer(s) sandwiched between electrodes with at least one of them being semitransparent, as shown in figure 5.1. By applying a bias voltage to the electrodes injection of electrons from a cathode and holes from an anode is initiated. The carriers meet together in the organic material of semiconductor properties and create excitons which subsequently recombine radiatively emitting light.

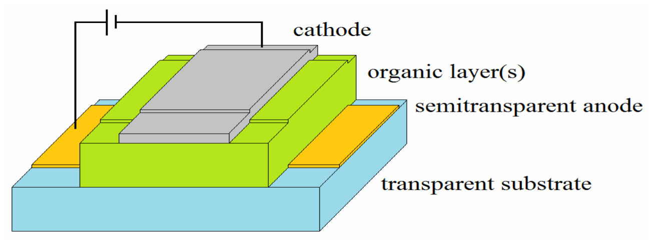

Figure 5.1. A general structure of an organic light-emitting diode

5.1.1. Single layer devices

The simplest organic light-emitting diode consists of a single organic layer sandwiched between electrodes, a scheme of the device is presented in figure 5.2. In this type of diode an organic material simultaneously serves as transporter of both types of charge carriers and as emitter of light. By improving the charge transport properties of applied compound, the exciton radiative recombination probability decreases because [41]

$$P_{rec} = \frac{\tau_t}{\tau_t + \tau_{rec}}, \tag{5.1}$$

where τ_t and τ_{rec} are the transit and recombination time of the carriers, respectively. On the other hand, a charge trapping on the emission centres increases the recombination chance, but decreases the transport abilities as a charge carrier must be released from a trap in order to continue its travel within a layer. This may disturb injection from electrodes into organic material because the charge trapped close to the electrodes creates a barrier for the carriers entering a device. Thus, both transport and trapping are crucial in such a simple system and good balance of these properties is important to achieve an efficient diode.

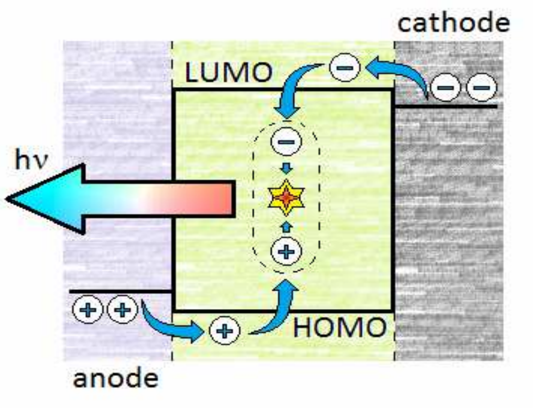

Figure 5.2. A scheme of a device with single organic layer

Considering electrodes, usually their energy levels should match well those of the applied organic material, that is the highest occupied molecular orbital (HOMO) in the case of an anode and the lowest unoccupied molecular orbital (LUMO) in the case of a cathode. As for the ideal carrier injection, the Ohmic contact should be created, *i.e.* without energy barrier for charge carriers between the electrode and the organic layer. However, as mobilities of holes and electrons are typically different for a given material it may be desired to have an energy barrier at one of the electrodes to balance carrier injections.

Three different injection mechanisms may be involved in OLED operation. The first one is a charge carrier injection above an energy barrier created between the electrode and organic material. Such a situation is created typically when a cathode is build of a low-work-function metal, *e.g.* calcium or barium. The second injection mechanism involves the tunneling through an energy barrier. Materials used for this type of contacts are insulators and their layer must be sufficiently thin to allow the process to be effective. An example of the material applied in this type of electrode is LiF with the layer thickness of 0.5 - 1.5 nm. The third possibility is the Ohmic contact, mentioned already above. To obtain such a contact it is not necessarily difficult, for example for the red emitter possessing a small energy gap.

Though single layer devices have drawbacks mentioned at the beginning, they are easy to build, also using wet techniques like spin-coating. This makes them a cheap solution for large area diodes.

5.1.2. Single layer devices with a guest

The development of the idea from the previous section is a single layer device with a dopant as an emitter of light. Introduction of a guest has important implications for OLED operation. First of all, the carrier transport and recombination processes are separated and occur in two specialized in their purposes materials. After charge injection into a host, the carriers may be transported efficiently through the device. Typically, the emitting dopant concentration does not surpass 10% of a layer composition (w/w) and charge trapping in vicinity of the electrode is limited which establishes good injection conditions. On the other hand, if an electron or a hole are trapped in a potential well of the dopant emitting centre (see figure 5.3),

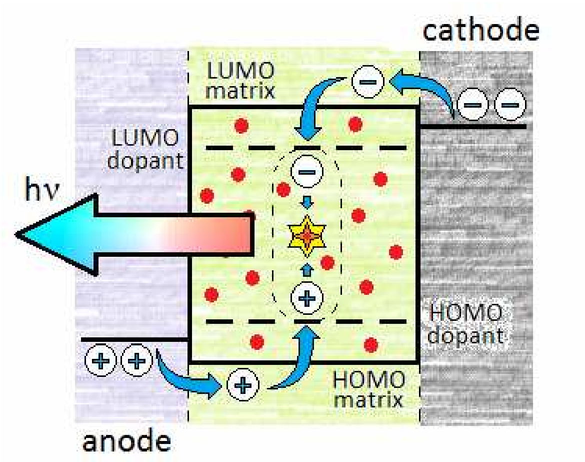

Figure 5.3. A scheme of a single layer device with a dopant (red dots)

they can stay there for a time long enough to increase the effectiveness of opposite sign carrier capture, an exciton creation and, subsequently, radiative recombination. In the case that the recombination occurs on the host it is highly probable that energy transfer to the guest will take place. This is because the energy gap of the matrix material is larger than that of the dopant material and, consequently, the host emits at higher energy than the guest. Distribution of a guest in a matrix also prevents from concentration quenching of emission.

5.1.3. Devices with transporting layers

Organic materials typically have different electron and hole mobilities. As a result, the recombination zone in a single layer device shifts towards a certain side of the diode, which may reduce the performance of OLEDs by the interfacial exciton quenching due to energy transfer to the high-density electrode states or generation of plasmons in an electrode. A solution of this problem is application of charge transporting layers, as shown in figure 5.4.

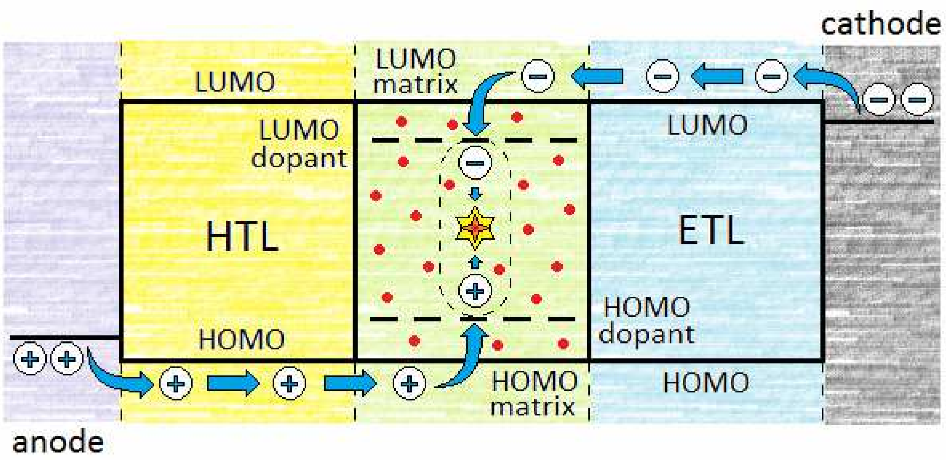

Figure 5.4. A scheme of a device with a hole transporting layer (HTL), doped emitting layer and electron transporting layer (ETL)

In this type of device transport of electrons and holes is separated and assigned to the materials specialized in their tasks. As a result, charge is injected and conveyed to the recombination zone very efficiently, but when it arrives there the charge carriers are trapped on dopant emitting centres. In this way the transit time through the emitting layer (τ_t) is longer, increasing the recombination probability (P_{rec}). Another advantage is the position of recombination zone in the central part of a device, far from the electrodes, which diminishes excitation of plasmons.

An important step towards efficient charge injection and transport was done by doping transporting layers with *p* and *n* type species [42, 43]. In this way a device constructor has a greater freedom of choice of electrodes materials because one does not have to match the work function of the electrode to the energy levels of transporting materials. As a result, the best devices are able to approach the thermodynamic limit [44] when the voltage necessary to turn on a device corresponds to the emitted photon energy divided by the elementary charge. However, the creation of organic molecules with *p* (or *n*) doping capabilities requires that their HOMO and LUMO levels must be positioned much deeper (shallower) than in the case of typical organic semiconductors, therefore, a special effort is necessary to design such molecules. Additionally, the stability of *n* type doping materials is diminished due to shallower HOMO levels which makes reduction by oxygen of these compounds much easier.

5.1.4. Devices with blocking layers

In the operating electroluminescent device a charge carrier in principle is able to pass through the whole diode without recombination with the counter charge. Such a situation, termed as the leakage current, is detrimental to the diode and it is a parasitic effect. In order to prevent from this effect, blocking layers are incorporated at both interfaces of the transporting layers and emitting layer, as shown in figure 5.5.

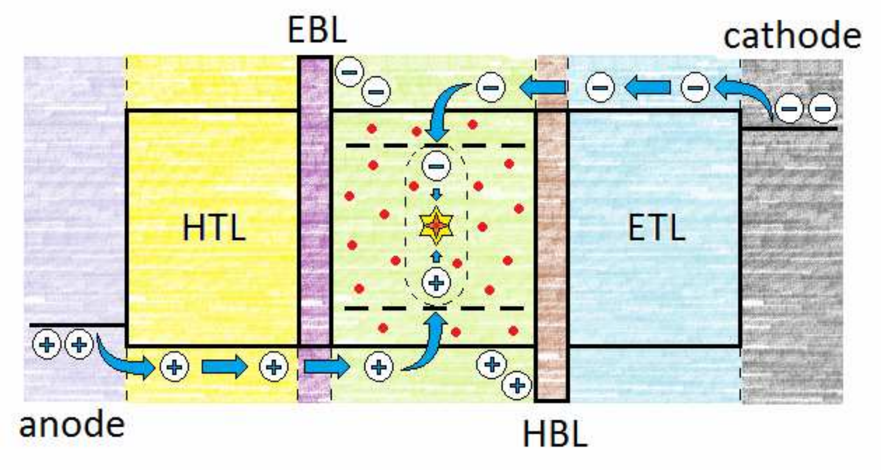

Figure 5.5. A scheme of a device with a hole transporting layer (HTL), electron blocking layer (EBL), doped emitting layer, hole blocking layer (HBL) and electron transporting layer (ETL)

Compounds used as blocking layers must have properly localized energy levels with respect to transporting and matrix materials. In the case of electron blocking layer (EBL), the HOMO should have similar energy as the HOMO of the HTL and the matrix, while the LUMO must be higher than its neighbour layers. In this way electrons that arrive to the edge of the emitting layer are blocked there and cannot reach the HTL. Similarly, a hole blocking layer (HBL) must have the LUMO at the energy level of the matrix and the ETL, but the HOMO below their HOMO levels. Blocking layers should be thin, around 10 nm, just to stop charge within the emitting zone, but without having significant influence on device thickness.

5.2. White organic light-emitting diodes (WOLEDs)

We start to describe WOLEDs from a brief review of architectures used in these devices. In figure 5.6 the most common approaches are shown: a) doping single colour lumiphores into a single emitting layer, b) building a stack of layers emitting in different spectral regions, c) applying monochrome devices with semitransparent electrodes as a stack, d) using adjacent monochrome subpixels, e) converting blue light partially by phosphors placed on a surface of a blue OLED.

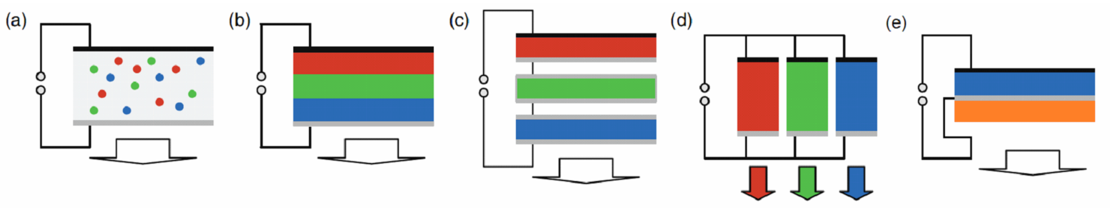

Figure 5.6. Different approaches used in OLEDs to generate white light. Semitransparent electrodes are grey, reflective electrodes are shown black

The most straightforward way to generate white light in a WOLED is to blend different colour luminophores in the emitting layer. The first WOLED having reasonable efficiency was built by Kido and co-workers in 1994 using this method (Fig. 5.7) [12].

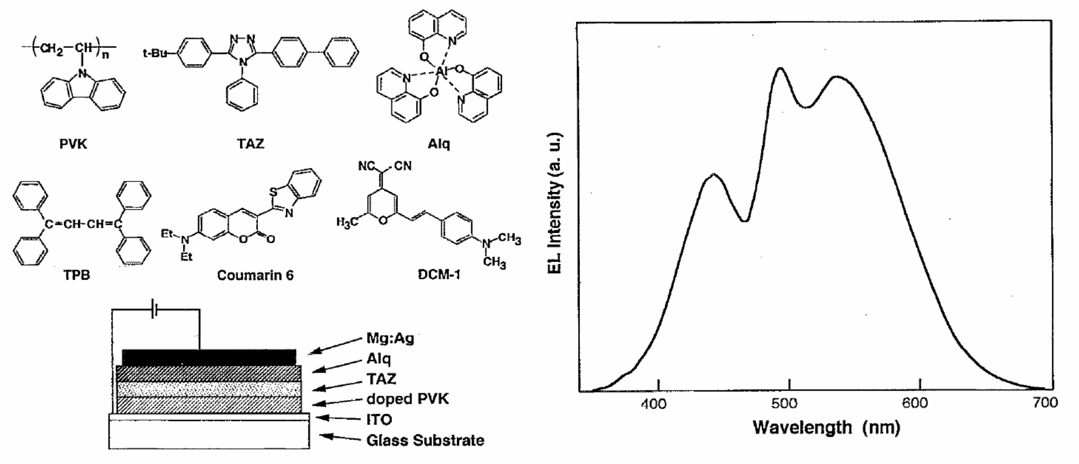

Figure 5.7. Device architecture, structures of molecules and EL spectrum of the WOLED built by Kido and co-workers [12]

The drawback of such a simple device architecture is possible phase separation of the components with the passage of time which will result in film nonhomogeneity, local changes in current density and spectral shift of emitted light. The requirements for materials applied in this concept may be also contradictory like balanced transport of electrons and holes through a matrix.

The second approach in building WOLEDs is construction of a multilayer device, where each layer emits different colour. The first diode of this type was presented by Kido *et al*. in 1995 [45]. This strategy requires application of vacuum evaporation optionally with spin-coating used to prepare some layers. The big challenge in multilayer WOLEDs is to maintain the balance of all colours at different brightness levels. The colour variation is caused by excitation complexity of emitting species involving direct electron-hole recombination on dopants, energy transfer processes and shift of the recombination zone with increase of applied voltage.

The next architecture used in WOLEDs is a stack of OLEDs. This approach has some advantages as compared to the previous concept. They are less susceptible to colour change at different biases because the current density in each subdevice is the same. The stack architecture allows for current reduction due to the presence of charge generating zones placed between organic layers [46-48]. After external bias application a charge is injected from the external electrodes and also generated directly inside of a device. Since the operational lifetime of OLEDs depends on current density in a superlinear manner, reduction of current density is able to increase the device lifetime significantly.

A variation of the stack concept is a device in which subdevices can be addressed separately. In this way colour balance of the components can be controlled independently via brightness change. Additionally, degradation of emitters due to aging can be actively compensated.

The advantage of direct addressing of each colour is also present in adjacent subpixel architecture. Such an arrangement requires, however, closely spaced stripes to give an impression of white colour, which creates some difficulty in processing. Typically, production involves vacuum evaporation through shadow masks, though wet technique is also applicable [49].

The last way to obtain white OLEDs we describe is borrowed from inorganic white LEDs. It involves a blue emitting OLED and an orange phosphor placed on it. When the diode is emitting, some of light is absorbed and reemitted by the phosphor giving overall white emission. Such a concept is not very frequently applied in WOLEDs because it requires an efficient and long living blue OLED which is one of the real problems of organic emitters.

Now we review very briefly the strategies for generating white electroluminescence from the employed materials point of view. The most obvious way of white light creation seems to be doping a conductive host with guests emitting primary or complementary colours. In the first method red, green and blue emitters are applied and their simultaneous emission creates white light. The complementary colours approach is based on Grassmann's law, which states that chromatic sensation can be described in terms of an effective stimulus consisting of linear combinations of different light colours [50]. In this method only blue and orange emitters are used, together creating white light. Such an approach simplifies the device design and building process, but the typical disadvantage is lower CRI[1] compared to WOLEDs containing three emitters.

In the doping approach small molecules as well as polymers can be applied in a single and multilayer configuration. In the first case co-evaporation of a dopant with host molecules is used to create emitting layer(s). An example of such a device together with structures of employed molecules is displayed in figure 5.8.

Considering application of polymers, the easiest method is to add emitting dopant species into polymeric matrix. However, much more interesting solution is to synthesize a single compound emitting white electroluminescence. For this purpose, the block copolymers or polymers with pedant emitting groups as well as single molecules can be employed [52-58], examples are presented in figure 5.9. The existence of such materials paves the way to large-area light sources produced by cheap spin-coating or roll to roll methods.

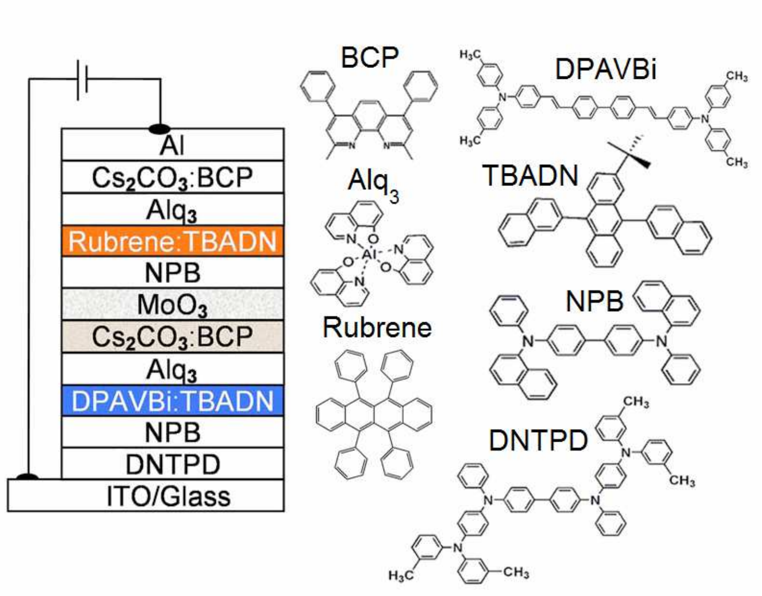

Figure 5.8. Design of a WOLED applying the complementary colours strategy and structures of molecules used [51]

Another way of white light formation is the application of compounds having simultaneous monomer and excimer or electromer emission [59, 60]. The EL spectrum of this system does not change with device aging because only one species is responsible for the emission. Moreover, the excimer/electromer spectrum forms typically a broad structureless band which is desired for white light generation purpose. Disadvantages of this approach are typically low efficiencies of excimer or electromer emission and difficulty in controlling the EL bands associated with these states.

---

[1] Colour Rendering Index (CRI) is the parameter describing how well a light source reproduces true colours of the object. See chapter 6 for more details.

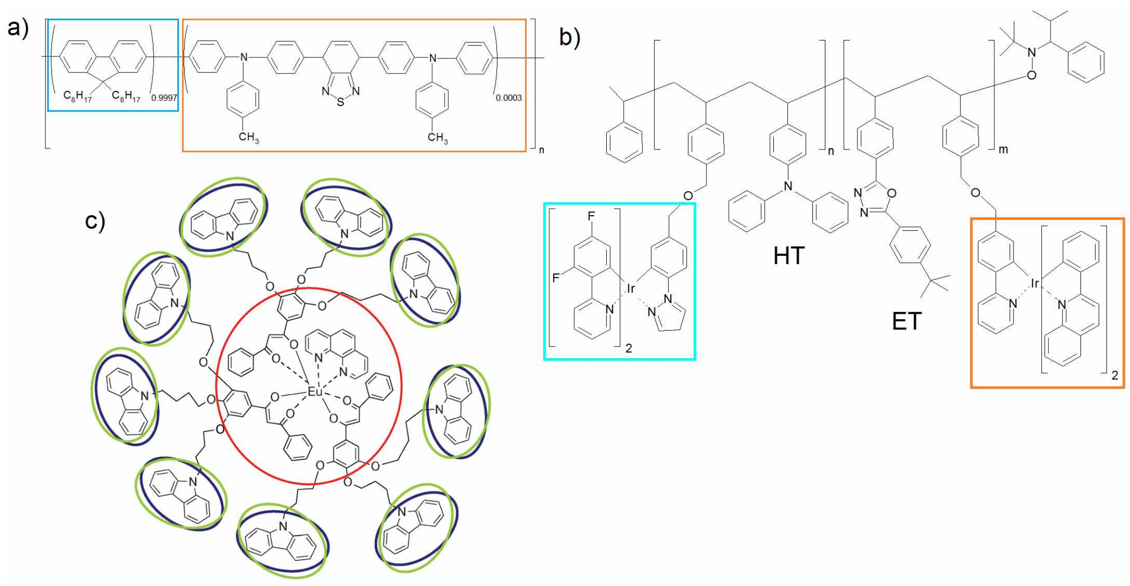

Figure 5.9. Examples of compounds emitting white light. (a) Block copolymer [57]. (b) Polymer with pendant groups, HT and ET denote hole transporting and electron transporting groups, respectively [58]. (c) White light emitting molecule [54]. In all cases colours show the emission spectral range of the proper part of the compound

6. PARAMETERS DESCRIBING LIGHT-EMITTING DIODES

In order to be able to compare different light sources without an ambiguity a set of parameters describing their properties is necessary. We can divide them roughly into four groups: i) characterizing colour perception of emitted light by the human eye; ii) describing electrical performance of a diode; iii) combination of the first two; iv) remaining parameters describing a diode. Into the first group we include the Comission International d'Eclairage (CIE) chromaticity coordinates, the colour temperature (CT) or correlated colour temperature (CCT), the colour rendering index (CRI) and luminance. The second group consists of turn-on voltage, internal and external quantum efficiency. Parameters from the third group are luminous efficacy and luminous power efficacy. The last group consists of spatial distribution of emitted radiation and stability of a device. Below each term is described shortly and at the end of this chapter the definition of white light is given.

6.1. The CIE chromaticity coordinates

All colours visible by the human eye in photopic vision[*] mode can be expressed by a set of numbers *x* and *y*, known as the *CIE* chromaticity coordinates. The coordinates determine the position of a colour in the *CIE* 1931 chromaticity diagram, shown in figure 6.1. The arc within the centre of the diagram is known as the Planckian locus and shows the coordinates of black body radiation at different temperatures. At coordinates (0.33, 0.33) the equal energy white is placed, which converges to the coordinates of the black body at temperature 5780K corresponding well with the photosphere of the Sun temperature [61].

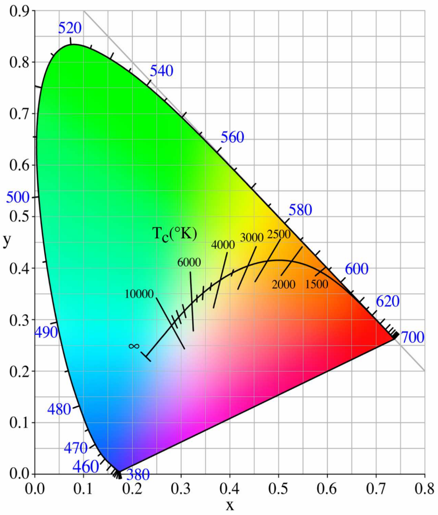

Figure 6.1. The *CIE* 1931 (*x*, *y*) chromaticity diagram. The Planckian locus, isotherms and wavelengths in nanometres (blue numbers) are indicated. Colours in the diagram are approximation only

---

[*] Photopic vision is a way of perception of an eye in high brightness conditions, in opposite to scotopic vision, which is operational at low light levels.

Now we describe how to calculate the *CIE* coordinates. In figure 6.2 the colour matching functions $\bar{x}(\lambda)$, $\bar{y}(\lambda)$ and $\bar{z}(\lambda)$ are depicted. They were derived experimentally on a sample of many people and can be considered as a chromatic response of the standard observer.

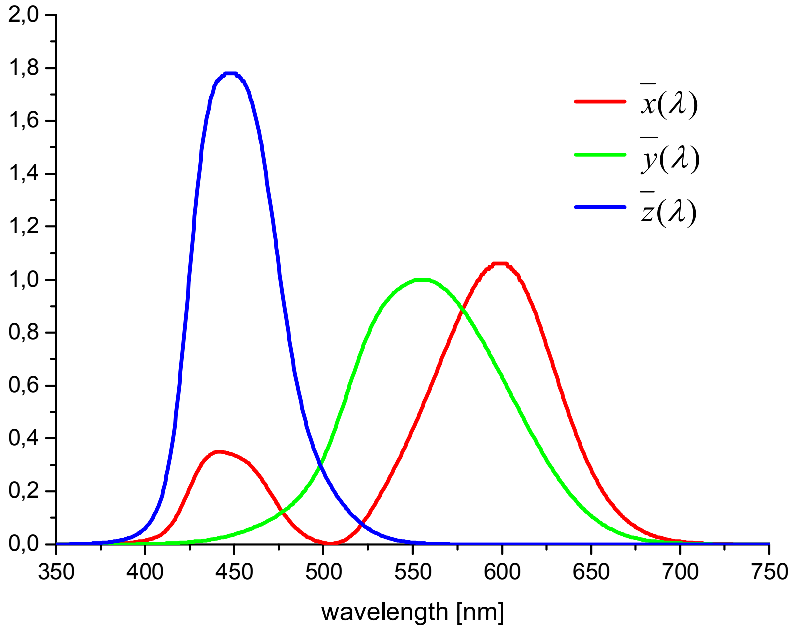

Figure 6.2. The colour matching functions of the *CIE* standard observer

In order to find the *CIE* coordinates of a light source having spectrum $I(\lambda)$ we integrate the product of the spectrum with each matching function. Obtained three numbers X, Y, Z are known as the tristimulus values:

$$X = \int_0^\infty I(\lambda)\bar{x}(\lambda)d\lambda\,, \qquad Y = \int_0^\infty I(\lambda)\bar{y}(\lambda)d\lambda\,, \qquad Z = \int_0^\infty I(\lambda)\bar{z}(\lambda)d\lambda\,. \tag{6.1}$$

The chromaticity coordinates are defined as

$$x = \frac{X}{X+Y+Z}\,,\; y = \frac{Y}{X+Y+Z}\,,\; z = \frac{Z}{X+Y+Z}\,. \tag{6.2}$$

It is easy to notice that $z = 1 - x - y$ and it is enough to know two coordinates (*x*, *y*) to determine the chromaticity of a given colour.

6.2. Colour temperature (CT) and correlated colour temperature (CCT)

It is common to describe a colour of light sources in terms of temperature expressed in kelvins. If a given light source had a spectrum of the black body radiator, its *CIE* coordinates lie exactly on the Planckian locus. For such light sources the colour temperature (*CT*) name is assigned and *CT* is equal to the temperature of the black body at the chromaticity coordinates of a given source. The best example of such a light source is an incandescent bulb. In the case that a spectrum has not a form of the black body radiation, but the *CIE* coordinates are still close to the Planckian locus (the term "close" is explained below), the name correlated colour temperature (*CCT*) is used. Following the official definition [62]: “The correlated colour temperature is the temperature of the Planckian radiator whose perceived colour most closely resembles that of a given stimulus at the same brightness and under specified viewing conditions”.

The temperature of colours was defined not in the *CIE* 1931 colour space but in the *CIE* 1960 Uniform Chromaticity Space (*CIE* 1960 UCS) [63], which chromaticity diagram is shown in figure 6.3. The reader should notice that in the *CIE* 1960 UCS the lines denoting an equal temperature – isotherms are perpendicular to the Planckian locus arc while in the *CIE* 1931 they are not (fig. 6.1). In both spaces, however, the isotherms are straight lines. From both diagrams it is clear that there are many colours having the same temperature because there are many points with different coordinates which lie on the same isotherm.

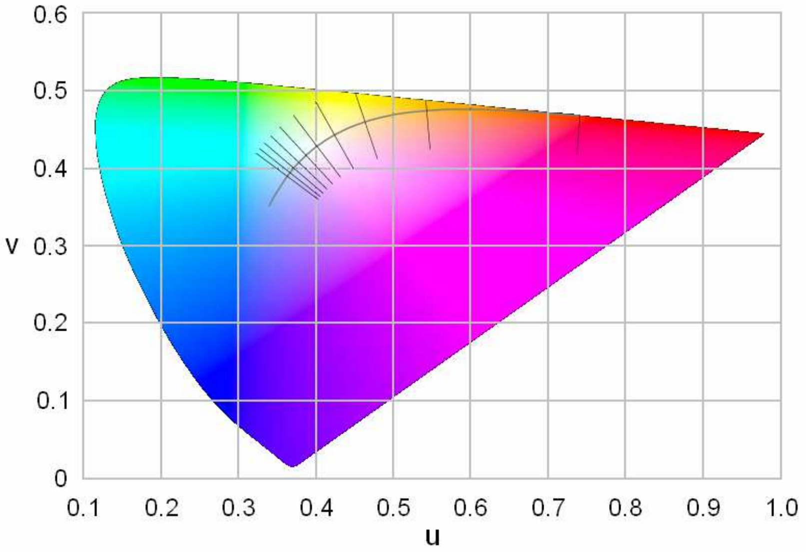

Figure 6.3. The *CIE* 1960 UCS (*u, v*) chromaticity diagram. The Planckian locus and isotherms from 1,000K to 10,000K are indicated

After simplification of the chromaticity diagram of *CIE* 1960 UCS by MacAdam [64], to calculate the (*u*, *v*) chromaticity coordinates in the *CIE* 1960 colour space, formulas presented below are used

$$u = \frac{4x}{-2x+12y+3}, \quad v = \frac{6y}{-2x+12y+3}, \tag{6.3}$$

where *x* and *y* are the chromaticity coordinates from the *CIE* 1931 diagram. Following the definition, to determine *CCT* of a source having chromaticity coordinates (u_s, v_s) we must find the minimal distance to the point on the Planckian locus, the coordinates of which we denote as (u_P, v_P). Using geometrical properties of the *CIE* 1960 space, the chromaticity distance *DC* is defined as

$$DC = \sqrt{(u_s - u_P)^2 + (v_s - v_P)^2}\ . \tag{6.4}$$

Having determined the chromaticity coordinates of the Planckian radiator the closest to our source we ascribe the *CCT* to the temperature of the black body at the coordinates (u_P, v_P).

It is set that to maintain a meaningful result the *DC* difference between the coordinates should be less than 0.0054. It allows to avoid an ambiguity when the chromaticity coordinates of a source are equidistant to two points on the locus. In order to distinguish whether a source coordinates are above or below the locus, the *DC* is positive for the first and negative for the latter case. The *CCT* can be calculated numerically but in this work we used two approximations from references [65] and [66].

6.3. Colour rendering index (CRI)

The colour rendering index (*CRI*) is the parameter describing how well a light source reproduces colours of illuminated objects with respect to the reference light source, both having the same *CT* or *CCT*. It has a value from 0 to 100 and the latter one means an excellent similarity. The *CRI* evaluation is based on the comparison of colour appearance of the eight test samples illuminated by the tested and the reference light sources. A determination of *CRI* does not require performing an experiment as the reflectance spectra of the test samples are known [67] and reference source spectra can be generated numerically. A detailed calculation of *CRI*, based on references [68-70], is presented in Appendix A, here we discuss certain restrictions imposed on the *CRI*.

A high *CRI* value should not be automatically assigned to a good quality of light, *i.e.* its natural reproduction of colours. That is because a reference source itself may not render colours perfectly. Again the best example is an incandescent bulb, having the *CRI* equal to 100. However, objects illuminated by this light source are not rendered naturally. Especially in the blue spectral region, where this kind of source has small intensity, the reproduction of colour is rather poor.

Due to the discontinuity of reference source determination at 5000K, two very close light sources (one with *CCT*=4999K and the other with *CCT*=5001K) may give an overestimated difference of their *CRI*s.

The CRI as well as CCT cannot be evaluated for sources emitting non-white light.

6.4. Luminance

The luminance of a source is the quotient of the luminous intensity of light emitted within the given solid angle per unit area of the source. The unit for luminance is candela per square meter (cd/m^2). It is defined by formula

$$L = \frac{d^2\Phi_v}{dSd\Omega\cos\theta}\,, \tag{6.5}$$

where Φ_v is the luminous flux (lm), S is the area of a source (m^2), Ω is the solid angle (sr) and θ is the angle between the surface normal and the specified direction.

A derivation of the formula determining luminance of a device and also the formulae of other quantities describing performance of an electroluminescent diode can be found in Appendix B.

Luminance should not be confused with term brightness since the latter depends on the state of the eye, *e.g.* a source will seem brighter in a dark room than in a daylight, even if its luminance is the same.

6.5. Turn-on voltage

The turn-on voltage (V_{on}) is defined typically as the voltage at which a device starts to emit light (reaches 0.1 cd/m^2). It depends on the heights of energy barriers between the energy levels of organic materials and electrodes, the thickness of an OLED and the transporting properties of employed materials. Generally, the lower the value the better and today the best devices approach or even surpass [71] their thermodynamic limit.

6.6. Internal quantum efficiency

The internal quantum efficiency (η_{int}) is the ratio of photons generated inside a device to the number of charge carriers injected into the diode. It can be expressed also as

$$\eta_{\text{int}} = \eta_{PL} P_{ss} P_{rec}, \qquad (6.6)$$

where η_{PL} is the quantum yield of an emitter, defined as the ratio of the radiative to the total decay rate constants, P_{ss} denotes the probability, based on the spin statistics, that in an electron-hole recombination event the emissive state with proper multiplicity will be created, and P_{rec} is the (e-h) recombination probability. According to the spin statistics, $\frac{1}{4}$ of excitons created in EL are singlets and $\frac{3}{4}$ are triplets. Thus, for fluorescent emitters the maximal η_{int} is equal to 25%, assuming $\eta_{PL} = 1$, $P_{rec} = 1$ and no interaction between excitons (we neglect *e.g.* triplet-triplet annihilation process from which excited singlet state may be created). The above theoretical calculations were confirmed experimentally by Baldo and co-workers [72, 73].

In the case of phosphors, due to strong spin-orbit coupling, the multiplicity of excited states is not well defined, which makes forbidden transitions partially allowed. Since typically the first excited triplet state has lower energy than corresponding the first excited singlet state, EL from the first one is observed. The OLEDs with employed phosphorescent emitters are able to achieve $\eta_{\text{int}} \approx 100\%$ $\eta_{PL} \approx 100\%$, which was presented by Adachi and co-workers [74, 75].

Interestingly, conjugated polymers and oligomers seem to not obey the above spin statistics rule. As they are fluorescent materials, the devices containing them should not surpass 25% of the internal quantum efficiency under electrical excitation. However, it was proved that in these compounds the singlet states are created easier than triplets [76-79], which may increase η_{int} of OLEDs comprising this type of materials [80, 81]. On the other hand, there are examples of small molecule fluorescent emitters that also surpassed the theoretical limit for singlet exciton creation [82], therefore the issue remains still unclear.

6.7. External quantum efficiency

The internal quantum efficiency is important in determination of physical properties of materials employed in a device. However, considering application of OLEDs, more useful is the external quantum efficiency (η_{ext}), which is defined as the number of photons emitted from a device per amount of charge carriers injected into the device. It can be also expressed as

$$\eta_{ext} = R_{out}\eta_{\text{int}}, \tag{6.7}$$

where R_{out} is the outcoupling factor, describing extraction of photons generated inside the device from the diode.

It is well known that majority of generated light never leaves an OLED due to intrinsic losses, generation of plasmons in electrodes, total internal reflection and waveguiding, and self-absorption [83].

To solve the trapped light problem many solutions have been proposed, like Bragg mirrors [84], low refractive index grids [85], photonic crystals [86], antireflection coatings [87], patterned substrates [88] and microlenses [89, 90], to name but a few examples.

6.8. Luminous efficacy

The luminous efficacy (η_l) is defined as the ratio of the device luminance *L* multiplied by its active area *S* to the intensity of current *I* flowing through the OLED

$$\eta_l = \frac{LS}{I} \tag{6.8}$$

and is expressed in cd/A. The η_l can be considered as η_{ext} with included photopic eye sensitivity. The reader should be aware that in the literature various alternative names are used for luminous efficacy and also for luminous power efficacy described below.

6.9. Luminous power efficacy

The luminous power efficacy (η_p) of a light source is expressed by

$$\eta_p = \frac{\Phi_v}{IU}, \tag{6.9}$$

where Φ_v is the luminous flux, I is the current intensity and U is the voltage. The unit of luminous power efficacy is lm/W.

Luminous power efficacy of a source should not be confused with luminous efficacy of radiation, also having the lm/W unit. The latter expresses the ratio of the luminous flux to the radiant flux of a source and describes how much of the produced radiation is useful for the human eye.

6.10. Spatial distribution of emission

For a standard OLED it is common to assume that a spatial distribution of emission follows the Lambert law [91] which means that the emission intensity depends on the cosine of the angle between the normal perpendicular to the device surface and the observation direction. In figure 6.4 the normalized integrated intensity of OLED emission is shown as a function of the observation angle, together with theoretically calculated the lambertian emission pattern. The agreement is good enough and in this work we always based on the lambertian distribution assumption.

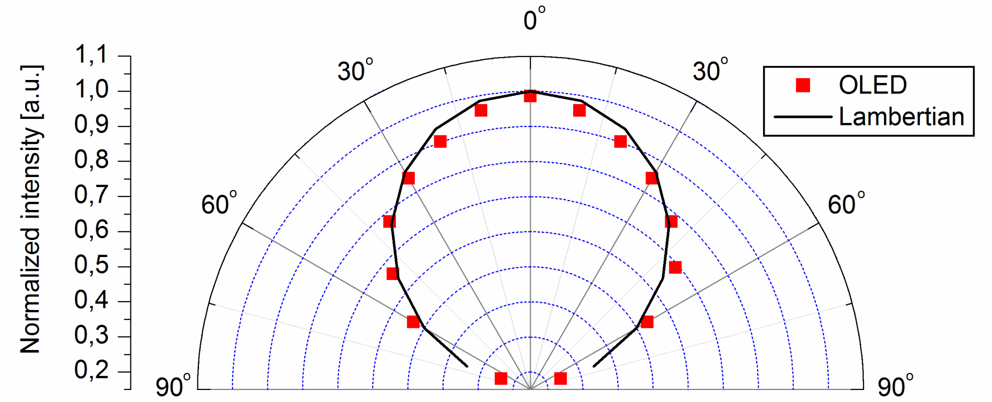

Figure 6.4. Normalized spatial emission distribution of a single layer F8BT OLED (points) and lambertian distribution (line)

By modifications introduced into a device it is possible to change a spatial distribution of emission. Application of a microcavity arrangement allowed to achieve sharply directed emission [92]. On the other hand, a patterned substrate enhances and broadens outcoupled light flux [89, 90].

6.11. Stability

The stability of a WOLED can be understood in two ways. The first one considers a change of the EL spectrum during increase of the voltage applied to the device. The most typical example is a dominant red emission at low luminance level and then a gradual growth of the green and blue components. This change in the spectrum can be caused by a direct charge trapping and subsequent recombination at the red emitting centres at low brightness levels. Red emitters possess smaller band gaps than the other employed emitting and transporting materials which facilitates charge trapping. Another possibility is energy transfer from the blue and green emitting materials to the red emitter. In both cases at some point the red emission is saturated and the higher energy emission emerges. In multilayer devices another option is a shift of recombination zone with increase of applied voltage. Due to the change of transport conditions in a diode, the recombination zone may move within organic layer stack from the layer emitting one colour to the layer emitting another one, thus influencing the balance of light components creating the white light.

Today the commercially available WOLEDs change their CIE coordinates at different luminance levels within the margin $x < 0.01$, $y < 0.01$, which makes the above problem negligible.

The second parameter describing the stability of a WOLED is its operational lifetime, *i.e.* how long a diode preserves the performance properties above a chosen level. The most commonly standard used here is LT70, which is defined as the time required to decrease the luminance to 70% of the initial value. Since lifetimes of present devices are in the range of tens of thousands of hours, to determine them some extrapolations were required. A decrease in luminance with time can be described by the stretched exponential decay [93]

$$L = L_0 \exp\left[-\left(\frac{t}{\tau}\right)^{\beta}\right], \tag{6.10}$$

where L_0 is the initial luminance and τ and β are the fitting parameters dependent on the used materials and device architecture.

There may be many origins of luminance decrease during organic diode operation, like exposure to water and oxygen due to poor encapsulation, crystallization, morphological changes at the different materials interfaces and chemical reactions, all together changing injection, transport and recombination properties of a WOLED. Degradation is a complex problem and despite many years of study there is still much work to fully understand processes responsible for luminance decrease [94].

The lifetime of an OLED, t, decreases in proportion to the current density, j, according to relation

$$t \propto j^{-n}, \tag{6.11}$$

where n (=1.2-1.9) is the acceleration factor [95]. From the above formula it is clear that in order to increase a lifetime we must apply more efficient emitters in a device, which would decrease the current density necessary to obtain the required luminance level. Another possibility is to employ a larger electrode area which decreases the current density and this way the luminance, but the amount of produced light remains the same due to a larger emissive surface.

6.12. White light definition

White is the colour the human eye sees when it senses light which contains all the wavelengths of the visible spectrum. As was mentioned at the beginning of this chapter, the equal energy white has chromaticity coordinates (0.33,0.33). In this chromatic point all the three basic colours have equal contribution to the human eye perception, giving as a result white light. In practice, as the white light sources are considered not only emitters the emission spectra of which have the (0.33, 0.33) coordinates, but all sources with coordinates close to the Planckian locus (the term "close" was defined in the section that describes *CCT*). From the applicative point of view not all white light sources are considered as suitable for the illumination purpose. Such emitters should fulfil CRI>80 condition and organic materials are here advantageous with their broad EL spectra.

In table 6.1 the chromaticity coordinates, colour temperatures, colour rendering indices and luminous power efficacies of common light sources are gathered.

Table 6.1. The *CIE* chromaticity coordinates (*x*, *y*), colour temperatures (*CT*) or correlated colour temperatures (*CCT*), colour rendering indices (*CRI*) and luminous power efficacies (η_p) of the light sources. Data from [96- 98]

Light source	*x*	*y*	*CT* or *CCT* [K]	*CRI*	η_p [lm/W]
High pressure sodium	0.519	0.417	2100	24	150
Incandescent bulb (100W)	0.448	0.408	2854	100	17
Tungsten halogen	0.448	0.407	2856	100	24
Fluorescent tube	0.375	0.367	4080	89	100
Xenon	0.324	0.324	5920	94	50
Daylight (Standard Illuminant D_{65})	0.313	0.329	6500	90	--

7. EXPERIMENTAL METHODS

In this chapter materials employed in devices and experimental methods used for their characterization are described.

7.1. Materials

7.1.1. Dendrons with pyrene antennae

A synthesis of the materials used in this investigation are described in ref. [99]. In our work the designation D is used for the energy donor molecules, A for the energy acceptor molecules and G for the dendrons. The subscript number (1,2,3) denotes the generation number of the donor or the dendron molecule. The donor molecules are built of pyrenes attached through alkyl chain and triazole ring to ester compound centre. Their structures are shown in figure 7.1.

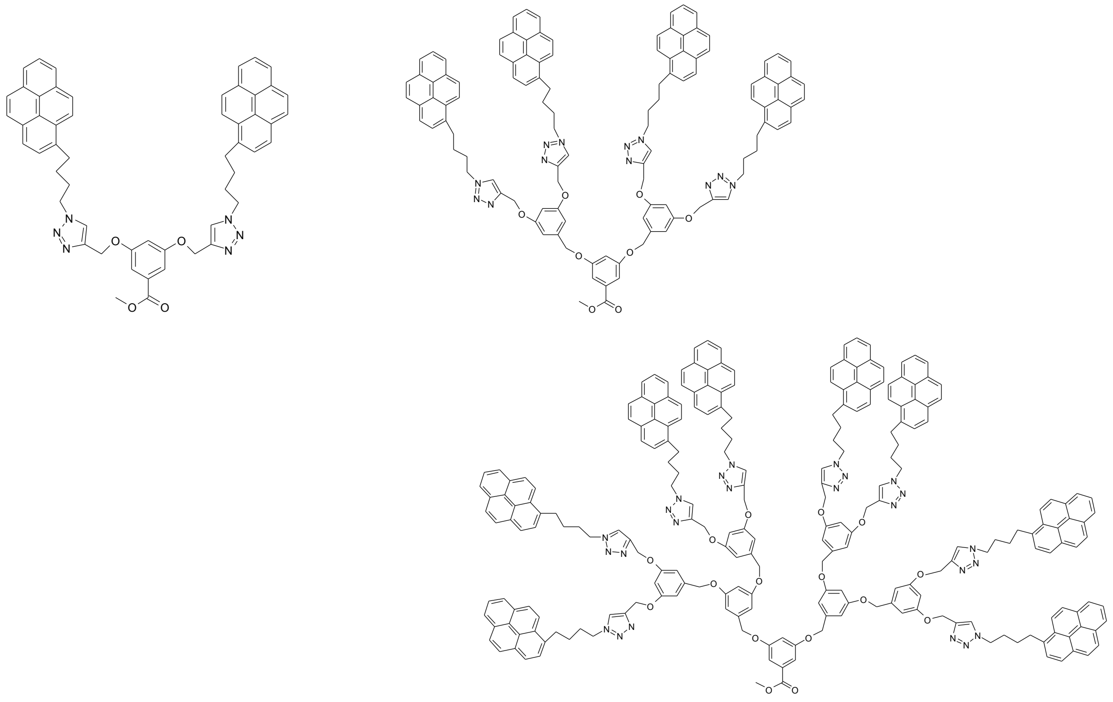

Figure 7.1. Chemical structures of the donor molecules D_1 (left), D_2 (centre) and D_3 (right)

A styrylpiridinium derivative molecule was used as the red emitting acceptor excited by energy transfer from pyrene antennae. Its structure is presented in figure 7.2.

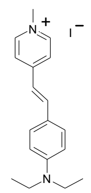

Figure 7.2. Chemical structure of the acceptor molecule A

The dendron molecules consist of the chemically bonded donor of proper generation, D_n, and the acceptor A, they are shown in figure 7.3.

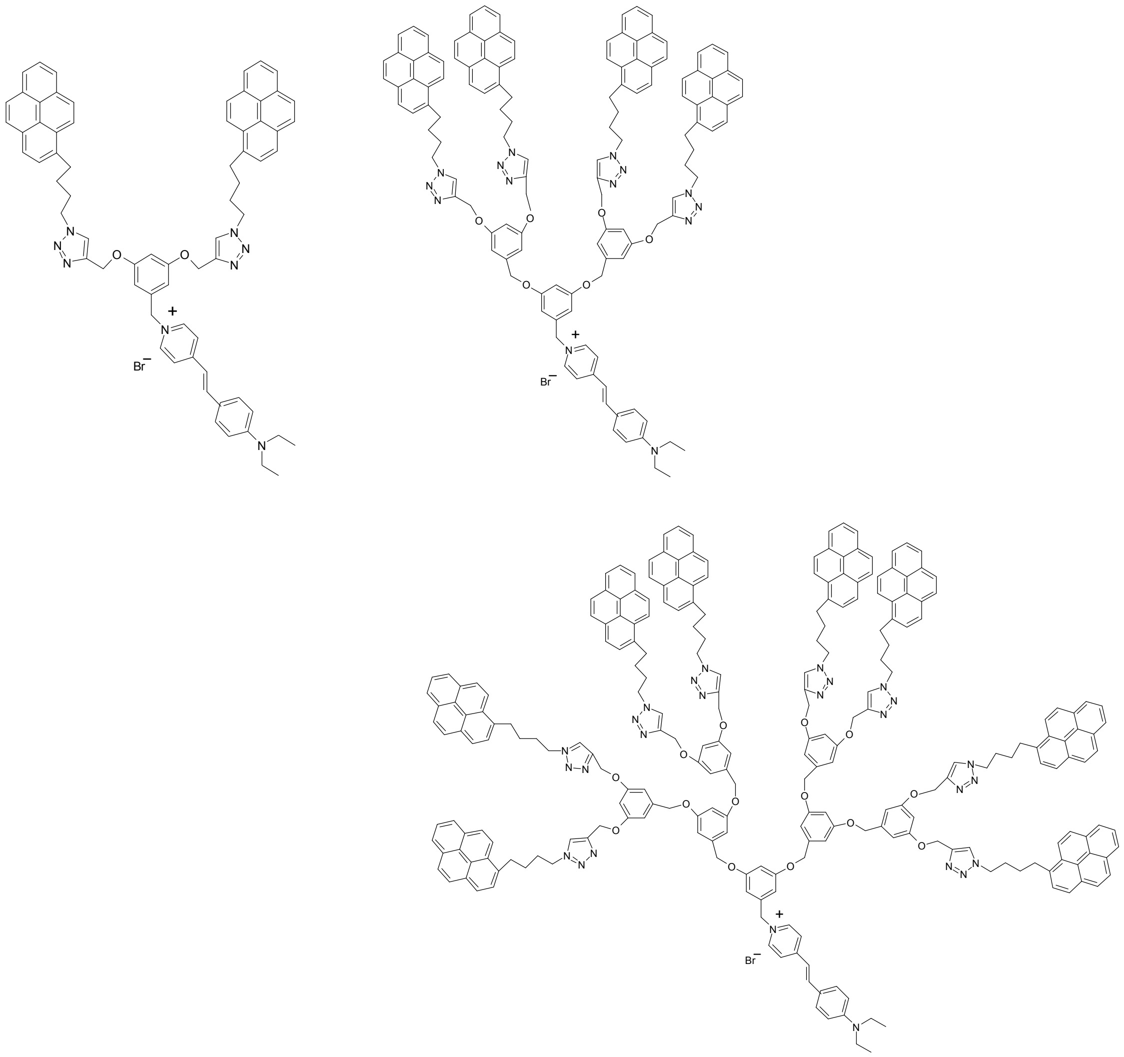

Figure 7.3. Chemical structures of the dendrons G_1 (left), G_2 (centre) and G_3 (right)

7.1.2. Tetrakis β-diketonate lanthanide complexes

As green and red emitters, tetraphenylphosphonium tetrakis-(1,1,1,5,5,5-hexafluoro-2,4-pentanediono)terbium(III) ($Tb(hfa)_4P(Ph)_4$) and tetraphenylphosphonium tatrakis(4,4,4,-trifluoro-1-(2-thienyl)-1,3-butadiono)-europium(III) ($Eu(tta)_4P(Ph)_4$) were used, respectively, in the WOLED based on tetrakis β-diketonate lanthanide complexes. Synthesis of the complexes used in this work are described in ref. [100]. Their chemical structures are presented in figure 7.4.

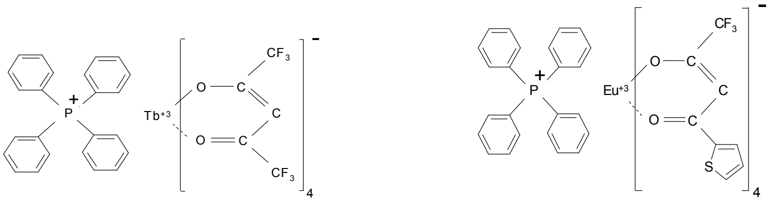

Figure 7.4. Chemical structures of green emitting $Tb(hfa)_4P(Ph)_4$ (left) and red emitting $Eu(tta)_4P(Ph)_4$ (right)

7.1.3. Organic platinum complexes

In the devices employing emission from the platinum complexes three types of complexes were used, their synthesis procedure can be found in ref. [60]. All the applied platinum complexes have similar base structure, the only difference is in the substituents at the two positions of the complexes. The structures of the complexes under investigation are presented in figure 7.5.

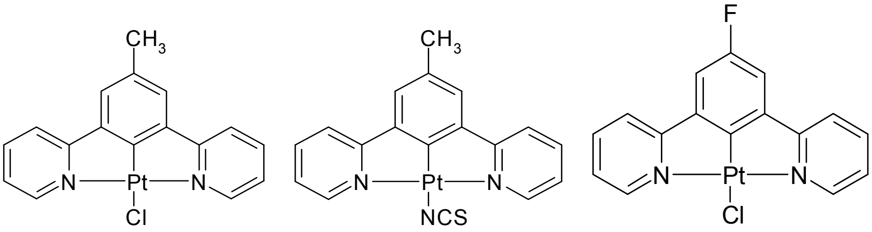

Figure 7.5. Chemical structures of MePtCl (left), MePtNCS (centre) and FPtCl (right)

7.1.4. Other materials

A typical matrix applied in an emissive layer in OLEDs from this work consisted of poly-N-vinylcarbazole (PVK) mixed with 2-(4-biphenylyl)-5-(4-tert-butylphenyl)-1,3,4-oxadiazole (PBD). The average molar weight of PVK employed in the matrices was 42.000 g/mol and both materials were purchased from Sigma-Aldrich and used as supplied. Their chemical structures are shown in figure 7.6.

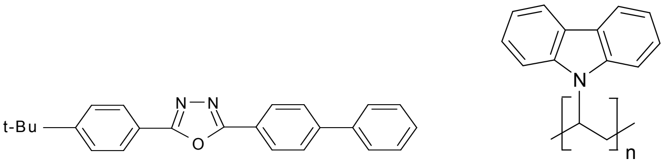

Figure 7.6. Chemical structures of PBD (left) and PVK (right)

In the improved OLEDs with the platinum complexes, PVK with a high molecular weight of 10^6 g/mol (PVK-h, Sigma-Aldrich) was used as a hole transporting layer.

In the double emissive layer WOLEDs with FPtCl, PVK-h was used in the blue emitting layer together with poly(9,9-dioctylfluorenyl-2,7-diyl) end-capped with N,N-bis(4-methylphenyl)-4-aniline (PFO, American Dye Source, M_w= 82.000 g/mol), applied as an emitter. The structure of PFO is shown in figure 7.7.

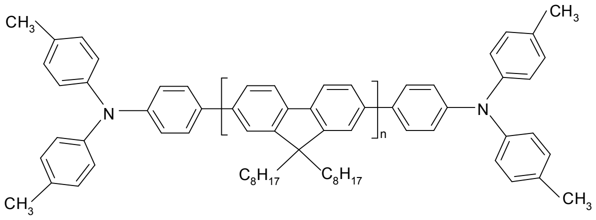

Figure 7.7. Chemical structure of PFO

Some samples used in energy transfer investigation between the matrix and the europium complex contained bisphenol-A-polycarbonate (PC) (Sigma-Aldrich, M_w= 45.000 g/mol) as a neutral binding polymer, its structure is depicted in figure 7.8.

In all OLEDs glass covered with indium tin oxide (ITO) was used as a substrate for devices. In all cases on glass / ITO substrates poly(3,4-ethylene-dioxythiophene)/poly(styrenesulfonate) (PEDOT:PSS) (H.C. Starck Clevios P VP.AI 4083) was spin-coated, creating a hole injecting layer. The structure of PEDOT:PSS is presented in figure 7.8.

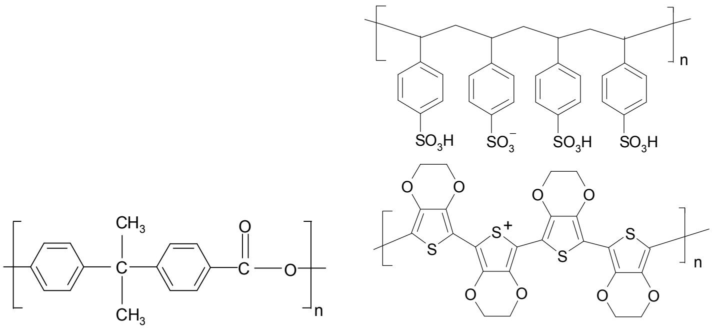

Figure 7.8. Chemical structure of PC (left) and PEDOT:PSS (right)

7.2. Samples preparation

7.2.1. Glass / ITO / PEDOT:PSS substrates for OLEDs

Glass substrates coated with indium tin oxide (ITO, with 20 ohms-per-square sheet) were cleaned ultrasonically in distilled water, acetone and 2-propanol. Afterwards, a 50 nm layer of PEDOT:PSS was spin-coated from a water solution filtered through nylon (pore size 0.45 μm), and annealed at 100°C for 10 minutes under a N_2 atmosphere. On such prepared substrates all types of OLEDs were built inside a nitrogen filled glovebox.

7.2.2. Samples based on the dendrons with pyrene antennae

Samples for photophysical characterization were prepared either in CH_2Cl_2 solutions, having concentration about 10^{-4} M, or by casting or spin-coating solutions on quartz substrates.

In the case of devices, the D_n and G_n molecules, PVK and PBD were dissolved in tetrachloroethane with the proper ratios at concentrations 15 mg/ml. Subsequently, a thin film creating emissive layer was spin-coated inside the nitrogen filled glovebox. The film thickness of the active layers was around 80-100 nm. Finally, 30 nm of calcium or 5 nm of barium and 100 nm of aluminium were thermally evaporated at 10^{-7} mbar.

7.2.3. Samples based on the tetrakis β-diketonate lanthanide complexes

All emissive layers of OLEDs were composed of PVK : PBD matrix and small amount of dopant(s). In the case of green emitting device the dopant was 4% (w/w) of $Tb(hfa)_4P(Ph)_4$ dispersed in 66% PVK : 30% PBD, while for the red emitting diode it was 4% of $Eu(tta)_4P(Ph)_4$

in the same matrix. In WOLEDs the ratio between the green and the red emitters was 4.5% : 0.5%, respectively, and the matrix consisted of 65% PVK : 30% PBD. The emitting layers were spin-coated from CH_2Cl_2 solutions, having the 7-10 mg/ml concentration, inside the nitrogen filled glovebox. Cathodes, consisting of 10 nm of calcium and 50 nm of aluminium, were deposited by thermal vacuum evaporation at 10^{-6} mbar.

Energy transfer was studied for 50 nm thick $Eu(tta)_4P(Ph)_4$: PVK blends and $Eu(tta)_4P(Ph)_4$: PBD : PC films, prepared in the same way as the emissive layers of the devices.

The PL quantum yields were measured in CH_2Cl_2 solutions or on samples prepared by casting or spin-coating solutions on quartz substrates.

7.2.4. Samples based on the organic platinum complexes

The emitting layers of simple green-emitting OLEDs (5% dopant), consisting of PVK, PBD and either FPtCl, MePtNCS or MePtCl, were spin-coated from a deaerated CH_2Cl_2 solution (8 mg/ml) comprised of 65% PVK : 30% PBD : 5% Pt complex by mass. As a cathode 10 nm thick layer of calcium and ca. 100 nm layer of aluminium were used.

In the case of improved green-emitting OLEDs, a film of PVK-h was spin-coated from CH_2Cl_2 solution (12 mg/ml) on substrates with PEDOT:PSS layers and subsequently the samples were annealed at 150°C for 30 min. Afterwards, on such prepared substrates emitting layers were spin-coated using the procedure as for the simple green-emitting OLEDs. The average total thickness of PVK-h and the emitting layer was equal to 165 nm for all three devices. Finally, a barium (5 nm layer) and aluminium (60 nm layer) were deposited by thermal vacuum evaporation at 10^{-6} mbar.

Devices containing high concentrations of FPtCl in the emitting layer were spin-coated from CH_2Cl_2 solutions, keeping more less the constant ratio between the materials creating matrices (2 PVK : 1 PBD).

In the WOLEDs, a film of PVK-h mixed with PFO with the ratio 52% PVK-h : 48% PFO by mass was spin-coated from toluene solution (15 mg/ml) onto the PEDOT:PSS-covered ITO substrates. The samples were successively annealed at 100°C for 30 minutes. Then the second layer, comprised of 40% PVK : 20% PBD : 40% FPtCl by mass, was spin-coated from CH_2Cl_2 solution (2 mg/ml). Finally, calcium (10 nm layer) and aluminium (60 nm) were deposited by thermal vacuum evaporation at 10^{-6} mbar.

7.3. Experimental setups

7.3.1. Photophysical measurements

The absorption spectra were measured either on Biotek Instruments XS or Perkin Elmer UV/VIS/NIR Lambda 900 spectrometer.

The luminescence spectra were recorded at room temperature by a liquid nitrogen cooled charge-coupled device (CCD, Spex) combined with a monochromator (Spex 270M). The steady state PL was excited by a monochromated xenon lamp, while EL was registered by applying constant bias to the devices. In the case of EL, the diodes were placed in nitrogen atmosphere. All the spectra were corrected for the instrument response.

Photophysical characterization of the platinum complexes was performed in degassed solvents, which was achieved *via* minimum three freeze-pump-thaw cycles whilst connected to the vacuum manifold. The final vapour pressure at 77K was $5\cdot10^{-2}$ mbar, as monitored using a Pirani gauge. Bimolecular rate constants for quenching by molecular oxygen, $k_Q^{O_2}$, were determined from the lifetimes in degassed and air-equilibrated solution, taking the concentration of oxygen in CH_2Cl_2 at 0.21 atm O_2 to be 2.2 mmol dm^{-3} [101].

7.3.2. Devices electrical characterization

The current–voltage (I–V) device characterization was performed with a Keithley 2602 source meter combined with a calibrated photodiode. The external quantum efficiency (η_{ext}) was calculated by measuring the light emitted in the forward direction and assuming the Lambertian emission intensity profile. All devices preparation and characterization was performed under a N_2 atmosphere inside a M-Braun glovebox system. The details of calculations of the parameters describing OLEDs can be found in appendixes A and B.

7.3.3. Thickness measurement

The thickness of the devices was measured with an AFM (NT-MDT NTEGRA) instrument in non-contact mode under ambient conditions after complete characterization of the diodes.

7.3.4. Photoluminescence lifetime measurements

In the case of samples with the lanthanide complexes the fluorescence lifetimes of PBD and PVK were measured with a streak camera (C5680, Hamamatsu), exciting the films by the third harmonic of a Ti:Sapphire laser (Mira 900, Coherent).

In the case of the platinum complexes the luminescence lifetimes of the complexes were measured by time-correlated single-photon counting, following excitation at 375 nm with an EPL-375 pulsed-diode laser. The emitted light was detected at 90^o using a Peltier-cooled R928 PMT after a passage through a monochromator. The estimated uncertainty in the quoted lifetimes is ±10% or better.

7.3.5. Quantum yield measurements

The quantum yields for the solutions were calculated according to formula [102]

$$\eta_{PL} = \eta_{PL}^{ref}\left(\frac{1-10^{-A_{ref}}}{1-10^{-A}}\right)\left(\frac{n^2}{n_{ref}^2}\right)\frac{AreaPL}{AreaPL_{ref}},$$

where η_{PL}^{ref} is the quantum yield of the reference emitter, *A* denotes the absorbance at the excitation wavelength, *n* stands for the refractive indices of solvents and *AreaPL* is the integrated PL spectrum divided before by photon energy. The formula requires that the excitation wavelength is the same for a reference and a sample, otherwise a correction for different intensities of excitation light is necessary. As the references quinine sulphate in 0.1M H_2SO_4 [103], rhodamine 6G in ethanol [104] or MePtCl [105] were used.

The quantum yields in solid state were measured in an integrating sphere using formula [106]

$$\eta_{PL} = \frac{P_c - (1-A)P_b}{AL_a}.$$

The subscript *c* denotes here the configuration where a sample inside the sphere is excited directly by an excitation light, the arrangement *b* corresponds to the sample excited by the excitation light scattered inside the sphere and subscript *a* describes the sphere without the sample. The *P* and *L* are the integrated emission spectra of the sample and the lamp, respectively, both divided by photon energy. Absorbance *A* is calculated from a formula

$$A = 1 - \frac{L_c}{L_b}.$$

In the case when the difference of emission intensities of a sample and a lamp was so big that during spectra acquisition the CCD was saturated, separate measurements were performed for the spectra *P* and *L* and, subsequently, they were normalized to the same acquisition time.

7.3.6. Electrochemical measurements of the lanthanide complexes

The cyclic voltammetry measurements of the complexes (*ca*. $1\cdot10^{-3}$ M in acetonitrile + 0.1 M Bu_4NClO_4) were performed at a platinum minidisc electrode (0.003 cm^2) and a scan rate of 0.1 V/s. The experiments were performed at 298 K under nitrogen in three electrode cells. The reference electrode was a silver/0.1 M silver perchlorate in acetonitrile (0.34 V *vs*. SCE). The voltammetric apparatus (AMEL, Italy) included a 551 potentiostat modulated by a 568 programmable function generator.

7.3.7. Electrochemical measurements of the platinum complexes

The cyclic voltammetry measurements were carried out using an Autolab PG-Stat 30 potentiostat with computer control and data storage *via* GPES Manager software. Solutions of concentration 1 mM in CH_2Cl_2 were used, containing $[Bu_4N][PF_6]$ 0.1 M as the supporting inert electrolyte. A three-electrode assembly was employed, consisting of a platinum wire working electrode (0.012 cm^2), a platinum wire counter electrode and a saturated calomel electrode (SCE) as the reference electrode. The polishing procedure for the working Pt electrode consisted of surface cleaning with diamond powder (Aldrich, diameter 1 µm) on a wet cloth (DP-Nap, Struers). The solutions were purged for 5 min with solvent-saturated N_2 gas with stirring, prior to measurements being taken without stirring. The ohmic drop (of 310 Ω) was compensated by the positive feedback technique. The voltammograms were referenced to a ferrocene–ferrocenium couple as the standard ($E^{1/2}$ = 0.42 V *vs*. SCE).

8. RESULTS AND DISCUSSIONS

In this chapter three ways of white light creation in OLEDs are presented with application of the materials described in chapter 7. Results from chapters 8.1, 8.2 and 8.3 were published in ChemPhysChem 11 (2010) 683, Phys. Chem. Chem. Phys. 11 (2009) 10152 and J. Mater. Chem. 21 (2011) 8653, respectively.

8.1. White electrofluorescent diodes based on the dendrons with pyrene antennae

The optical properties in solution and in solid state of D_2 dendron are presented in figure 8.1.1, though similar spectra were obtained for the first and the third generation molecules (D_1 and D_3, respectively). The absorption spectrum in dichloromethane reveals sharp peaks, corresponding to the $S_0 \rightarrow S_1$ and $S_0 \rightarrow S_2$ transitions of the pyrene unit, while in the solid state the spectrum broadens, but conserves all the spectral features. The registered slight red-shift (6 nm) of the absorption spectrum in the solid state, in comparison to the solution, indicates a presence of preassociated pyrene units in the ground state [107, 108]. The PL spectrum of D_2 donor in diluted solution (ca. 10^{-5} M) shows sharp peaks at 375 nm and 396 nm, corresponding to the $S_1 \rightarrow S_0$ transition of the monomer pyrene emission, and a broad intramolecular excimer emission centred at 488 nm [99]. In the solid state the monomer component of the PL spectrum disappears and only the green excimer emission is observed. Aggregation of the dendrons in the solid state causes pre-association of pyrene molecules that excludes emission from the monomers.

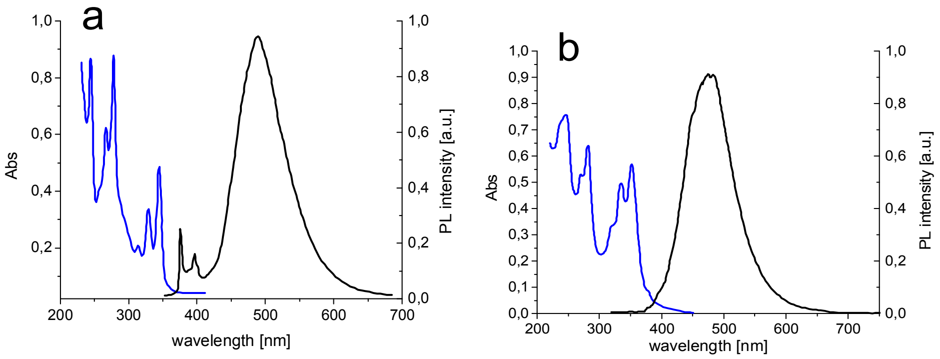

Figure 8.1.1. Absorption (blue) and PL (black) spectra of D_2 molecule in CH_2Cl_2 (a) and in the solid state (b)

The optical properties of the acceptor molecule A in solution and in solid state are gathered in figure 8.1.2. The molecule shows red emission centred at 620 nm in dichloromethane while in the solid state it is shifted to 660 nm and strongly quenched (see table 8.1.1) due to dependence on polarizability of the environment and intermolecular interactions [109 -111].

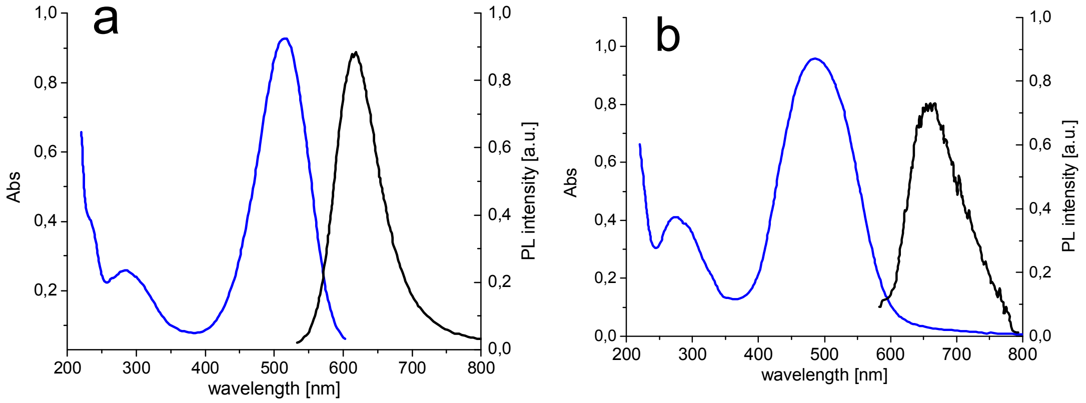

Figure 8.1.2. Absorption (blue) and PL (black) spectra of A molecule in CH_2Cl_2 (a) and in the solid state (b)

In figures 8.1.1 and 8.1.2 we notice that the absorption spectrum of the acceptor molecule overlaps very well with the excimer band emission of the donor molecule, both in solution and in solid state. Additionally, D_n molecules possess relatively high PL quantum yields (table 8.1.1) and A molecules - rather high extinction coefficient [112]. Therefore, efficient Förster type energy transfer is expected for the system containing the acceptor and donor molecules, in particular, dendrons G_n built from chemically bonded D_n and A moieties.

Absorption and PL spectra of the second generation dendron G_2 are presented in figure 8.1.3, but similar spectra were obtained also for the other dendron generations. The shape of PL spectra excited at 350 nm confirms the presence of energy transfer from the donor part of the dendron to the red emitting acceptor part. In solution (ca. 10^{-5} M) the most intense emission belongs to the acceptor A in the dendron, centred at 620 nm, but the pyrene monomer and excimer bands are still visible. Despite the above fact we can state that the dendrons show good light harvesting properties towards the red emitting acceptor. In the case of the solid state, energy transfer is even more efficient, since the pyrene emission disappeared and only the acceptor red light is detected. There are two reasons for more efficient energy transfer process in the solid state in comparison to the solution. The first one is the lack of monomeric pyrenes in the solid state which enhances the donor emission in the spectral region of better acceptor absorption. The second reason is an additional intermolecular energy transfer towards the red emitting dye in the case of solid state, which is not present in the solution.

A film of G_2 dendron reveals a bright red emission peaked at 635 nm despite a very weak emission of the neat acceptor molecules in the solid state. This feature can be ascribed to the screening effect of the pyrene units which reduces the quenching caused by intermolecular interaction between A molecules. As can be seen in table 8.1.1, the PL quantum yield of the molecules G_n in the solid state increases with the dendron generation, in agreement with the screening effect of the donor moieties. It is worth to note that the PL quantum yields of G_n films are the same for either direct acceptor excitation or donor excitation which reveals the conversion of excitation light to red light is performed efficiently by the dendrons in the solid state.

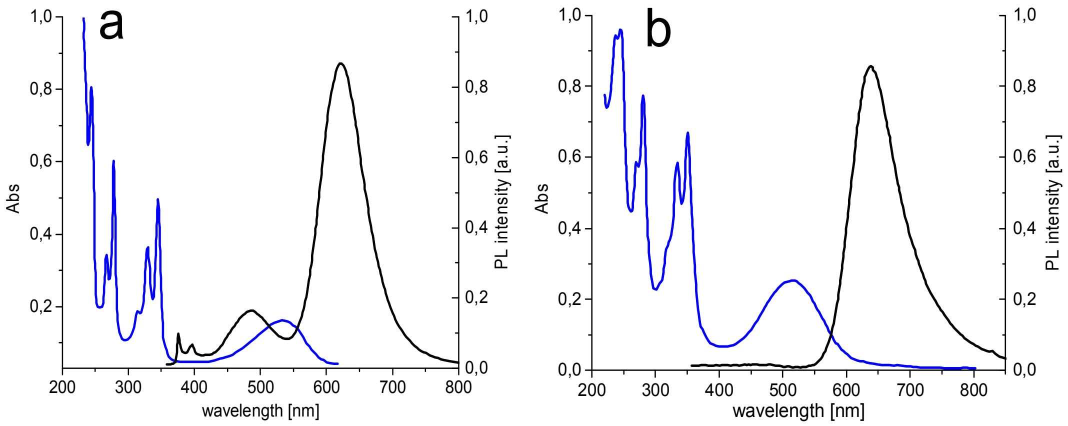

Figure 8.1.3. Absorption (blue) and PL (black) spectra of G_2 molecule in CH_2Cl_2 (a) and in the solid state (b)

To test the possibility of white light creation by our materials first we built devices containing a mixture of the D and G molecules. The EL spectra of devices consisting of solely D_2 molecule and 90 % D_2 : 10% G_3 mixture presented in figure 8.1.4 show a green emission at around 500 nm, typical of pyrene excimer [113], together with an additional component at 690 nm. The intensity of this red emission was dependent on the generation of D_n molecule, increasing with the generation (figure 8.1.4a inset) and also was growing with the operation time of the device with a D_2:G_3 blend (figure 8.1.4a bottom). A possible origin of the red emitting band may be triplet excimer of the pyrene units [114-116].

Table 8.1.1. PL quantum yields measured by exciting the pyrene donors at 350 nm or directly the acceptor molecule [a, b] for CH_2Cl_2 solutions and cast films

	A	D_1	G_1	D_2	G_2	D_3	G_3
solution	0.06 0.10[a]	0.24	0.14 0.22[a]	0.27	0.17 0.22[a]	0.32	0.28 0.29[a]
film	<0.01[a]	0.28	0.03 0.02[b]	0.22	0.07 0.07[b]	0.44	0.12 0.11[b]

[a] 488 nm, [b] 450 nm

In the case of PL spectra (figure 8.1.4b), measured on the devices with 90% D_2 : 10% G_3 blend, only the red emission from G_3 dendron was detected, in agreement with a complete energy transfer process from the D matrix to the acceptor of G molecule. Differently, in electroluminescence a weak red emission is superimposed on the dominating green D_2 emission and becomes quenched during device operation.

We note here that diodes built of solely G_3 dendron did not reveal any electroluminescence.

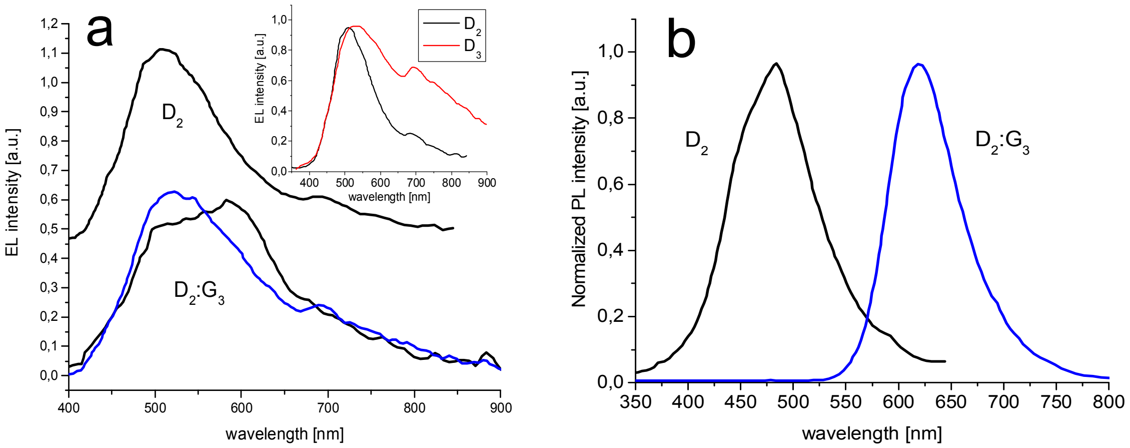

Figure 8.1.4. (a) EL spectra of D_2 film and D_2:G_3 blend at 10% G_3 concentration at the beginning of operation (black line) and after 2 minutes of operation (blue line) at 14V. In the inset EL spectra of D_2 and D_3 films; (b) PL spectra of D_2 film and D_2:G_3 blend

In order to improve stability of the red emission we decided to insert the molecules in a polyvinylcarbazole (PVK) matrix. PVK is a commercially available blue emitting and hole transporting polymer, widely used in OLEDs as a host. It possesses the LUMO and HOMO levels at 2.3 eV and 5.7 eV, respectively [100], providing a good fit with the energy levels of pyrene placed at 2.3 eV and 5.4 eV [113].

Absorption of PVK and PL spectra of PVK:G_3 blends for different dendron contents are presented in figure 8.1.5. The absorption spectrum of PVK resembles roughly that of pyrene, but is slightly shifted towards higher energy. Since the PL spectrum of the polymer is in the range 360-500 nm, it overlaps partially with both absorption spectra of pyrene and styrylpyridinium moieties of G_3. Consequently, PVK should be able to transfer energy to the dendron molecules. In the PL spectra of PVK:G_3 blends, the emission of the polymer and the dendron are present. The PVK component has a maximum at 413 nm while emission of G_3 molecules is manifested by the peak at 376 nm of the monomer pyrene and a broad band of the acceptor red emission. For all types of blends photoluminescence of pyrene excimers has not been observed.

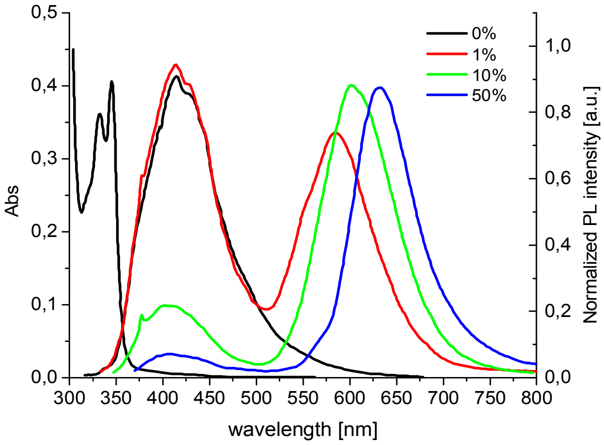

Figure 8.1.5. Absorption spectrum of a PVK neat film and PL spectra of PVK:G_3 films for different G_3 concentrations

A lack of the excimer band can be explained as follows. At low dendron concentrations in PVK, the pyrene units association is hindered due to a rigid polymer matrix surrounding G molecules. On the other hand, at high concentrations, when the pyrenes vicinity allows for the excimer formation, energy from the excimer is completely transferred to the acceptor moieties, as in the G_2 film (figure 8.1.3).

The emission intensity of the acceptor increases with respect to the PVK emission and the spectrum red-shifts with the increase of dendron concentration, reaching a maximum at 630 nm for the 50% concentration. This shift can be related to the dependence of the acceptor spectral properties on the polarizability of the environment [111]. The emission of PVK is still visible even at the 50% dendron concentration due to microaggregation of the dendron preventing from the efficient excitation energy reception from the polymer.

The EL spectra of PVK:G_3 blends presented in figure 8.1.6 do not show pyrene excimer emission. Similarly, like in the case of PL spectra, at low dendron concentration creation of the excimers is hindered, while at high concentration complete energy transfer to the acceptor occurs. The emission of PVK is characterized by a main band, centred at 440 nm, and a small low energy band at around 600 nm. The blue band of PVK, associated with singlet excimers, has been shown to possess spectral features dependent on the carbazole units conformation, while the low energy band was ascribed to triplet excimers of PVK [117, 118]. At low concentration of G_3 dendrimer the pyrene monomer peak and the acceptor emission band are superimposed on the EL spectrum of PVK. At higher concentrations the main emission originates from the acceptor and it shifts from 610 nm for the 10% concentration of G_3 to 630 nm for the concentration equal to 50%.

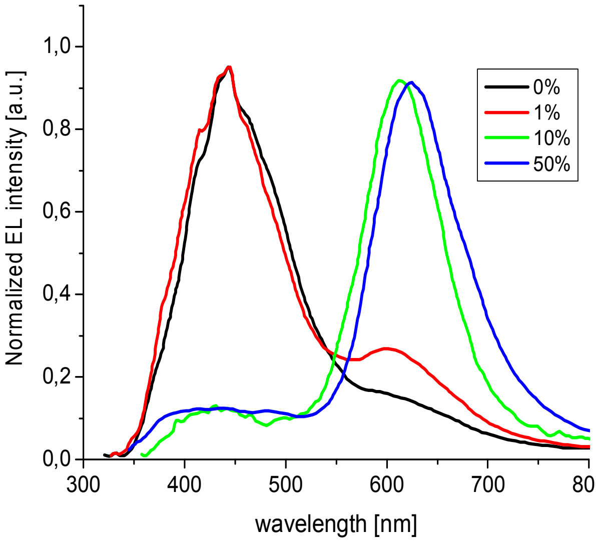

Figure 8.1.6. EL spectra of PVK:G_3 single layer diodes for different G_3 dendron concentrations

In electroluminescence, emission from dopant molecules is often stronger than that in PL in comparison to a polymer matrix emission, due to efficient trapping of charge at dopant sites before exciton generation on the polymer [119, 120]. In our case, comparing the PL and EL spectra of PVK:G_3 blends at different concentrations, we notice that the relative intensities of the polymer and dendron are similar for the both types of emission. This means that excitons are predominantly created at the carbazole polymer sites and then the energy is transferred to G_3 molecules. Consequently, the red emission from the dendron molecules in the polymer matrix is quite stable and is not quenched like in the case of the D:G blends. The low stability of molecular blends might be related to charge transfer reactions induced by electron trapping at acceptor sites which can lead to emission quenching [121, 122].

In order to insert the green component to EL spectrum it was decided to add donor molecules D_n at high concentration (60%w) into OLEDs [123]. Moreover, to obtain a better charge balance in the diode, PVK was mixed with PBD (50% : 50%w), an electron transporting material typically used with PVK matrix [120]. In figure 8.1.7 the EL spectrum of PVK:PBD:D_1 device is shown. The most intense green excimer emission, centred at 500 nm, comes from the pre-associated pyrene units. Additionally, a shoulder at 690 nm can be noticed, present also in the spectra of molecular films (figure 8.1.4). After inserting the 4%w of G_3 molecules into the PVK:PBD:D_1 blend, a band of the acceptor part of G_3 emerged in the electroluminescence together with the simultaneous emission of pyrene excimer. Therefore, in the PVK based matrices due to suitable position of PVK energy levels and those of pyrene units the collective EL emission from the polymer, the donor excimer and the acceptor unit of the dendron can be attained creating together white light.

The white light-emitting device achieved the maximal η_{ext} of 0.05%, CCT = 4260K and CIE chromaticity coordinates (0.36, 0.34) corresponding closely to the equal energy white point.

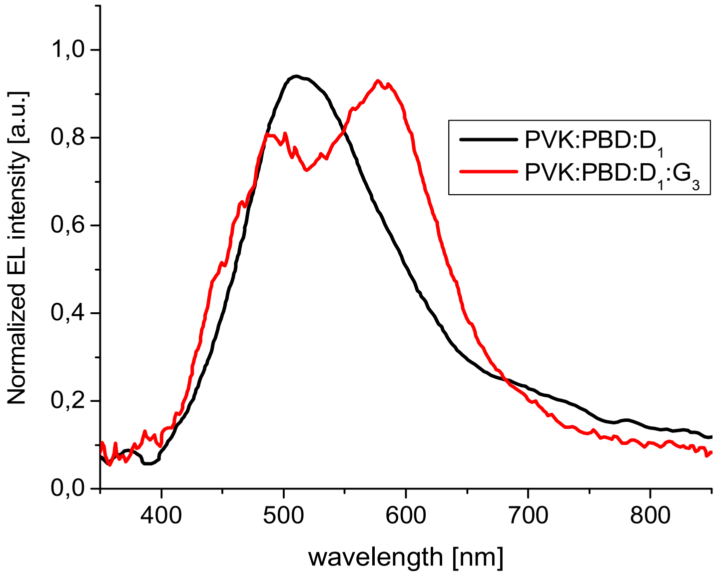

Figure 8.1.7. EL spectra of the devices consisting of D_1 dendron and D_1 : G_3 blend, both in PVK : PBD matrix

8.2. White organic light-emitting diodes with the lanthanide complexes

Absorption spectra of tetrakis β-diketonate terbium complex $Tb(hfa)_4P(Ph)_4$ and tetrakis β-diketonate europium complex $Eu(tta)_4P(Ph)_4$ in dichloromethane are shown in figure 8.2.1. Shapes of the spectra correspond very well to the absorption of (hfa) and (tta) ligands, therefore we can conclude that the ligand centre states are responsible for absorption in the complexes [124, 125].

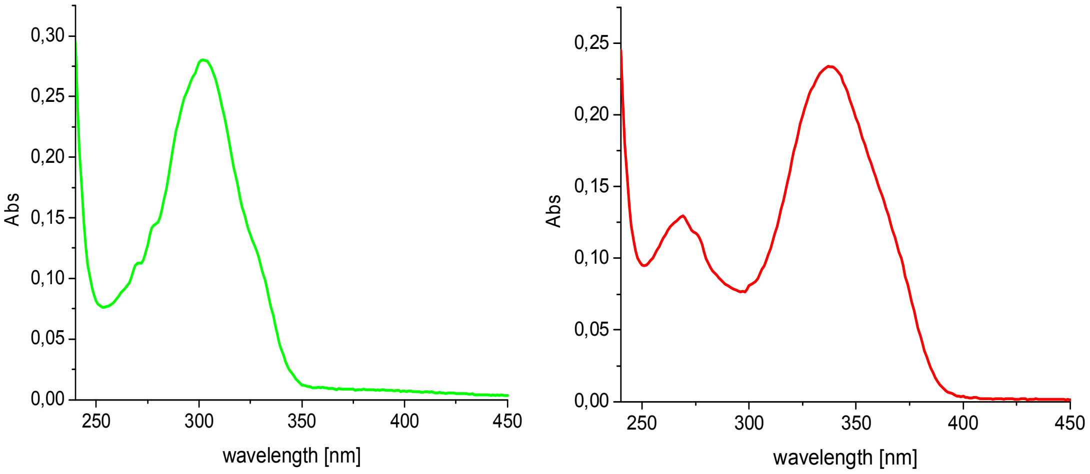

Figure 8.2.1. Absorption spectra of $Tb(hfa)_4P(Ph)_4$ (left) and $Eu(tta)_4P(Ph)_4$ (right) in dichloromethane

In figure 8.2.2 the photoluminescence spectra of the complexes are presented together with labels corresponding to the proper radiative transitions in the lanthanide ions. The emission peaks positions of Tb^{3+} are localized at 489 nm, 545 nm, 585 nm, 622 nm and 655 nm, while the peaks of Eu^{3+} are at 593 nm, 613 nm, 654 nm and 702 nm. The most intense line of the terbium complex is at 545 nm and the one of the europium complex at 613 nm, suggesting employment of these compounds as green and red emitters in OLEDs.

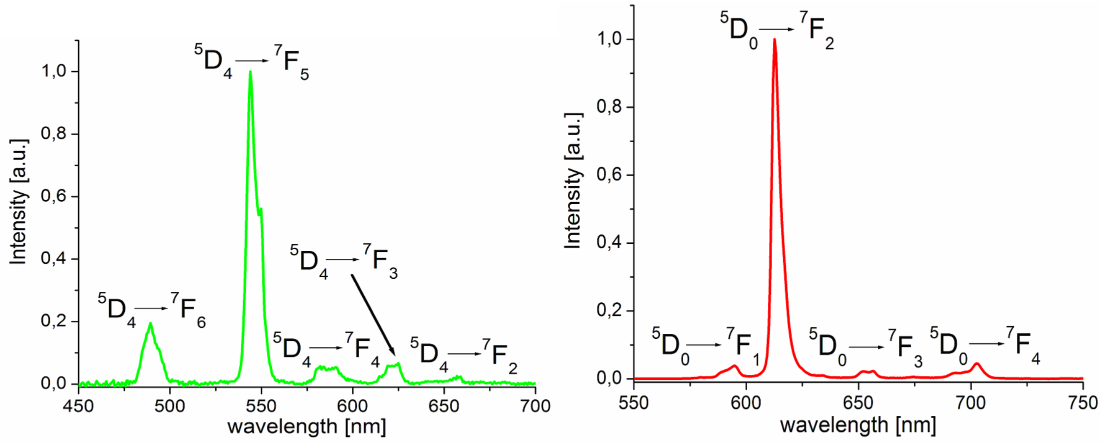

Figure 8.2.2. Photoluminescence spectra of $Tb(hfa)_4P(Ph)_4$ (left) and $Eu(tta)_4P(Ph)_4$ (right) in dichloromethane

In order to evaluate a possible application of the complexes in devices their PL quantum yields were measured in solution and in solid state. Results for $Tb(hfa)_4P(Ph)_4$, $Eu(tta)_4P(Ph)_4$

and also other europium complexes, included as a comparison, are presented in table 8.2.1. The terbium complex revealed low PL quantum yields in the solution and as a cast film, while it was an efficient emitter when in form of powder. Generally, the europium complexes showed quite high quantum yields, but with two interesting features. The europium complex with (hfa) ligand, $Eu(hfa)_4P(Ph)_4$, in the form of both spin-coated film and powder exhibits the quantum yield lower than of complexes with (tta) ligand. This shows that it is not sufficient to have a ligand with singlet and triplet energy levels higher than the relevant level of a lanthanide ion to create an efficient emitter, but also the difference between the levels must be optimized [126]. The second property of the presented complexes is a lack of the influence of different counterions ($P(Ph)_4$, $N(et)_4$, $As(Ph)_4$) on the PL quantum yields of the complexes.

Table 8.2.1. The PL quantum yields of terbium and europium complexes in dichloromethane, dispersed in policarbonate (PC) polymer matrix and as a powder

	Quantum Yield		
Compound	In CH_2Cl_2	10% complex : 90% PC film	Solid state (powder)
$Tb(hfa)_4P(Ph)_4$	1,5%	5% (dropcasting)	55%
$Eu(hfa)_4P(Ph)_4$	44%	6%	43%
$Eu(tta)_4P(Ph)_4$	47%	33%	71%
$Eu(tta)_4N(Et)_4$	48%	34%	64%
$Eu(tta)_4As(Ph)_4$	47%	24%	64%

Encouraged by good quantum yields of $Tb(hfa)_4P(Ph)_4$ and $Eu(tta)_4P(Ph)_4$ complexes we tested them in OLEDs. The EL spectrum of a device having composition of 66% PVK : 30% PBD : 4% $Tb(hfa)_4P(Ph)_4$ and its CIE coordinates are presented in figure 8.2.3. The peaks originating from the Tb^{3+} ion are well visible together with a small contribution from PVK and PBD singlet exciton emissions, possibly mixed with PBD: PVK exciplex and PVK excimer fluorescence [120, 127, 128]. Figure 8.2.4 shows measured electrical characteristics of the device and generally low levels of the efficiency values can be noticed. The external quantum efficiency reached 0.0007%, the luminous efficacy arrived at 0.0016 cd/A and the maximal luminous power efficacy is as high as 0.0006 lm/W. Searching for possible explanations of disappointing results we measured photoluminescence of the diode. The device PL spectrum together with PL of PVK are reported in figure 8.2.5. While in the EL the major emission was from the terbium complex, in the PL the main contribution originates from PVK and only a moderate intensity of the 545 nm peak is observed. This suggests an inefficient energy transfer from the matrix to the complex. The above hypothesis is confirmed by plots in figure 8.2.6, where spectra of the complexes ligands absorption and PL of PBD and PVK are shown. In the figure we notice that overlap of the (hfa) absorption and emission spectra of the

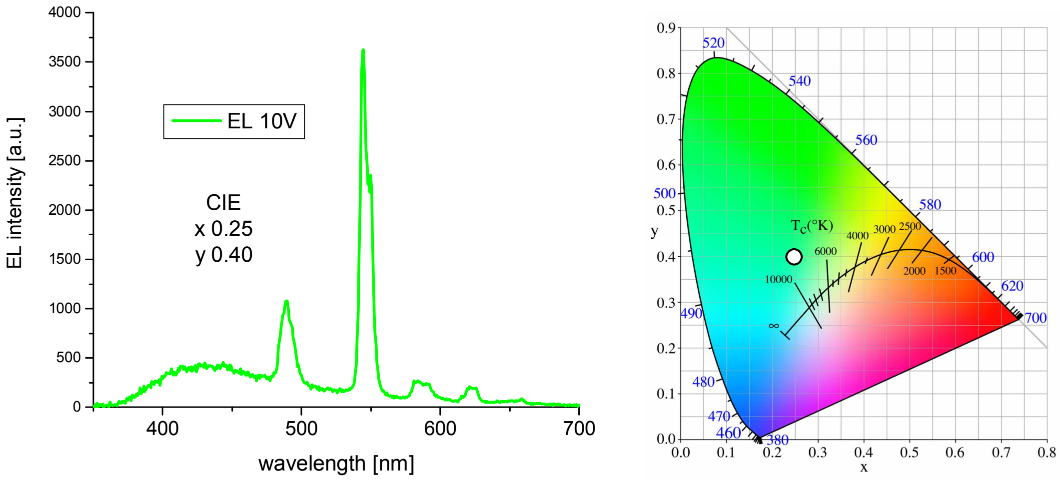

Figure 8.2.3. EL spectrum of 66% PVK : 30% PBD : 4% $Tb(hfa)_4P(Ph)_4$ diode and its CIE coordinates

compounds creating the matrix is negligible and, as a consequence, the requirement for energy transfer is not fulfilled. Therefore, in the green emitting diode the most important mechanism seems to be that of charge trapping. However, looking at figure 8.2.10 where the HOMO and the LUMO levels of used materials are shown we can see that either electrons or holes are not trapped easily on $Tb(hfa)_4P(Ph)_4$ molecules. As a result, the injected charge carriers pass rather through the device instead of being trapped on the emitting centres, which explains low efficiency of the green emitting OLED.

Passing to the red emitting device, it is clear that its operation mechanism is different from that for the green one. In figure 8.2.7 a comparison of EL and PL spectra of 66% PVK : 30% PBD : 4% $Eu(tta)_4P(Ph)_4$ diode is shown. Contrary to the case of OLED with the terbium complex, a very good agreement of the two spectra is observed which suggests an efficient energy transfer. Indeed, the overlap of proper spectra (figure 8.2.6) confirms the presence of this phenomenon. More detailed analysis of energy transfer from the materials forming the matrix to the europium complex will be presented later. Figure 8.2.8 reports the performance characteristics of the red emitting OLED. Though it is more efficient than the one with $Tb(hfa)_4P(Ph)_4$, the efficiency is still below expectations. The maximal values of the external quantum efficiency, luminous efficacy and luminous power efficacy are 0.0135%, 0.024 cd/A and 0.0094 lm/W, respectively. The diode turn-on voltage is 6V, two volts less in comparison to the green emitting device with the terbium complex.

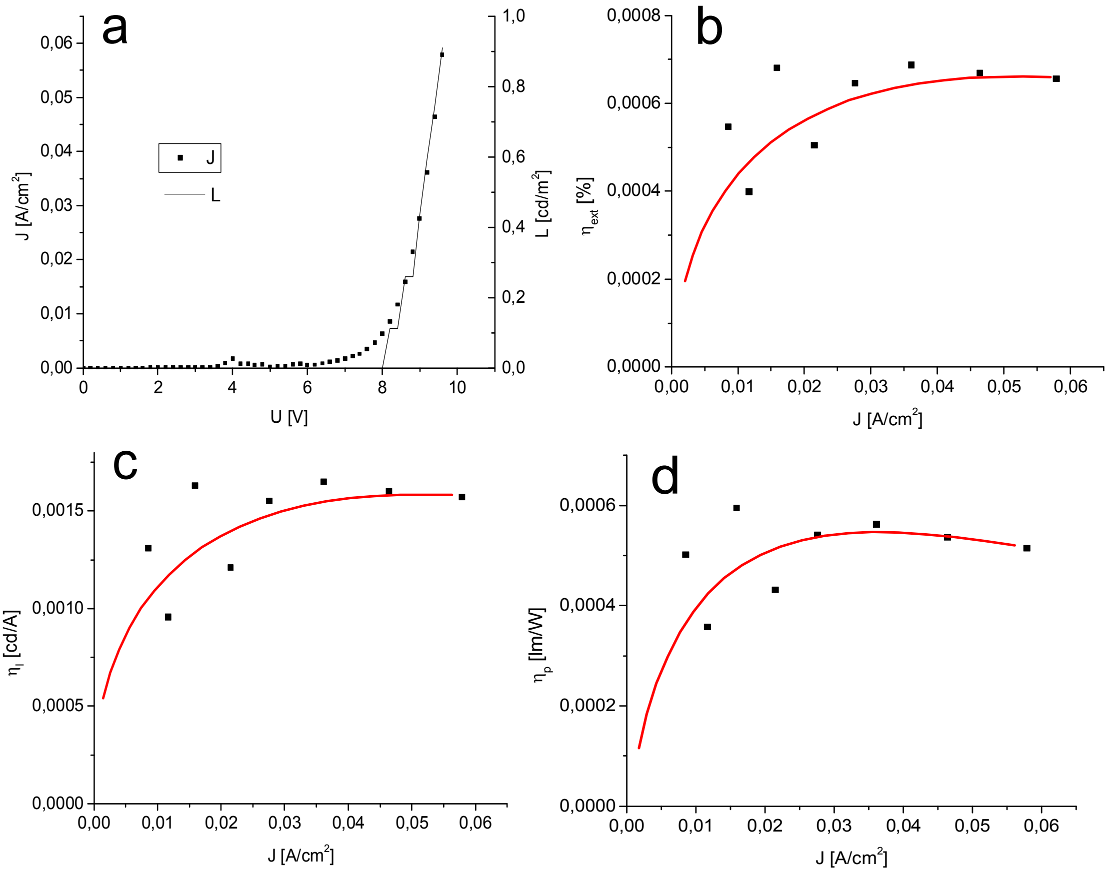

Figure 8.2.4. (a) The current density-voltage-luminance (J-V-L) curves, (b) the external quantum efficiency, (c) the luminous efficacy and (d) the luminous power efficacy of 66% PVK : 30% PBD : 4% Tb(hfa)$_4$P(Ph)$_4$ device. The red lines are for eye guidance only

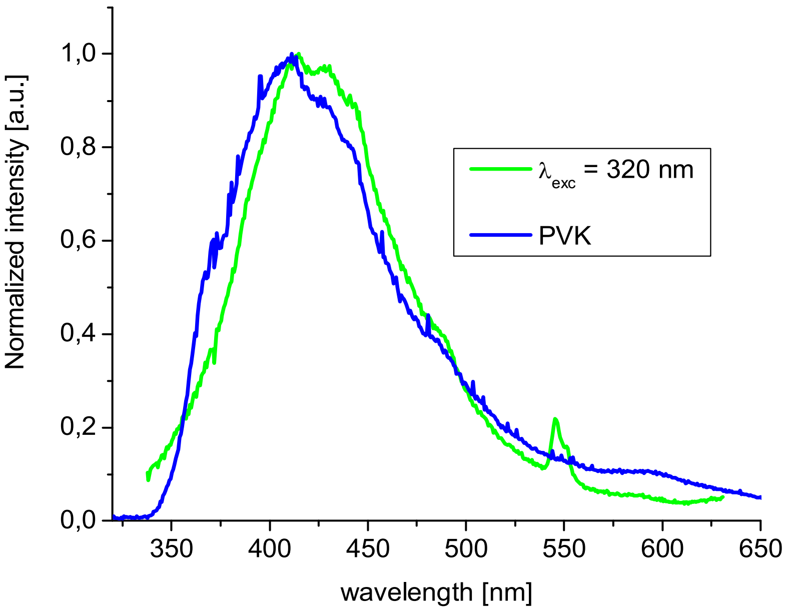

Figure 8.2.5. PL spectra of 66% PVK : 30% PBD : 4% Tb(hfa)$_4$P(Ph)$_4$ OLED and 100% PVK film

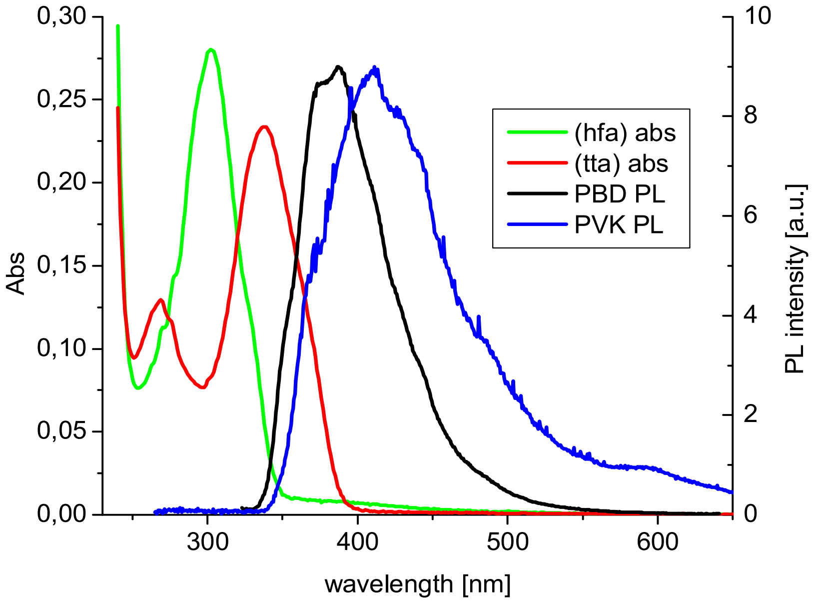

Figure 8.2.6. The overlap of absorption spectra of (hfa) and (tta) ligands and PL spectra of PBD and PVK

Finally, all the compounds were mixed in the ratio of 65% PVK : 30% PBD : 4.5% $Tb(hfa)_4P(Ph)_4$: 0.5% $Eu(tta)_4P(Ph)_4$ in order to create white light. PVK and PBD play a quadruple role in the device, being a matrix for the small-molecule compounds, blue emitters, energy donors for $Eu(tta)_4P(Ph)_4$ and charge transporting materials. PVK mainly transports holes and PBD is an electron transporter introduced here in order to improve a balance between charge carriers. The EL spectrum of the WOLED is presented in figure 8.2.9 where contributions of the green and red emitting OLEDs can be easily distinguished. The CIE coordinates at 14V (x = 0.33, y = 0.38) correspond to white light with green hue which is confirmed by the photograph of emitting diode in the inset of figure 8.2.9.

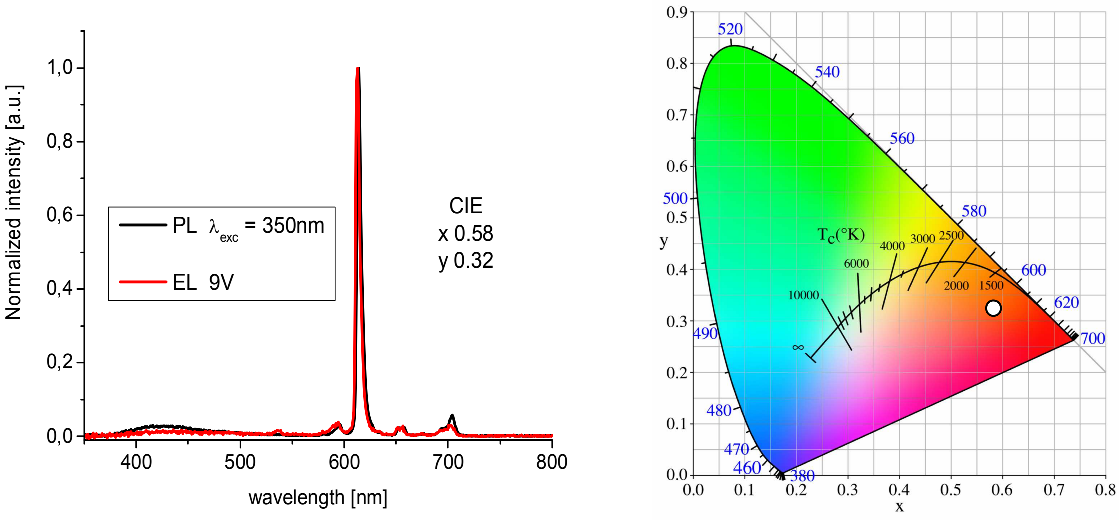

Figure 8.2.7. EL and PL spectra of 66% PVK : 30% PBD : 4% $Eu(tta)_4P(Ph)_4$ diode and the CIE coordinates of the EL spectrum

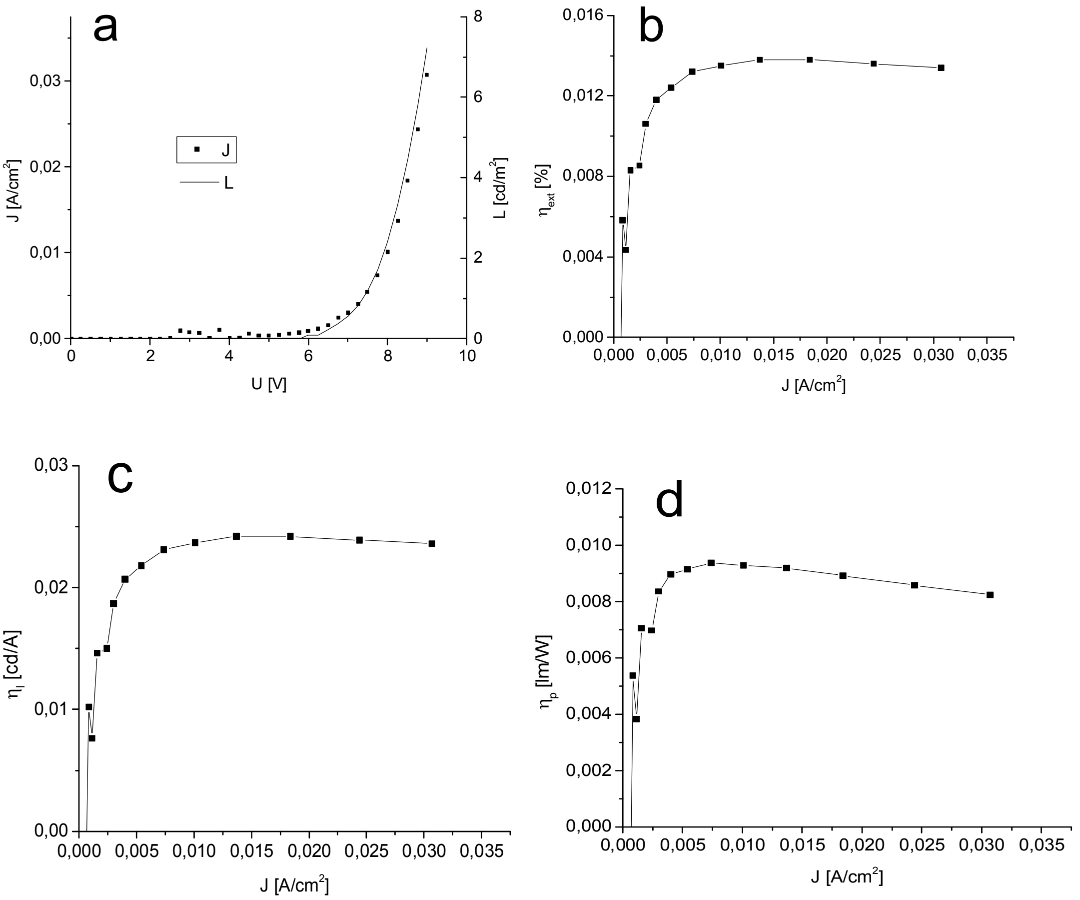

Figure 8.2.8. (a) The J-V-L curves, (b) the external quantum efficiency, (c) the luminous efficacy and (d) the luminous power efficacy of 66% PVK : 30% PBD : 4% Eu(tta)$_4$P(Ph)$_4$ device

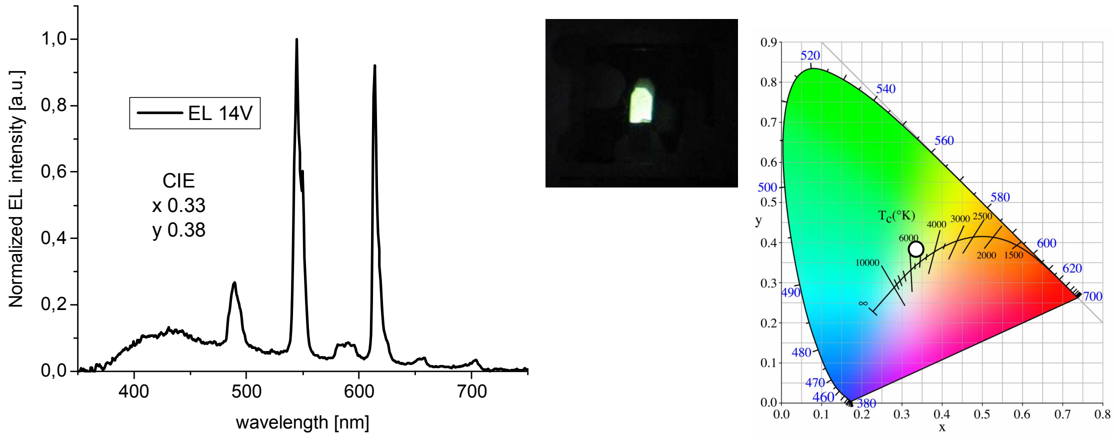

Figure 8.2.9. EL spectrum of 65% PVK : 30% PBD : 4.5% Tb(hfa)$_4$P(Ph)$_4$: 0.5% Eu(tta)$_4$P(Ph)$_4$ device and its CIE coordinates. In the central part a photograph of the emitting WOLED is presented

The calculated correlated colour temperature and colour rendering index are 5460K and 81, respectively, providing a natural daylight for good colour reproduction.

In figure 8.2.10 energy levels of the materials used in the devices are shown. A rather high energy barrier for hole injection between PEDOT:PSS and PVK, being the main hole transporting material in the matrix, together with a barrier for electrons at the PBD/cathode interface and a lack of efficient charge trapping at the lanthanide complexes are the essential reasons for small efficiency of the WOLED. The relevant graphs illustrating the performance of the WOLED are presented in figure 8.2.11. A very rapid decrease of all the efficiencies at the beginning of operation of the device can be noticed with subsequent stabilization of all the parameters. The external quantum efficiency diminished from 0.011% to 0.0015%, the luminous efficacy decreased from 0.025 cd/A to 0.003 cd/A and the luminous power efficacy was reduced ten times from 0.01 lm/W to 0.001 lm/W.

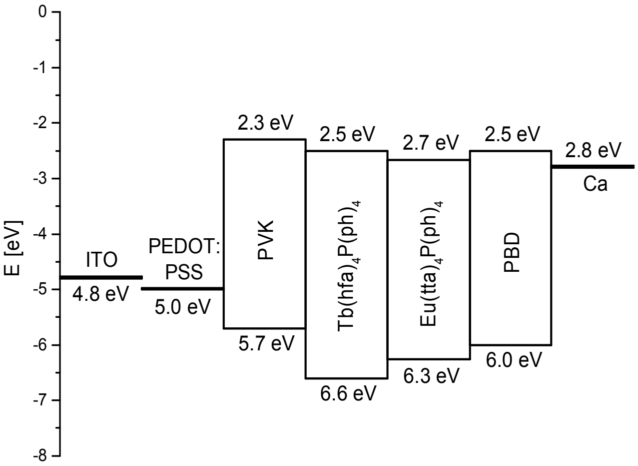

Figure 8.2.10. Energy levels of the materials used in the devices

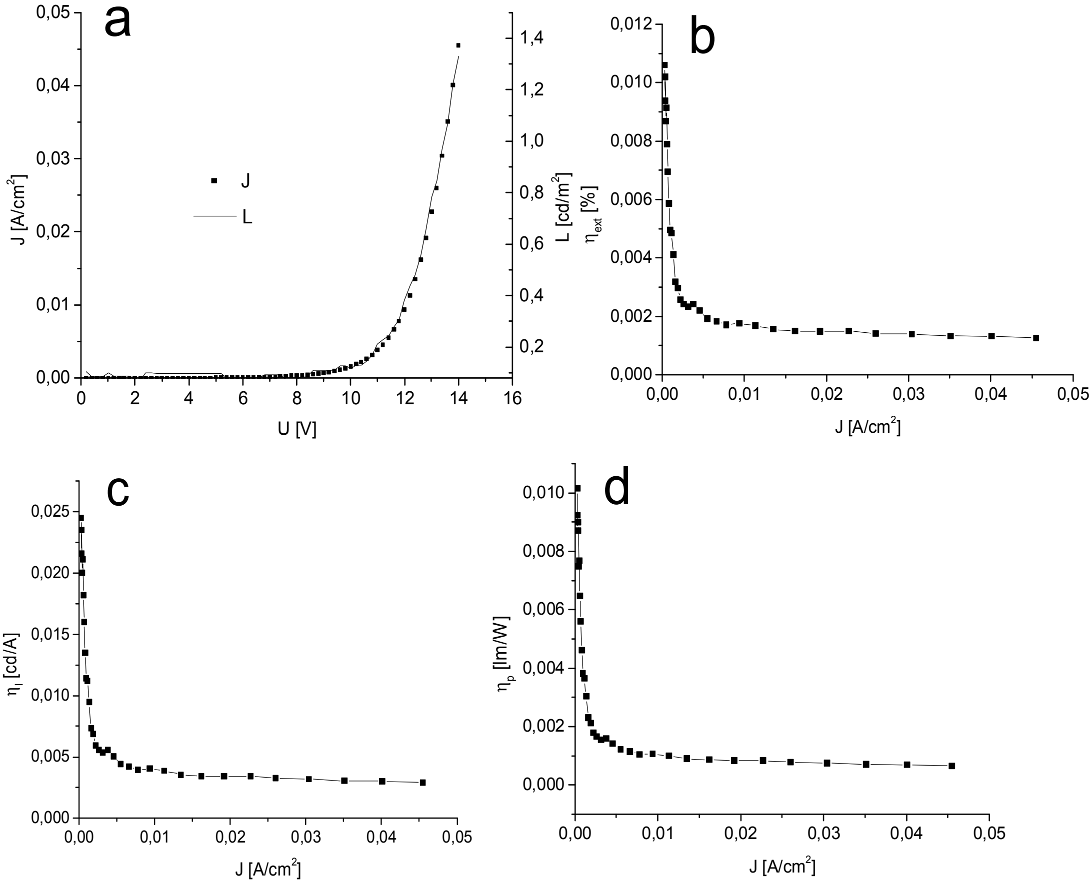

Figure 8.2.11. (a) The J-V-L curves; (b) the external quantum efficiency, (c) the luminous efficacy and (d) the luminous power efficacy of 65% PVK : 30% PBD : 4.5% $Tb(hfa)_4P(Ph)_4$: 0.5% $Eu(tta)_4P(Ph)_4$ device

At this point we will analyze in more detail energy transfer processes that take place in the host-guest mixtures present in OLEDs. We concentrate ourselves on the arrangements containing Eu(tta)$_4$P(Ph)$_4$ since, as was pointed out above, the energy transfer between materials forming the matrix of the devices and the terbium complex is inefficient. Two types of samples were analyzed with different concentrations c of the dopant. The first set had composition c% Eu(tta)$_4$P(Ph)$_4$: (100% - c%) PVK while the second one consisted of c% Eu(tta)$_4$P(Ph)$_4$: 80% PBD : (20% - c%) PC. In the second type of samples bisphenol-A-polycarbonate (PC) was used as an optically and electrically neutral matrix polymer for the small molecules.

We start with determination of Förster radii for the europium complex embodied in PVK and PBD. Assuming an isotropic distribution of acceptors and taking η_{PL}^{PVK} = 0.16, η_{PL}^{PBD} = 0.34 (measured for 80% PBD : 20% PC film), and refractive index n = 1.5 one obtains R_0 = (2.2±0.2) nm and R_0 = (2.9±0.2) nm for doped PVK and PBD:PC films, respectively. Subsequently, a theoretical model based on the steady state PL kinetics was derived for a donor - acceptor system presented in figure 8.2.12. The model assumes that only the donor is excited directly. This statement is justified by the fact that the absorption of Eu(tta)$_4$P(Ph)$_4$ at excitation wavelength (295 nm) has a minimum and concentration of the acceptor is low as compared to the concentrations of hosts. It is also assumed that back transfer from the acceptor to the donor is not operative.

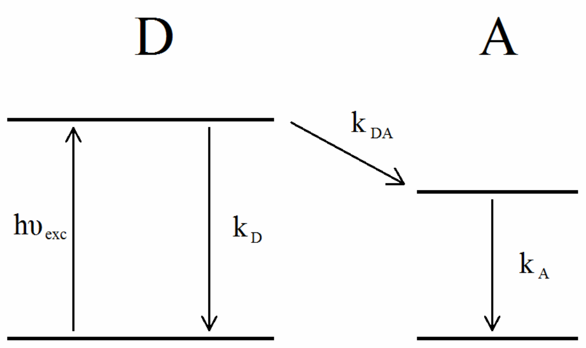

Figure 8.2.12. The possible transitions in a donor - acceptor system used in the model

Equation 8.2.1 describes behaviour of the excited donors at D concentration in a steady state

$$0 = \frac{dD}{dt} = \alpha I_0 - \left(k_D + k_{DA}\right)D = \alpha I_0 - k_{Deff}D\,. \tag{8.2.1}$$

The absorption coefficient α multiplied by the excitation light intensity I_0 describes the generation term, while k_D and k_{DA} are the decay rate constant and the transfer rate constant, respectively, joined into the one effective rate constant k_{Deff}. Note that k_D includes the radiative and nonradiative processes. The acceptor excited states of A concentration do behave according to equation 8.2.2

$$0 = \frac{dA}{dt} = k_{DA}D - k_A A, \tag{8.2.2}$$

from which we find that

$$\frac{D}{A} = \frac{k_A}{k_{DA}}. \tag{8.2.3}$$

In order to find the dependence of the energy transfer efficiency on the acceptor concentration *c* we introduce a function *φ(c)* defined as the ratio of the acceptor luminescence intensity to the total acceptor and donor emission intensity

$$\varphi(c) = \frac{I_A}{I_A + I_D} = \frac{1}{1 + \frac{I_D}{I_A}}. \tag{8.2.4}$$

The intensities of the acceptor and donor emissions are described by formulas 8.2.5

$$I_A = \eta_{PL}^{A} k_A A, \; I_D = \eta_{PL}^{D} k_D D, \tag{8.2.5}$$

where η_{PL}^{A} and η_{PL}^{D} are the PL quantum yields of the acceptor and donor, respectively. Using formula 8.2.3 we calculate the ratio of the two intensities

$$\frac{I_D}{I_A} = \frac{k_D}{k_{DA}} \frac{\eta_{PL}^{D}}{\eta_{PL}^{A}}. \tag{8.2.6}$$

From equation 8.2.1 we find that, $k_{DA} = k_{Deff} - k_D$, and making the substitution of k_{DA} into formula 8.2.6 we obtain

$$\frac{I_D}{I_A} = \left(\frac{k_{Deff}}{k_D} - 1 \right)^{-1} \frac{\eta_{PL}^{D}}{\eta_{PL}^{A}}. \tag{8.2.7}$$

At this point we have to define the effective rate constant k_{Deff}, which contains intrinsic decay of donors without acceptors and also includes donor exciton diffusion and resonant energy transfer to uniformly distributed acceptors. The first who investigated those phenomena were Yokota and Tanimoto in work [129]. Formula for the donor luminance decay derived by them is presented below

$$\xi(c,t) = \exp\left[\frac{-t}{\tau_D} - 2k_1 k_2 \left(\frac{t}{\tau_D} \right)^{\frac{1}{2}} \right], \tag{8.2.8}$$

where $k_1 = c\frac{2\pi^{\frac{3}{2}} R_0^3}{3}$, $k_2 = \left(\frac{1 + 10.87\chi + 15.5\chi^2}{1 + 8.743\chi} \right)^{\frac{3}{4}}$, $\chi = D_S \frac{\tau_D^{\frac{1}{3}}}{R_0^2} t^{\frac{2}{3}}$.

Here τ_D is the lifetime of the donor, *c* denotes the concentration of the acceptor in cm^{-3}, R_0 is the Förster radius and D_S stands for the diffusion coefficient of the donor singlet exciton.

For diffusion and energy transfer mechanisms occuring in the system the rate constants can be rewritten as

$$k_{Deff} = \frac{\int_0^\infty \xi(c,t)dt}{\int_0^\infty t\xi(c,t)dt}, \qquad k_D = \frac{1}{\tau_D}. \tag{8.2.9}$$

Using the result of 8.2.7 and making substitution in 8.2.4 we obtain a formula for *φ(c)* as depending on the acceptor concentration. For given concentration of the acceptor the only fitting parameter is the diffusion coefficient D_S,

$$\varphi(c) = \frac{1}{1 + \left(\frac{\tau_D \int_0^\infty \xi(c,t)dt}{\int_0^\infty t\xi(c,t)dt} - 1 \right)^{-1} \frac{\eta_{PL}^D}{\eta_{PL}^A}}. \tag{8.2.10}$$

Figure 8.2.13 presents function *φ(c)* measured for different concentrations of the acceptor in Eu(tta)$_4$P(Ph)$_4$: PBD : PC system together with theoretical curves calculated with formula 8.2.10 for different values of the diffusion coefficient. In the model η_{PL}^{PBD} = 0.34, R$_0$ = 2.9 nm and τ_D = 770ps (measured for 80% PBD : 20% PC film) were used. The curve calculated under the assumption of D_S = 0 lies below the experimental points which indicates that diffusion is operative in our system. The best fit was obtained for D_S = 6·10^{-5} cm^2/s. This value is comparable with diffusion coefficient D$_S$ = (6±2)·10^{-5} cm^2/s measured in vacuum evaporated amorphous films of tris(8-hydroxyquinoline)aluminium (Alq$_3$) [130] and results obtained for other amorphous materials being in the range of (7·10^{-5} - 4·10^{-3}) cm^2/s [131]. After we have determined the diffusion coefficient, the diffusion path length of singlet excitons in the studied blend can be found. For the case of three dimensional isotropic exciton migration the diffusion path length is described by $l_d = \sqrt{6D_S\tau_D}$. For D_S = 6·10^{-5} cm^2/s and τ_D = 770ps one obtains l_d = 17 nm.

Results obtained for Eu(tta)$_4$P(Ph)$_4$: PVK blend are presented in figure 8.2.14 together with theoretical curves calculated for η_{PL}^{PVK} = 0.16, R$_0$ = 2.2 nm and τ_D = 350ps. From the plot we can conclude that in PVK the diffusion plays a more significant role in energy transfer processes than in the PBD:PC matrix. The best fit was achieved for D_S = 4·10^{-4} cm^2/s. Using this value for calculation of the diffusion path length we obtain l_d = 9 nm. Found by Yang and co-workers, the diffusion coefficient and the diffusion length for PVK are equal 2.5·10^{-4} cm^2/s and

14 nm, respectively (in 3D model), which confirms the validity of our results [132]. For comparison, the diffusion coefficients and diffusion path lengths found for PPV derivatives are in the range ($3 \cdot 10^{-4}$ - $20 \cdot 10^{-4}$) cm^2/s and 15-17 nm, respectively [133].

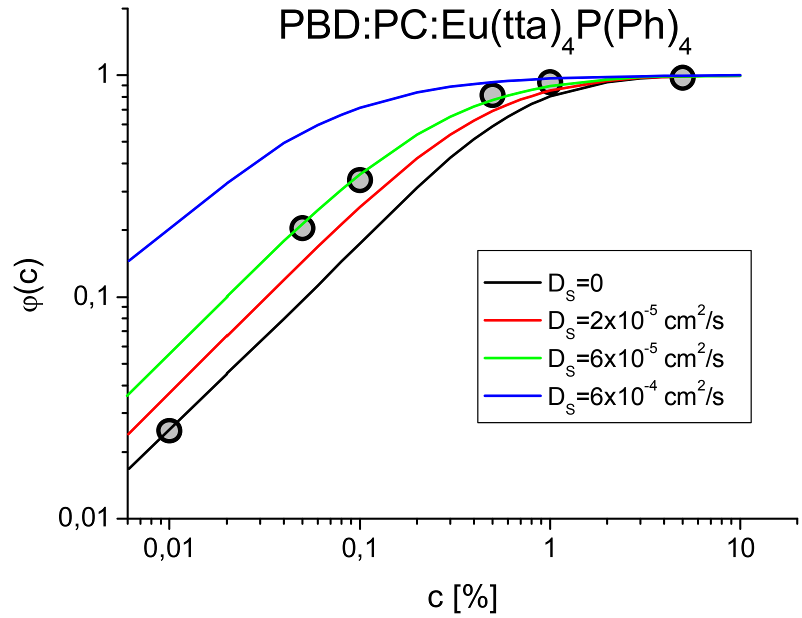

Figure 8.2.13. The dependence of energy transfer efficiency on the acceptor concentration (in wt%) for *c*% $Eu(tta)_4P(Ph)_4$: 80% PBD : (20% - *c*%) PC system

Table 8.2.2 summarizes the values of parameters found in this work and also provides their comparison with those of D_S and l_d measured for other organic materials.

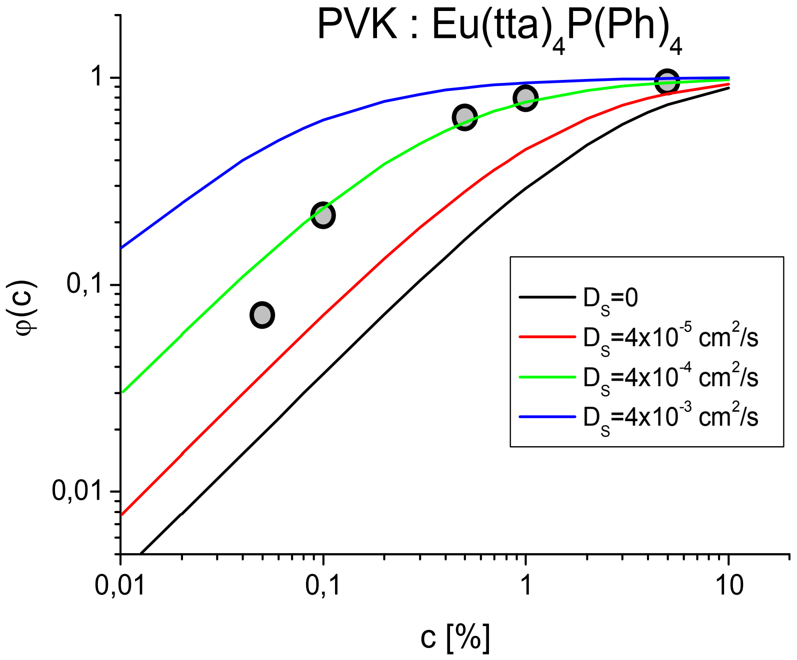

Figure 8.2.14. The dependence of energy transfer efficiency on the acceptor concentration (in wt%) for *c*% $Eu(tta)_4P(Ph)_4$: (100% - *c*%) PVK

Table 8.2.2 The diffusion coefficients and diffusion path lengths of singlet excitons for the systems investigated in this work and for other organic materials

Material	D_S [cm^2/s]	l_d [nm]
Eu(tta)$_4$P(Ph)$_4$: PBD : PC	$6\cdot10^{-5}$	17
Alq$_3$	$(6 \pm 2)\cdot10^{-5}$	23 [130]
NPD	$7\cdot10^{-5}$	5.1 [131]
CBP	$4\cdot10^{-3}$	16.8 [131]
SubPc	$\geq 6.4\cdot10^{-4}$	8.0 [131]
Eu(tta)$_4$P(Ph)$_4$: PVK	$4\cdot10^{-4}$	9
PVK	$2.5\cdot10^{-4}$	14 [132]
NRS-PPV	$3\cdot10^{-4}$	15 [133]
MEH-PPV	$1.1\cdot10^{-3}$	17 [133]
BEH-PPV	$2\cdot10^{-3}$	16 [133]
Naphtalene crystal	$(2 \pm 1)\cdot10^{-4}$ [40]	50 [134]
Anthracene crystal	$(3 \pm 2)\cdot10^{-3}$ [40]	46 [134]
Tetracene crystal	$4\cdot10^{-2}$ [40]	12 [134]

8.3. White electrophosphorescent diodes with organic platinum complex

Absorption and PL spectra of three organic platinum complexes dissolved in dichloromethane are presented in figure 8.3.1. Absorption bands below 300 nm were assigned to the $^1\pi$-π^* transitions localized on the ligands while those between 320-450 nm were attributed to the transitions with mixed character of charge transfer and ligand-centred nature [105, 135, 136]. Very weak absorption bands around 490 nm correspond to the $S_0 \rightarrow T_1$ transitions, partially allowed due to the presence of heavy platinum atom [105, 137].

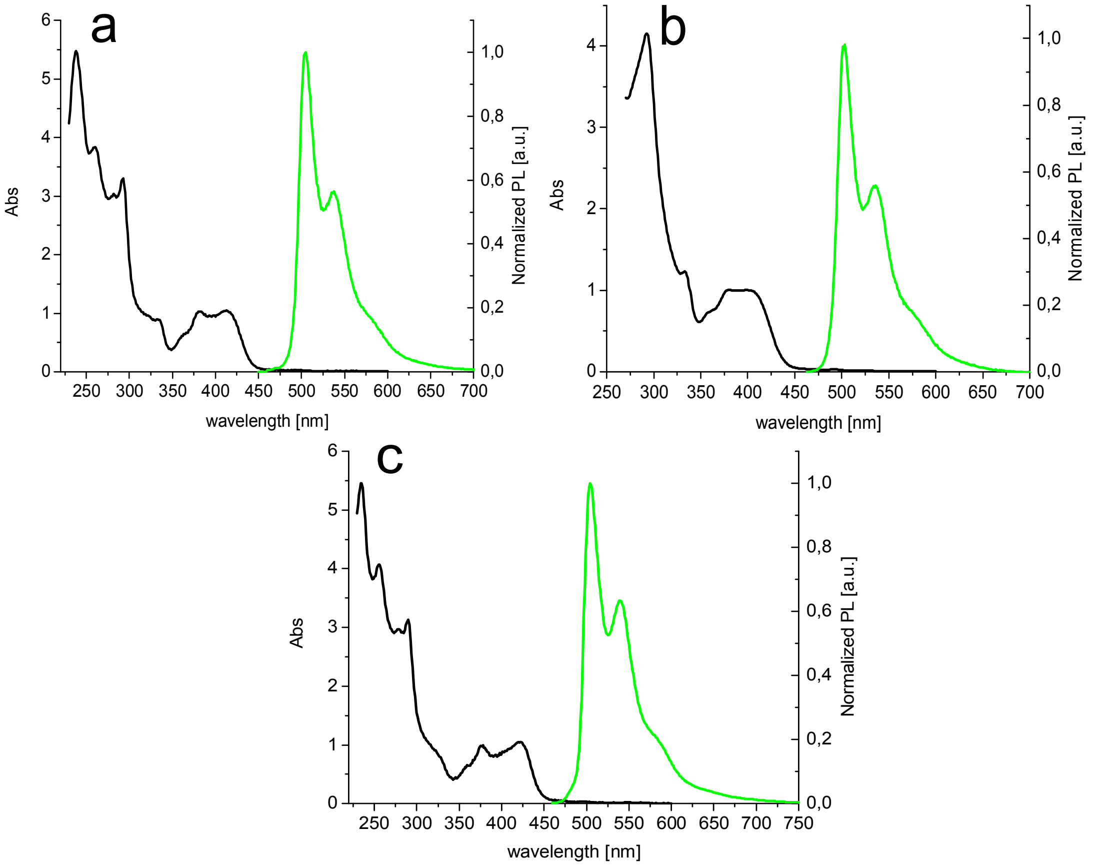

Figure 8.3.1. Normalized absorbance (black) and PL (green) spectra of MePtCl (a), MePtNCS (b) and FPtCl (c) dissolved in dichloromethane

Emission spectra, with well resolved vibrational structure, are essentially the same for all three complexes. Positions of their maxima together with absorption peaks can be found in table 8.3.1. Similarity of the PL spectra seems to be unexpected since it is well known that introduction of electron-withdrawing fluorine atom into a complex causes a blue shift of spectra, as it was observed for *m*-F_2PtCl possessing two fluorine atoms in *meta* positions [138] as well as other types of organometallic complexes [139-142]. These contrasting effects of the F atoms can be understood in terms of frontier orbitals in such complexes. Calculations applying time dependent density functional theory (TDDFT) performed for HPtCl complex, a precursor of the molecules under discussion, showed that the first triplet excited state has predominantly a HOMO-LUMO character [143]. The LUMO is based primarily on the pyridyl rings while the HOMO is predominantly localised on the chloride co-ligand, the platinum ion and on the aryl ring. The fluorine atom attached in *para* position to the metal in FPtCl has a small impact on the HOMO of the complex due to attenuation of the inductive effect by the mesomeric electron-donating effect of F through π orbitals [60]. The F atom has also a small influence on the LUMO as in *para* position there is a small overlap of the electron cloud with this point [144]. Therefore, a substitution of the methyl group by fluorine in *para* position to Pt ion in this family of complexes does not change their emission spectra.

On the other hand, the change of co-ligand from chloride in MePtCl to isothiocyanate in MePtNCS has no significant effect on the emission spectra due to similar positions of the Cl and NCS ligands in the spectrochemical series resulting in no distinctive change in frontier orbitals of such complexes [143].

Table 8.3.1. Photophysical and electrochemical properties of MePtCl, MePtNCS and FPtCl at 298K in dichloromethane

	Absorption λ_{max} / nm (ε / L mol^{-1} cm^{-1})	Emission λ_{max} / nm	η_{PL} ^{a}	τ_0^{b} / μs degassed (aerated)	k_Q^{SQ} / 10^9 M^{-1} s^{-1} ^{b}	k_Q^{O2} / 10^8 M^{-1} s^{-1} ^{c}	k_r (Σk_{nr}) / 10^4 s^{-1} ^{d}	HOMO^{e} / eV	LUMO^{e} / eV
MePtCl	335 (5710) 381 (6900) 412 (6780) 460 (190) 495 (130)	505 539 578	0.68	7.8 (0.3)	3.3	16	8.7 (4.1)	-5.16	-2.53
MePtNCS	333 (4760) 357 (2800) 382 (3890) 406 (3820) 499 (188)	501 533 580	0.60	8.6 (0.7)	8.9	6.2	7.0 (4.6)	-5.04	-2.59
FPtCl	322sh (6170) 377 (7740) 422 (8270) 486 (312)	504 542 580	0.47	6.3 (0.6)	5.6	7.4	7.4 (8.5)	-5.36	-2.61

[a] The luminescence quantum yield in degassed solution. [b] The τ_0 is the lifetime at infinite dilution and k_Q^{SQ} - the self-quenching rate constant determined from the intercept and slope, respectively, of measured emission decay rate constant plotted against solution concentration. [c] The bimolecular rate constant for quenching by molecular oxygen as estimated using the lifetimes in degassed and air-equilibrated solutions, and taking $[O_2] = 2.2 \times 10^{-3}$ M in CH_2Cl_2 at 1 atm pressure of air. [d] Estimates of the radiative k_r and non-radiative (Σk_{nr}, in parenthesis) decay constants are made as follows: $k_r = \eta_{PL} / \tau_0$. $\Sigma k_{nr} = (1/\tau_0) - k_r$. [e] Calculated from the redox potentials

As can be seen in table 8.3.1, the PL quantum yields of the complexes in degassed dichloromethane are relatively high being in the range of 50 - 70%, and are comparable to the values obtained for other complexes of the same family [135]. Such high quantum yields are obtained despite the long lifetimes of radiative decays which suggests that the non-radiative processes in those complexes are strongly suppressed, probably due to high rigidity of the molecular skeleton and high ligand-field strength associated with N^C^N-coordinated ligand.

Lifetimes in the range of microseconds together with the quenching effect of oxygen confirm that we deal with phosphorescence as the emission mechanism. Based on the measured PL quantum yields and lifetimes, radiative and non-radiative rate constants were estimated for the three Pt complexes (it was assumed that the emitting state is created with 100% efficiency). The calculated radiative rate constants are similar to other ones obtained for complexes of the same family [135]. On the other hand, the values of k_r are about one order of magnitude smaller in comparison to those of Ir(ppy)$_3$, probably the most widely studied green phosphorescent complex [145]. However, the non-radiative rate constants for the Pt complexes are 4-5 times smaller than those for Ir(ppy)$_3$.

In table 8.3.1 the HOMO and LUMO energy values for the complexes can be also found. As expected for higher electron withdrawing effect of F atom in comparison to a methyl group, FPtCl is more difficult to oxidize and more easily to reduce with respect to MePtCl. This caused a shift of the HOMO and LUMO energies of FPtCl toward higher values compared to MePtCl.

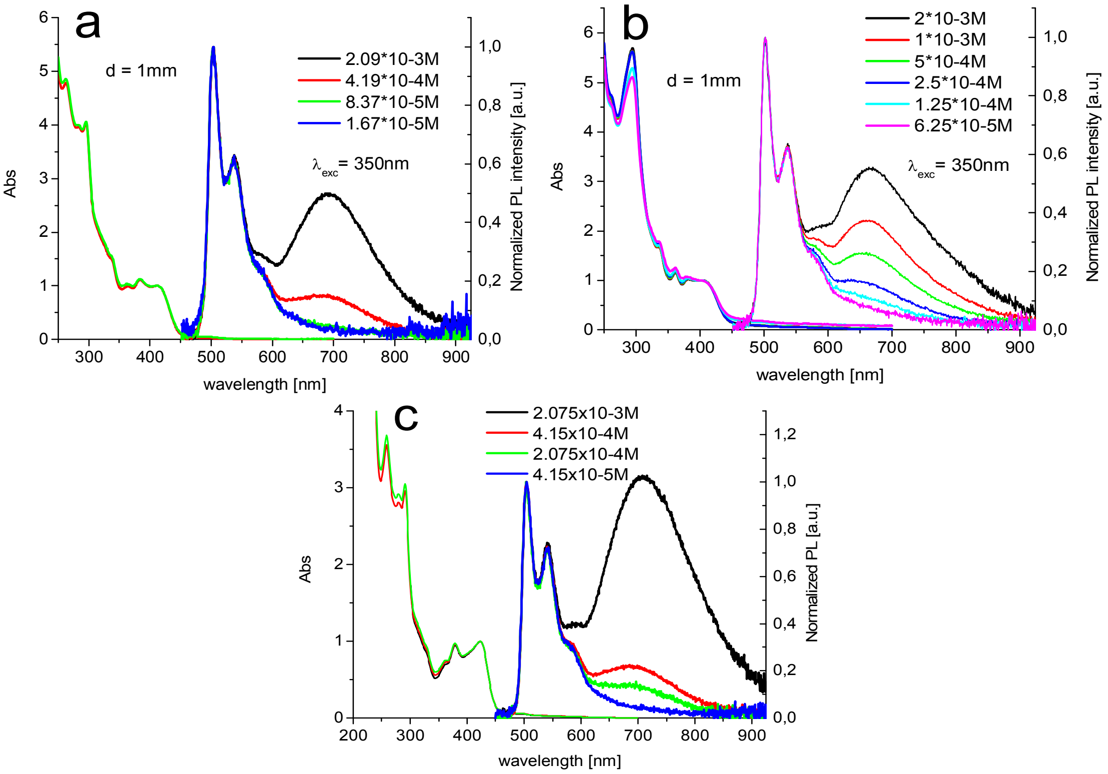

Figure 8.3.2. Absorption and PL spectra of MePtCl (a), MePtNCS (b) and FPtCl (c) in dichloromethane as a function of concentration

As can be seen in figure 8.3.2, the absorption spectra of the complexes under study are insensitive to increasing concentration while the PL ones show appearance of a broad structureless band at longer wavelengths. This new emitting state was ascribed to excimer emission of the complexes as was already observed for other members of this family of molecules [105, 135].

In order to test the performance of the complexes in electroluminescent diodes, devices with simple structure, ITO / PEDOT:PSS / 65% PVK : 30% PBD : 5% Pt complex / Ca / Al, were

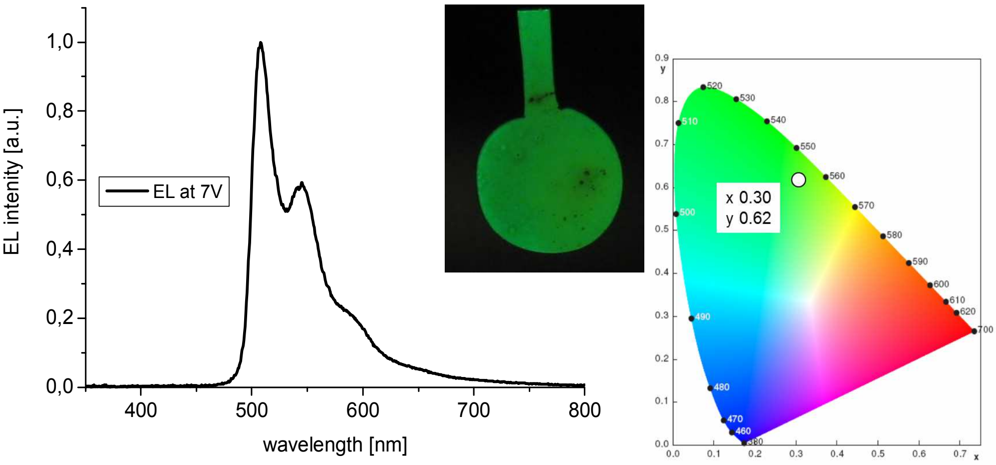

Figure 8.3.3. EL spectrum of the diode having 65% PVK : 30% PBD : 5% FPtCl weight ratio as emitting layer (left), a photograph of the emitting device (centre) and its chromaticity coordinates (right)

built. Results obtained for the OLED containing FPtCl as an emitter are presented as an example. As can be seen from figure 8.3.3, the EL spectrum resembles the photoluminescence spectrum of the complex while the UV-blue emission of PBD or PVK is not detected. Despite high quantum yield of the applied emitter the performance of the diode is quite poor as can be observed in figure 8.3.4. Note that from the current density-voltage-luminance (J-V-L) curves an unstable current behaviour between 3 and 6 volts can be seen. This is often observed property of devices containing PVK as a host matrix. Moreover, as seen from the results from the inset in figure 8.3.4, the device luminance does not depend linearly on the current density in almost the whole operating current range. Instead of it one can see the luminance points lying below the best-fit straight line plotted for current intensities of maximal external quantum efficiency. Such a behaviour at higher current densities is typical for OLEDs, however, a similar behaviour observed for small values of current is a symptom of unbalanced current in the device at the beginning of its operation. As a consequence, the maximal EL efficiencies do not reach high values and achieve only the η_{ext} of 0.05%, the luminous efficacy of 0.16 cd/A of and the luminous power efficacy of 0.045 lm/W.

In order to improve the performance of the devices the multilayer structure was employed. In comparison to a single layer architecture (we consider PEDOT:PSS as a part of an ITO covered substrate) a multilayer diode exhibits numerous advantages (see chapter 5). Additionally, it was possible to build an organic stack structure by applying solely the spin-coating technique which is much cheaper than the commonly used thermal evaporation and paves the way to large-area OLEDs.

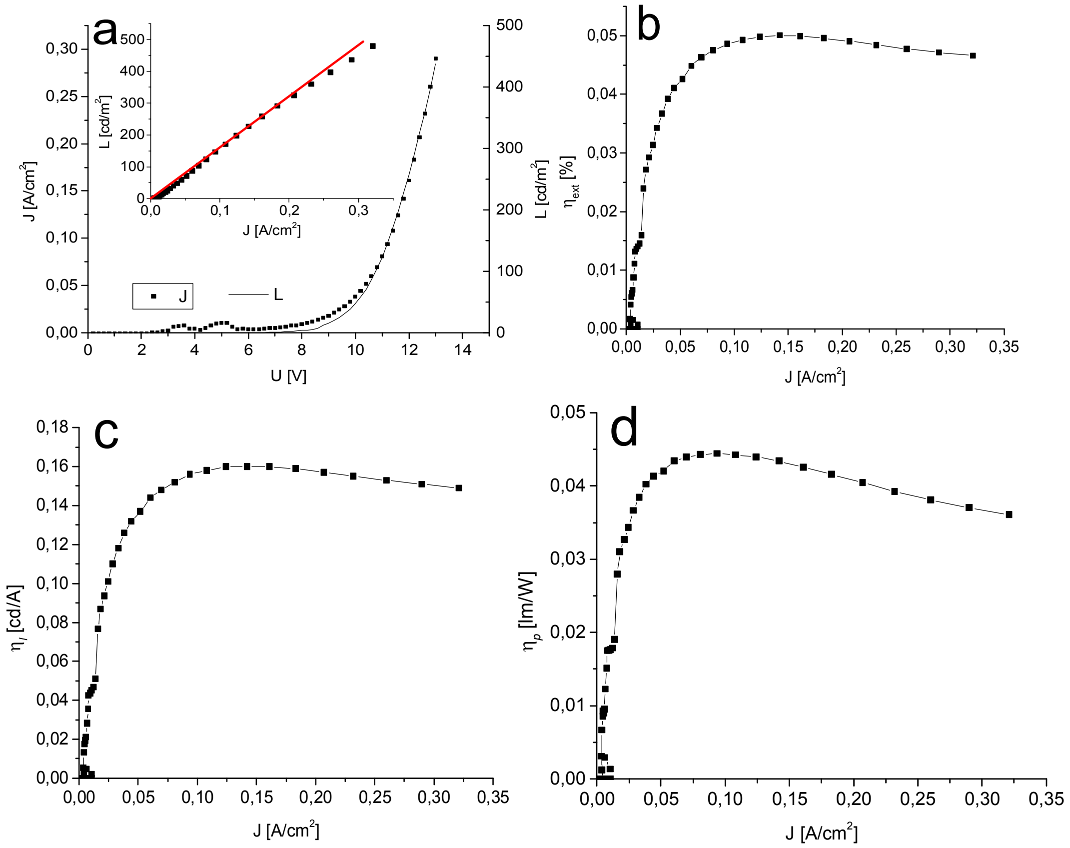

Figure 8.3.4. The current density-voltage-luminance (J-V-L) curves (a) as well as the external quantum efficiency (b), the luminous efficacy (c) and the luminous power efficacy (d) as a function of current density for 65% PVK : 30% PBD : 5% FPtCl diode. In the inset the dependence of the luminance on current density is shown. The red straight line is a fit to the data for the current range of the maximal external quantum efficiency

As a hole transporting layer (deposited on PEDOT:PSS) polyvinylcarbazole (PVK-h) of high molecular weight was chosen. This polymer is well-known as a hole transporting material [146], also preventing excitons from quenching by PEDOT:PSS by separating the emissive layer from the PEDOT:PSS film [147]. Another advantage when using PVK-h is an increase in the distance between the anode and the emissive layer which in turn decreases creation of plasmons in the electrode [83, 148]. High molecular weight of PVK-h (10^6 g/mol) together with its thermal treatment allows to build a hole transporting layer of diminished solubility and makes it possible to deposit an emissive layer from solution onto it. The top (emissive) layer, as in our previous device, was composed of 65% PVK : 30% PBD : 5% Pt complex. As a cathode barium was used instead of calcium which should remove the injection barrier for electrons. Note that the barium work function is as high as 2.4 eV while the LUMO level of PBD is placed 2.5 eV below the vacuum level.

The EL spectra of the devices prepared in the above-described way are presented in figure 8.3.5, together with energy levels of used materials.

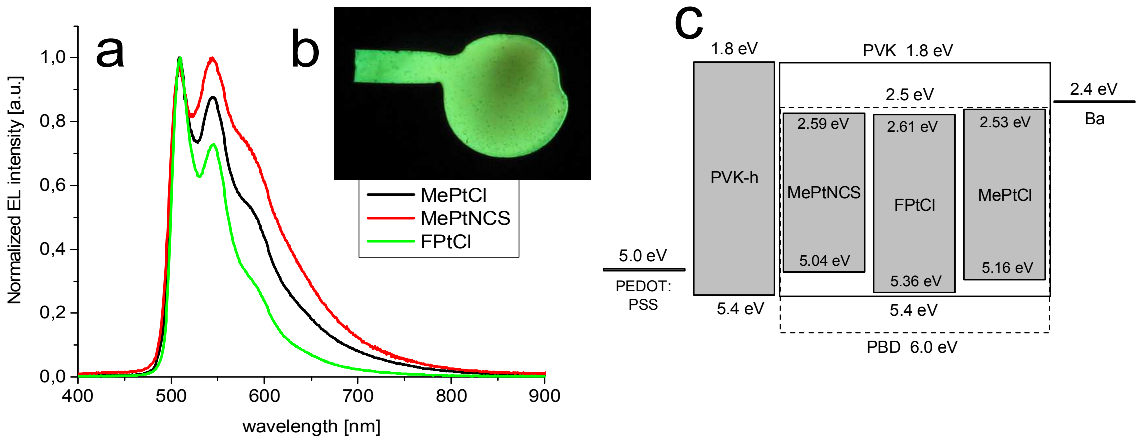

Figure 8.3.5. (a) EL spectra of PVK-h / 65% PVK : 30% PBD : 5% Pt complex devices: MePtCl (black), MePtNCS (red), FPtCl (green); (b) a photograph of the OLED with FPtCl as an emitter; (c) the HOMO and LUMO energy levels of the materials used in a double layer configuration

The EL spectra of the double layer diodes are in principle similar to the PL spectra of diluted solutions and the single layer devices. The difference is visible around 600 nm where a new long-wavelength component is superimposed on the emission of the complexes (this feature will be examined in more detail later on).

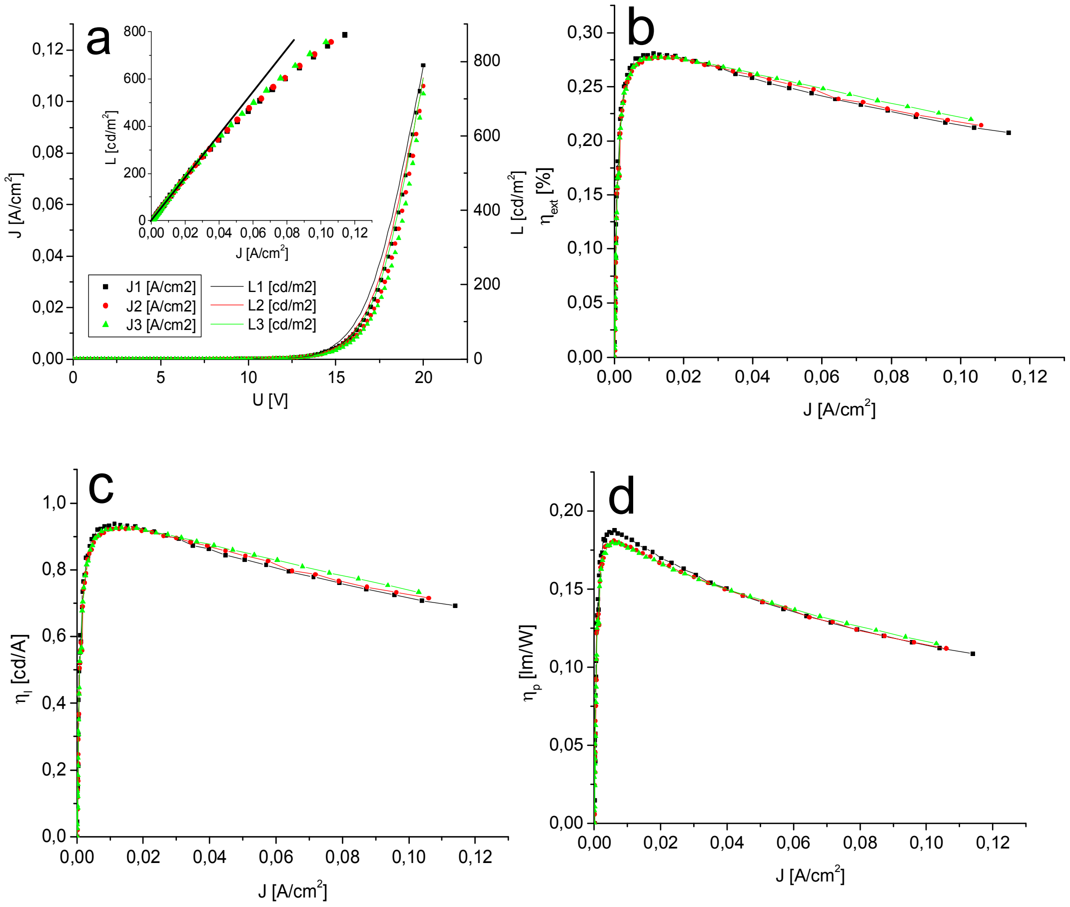

Figure 8.3.6. The current density-voltage-luminance (J-V-L) curves (a) as well as the external quantum efficiency (b), the luminous efficacy (c) and the luminous power efficacy (d) as a function of current density for PVK-h / 65% PVK : 30% PBD : 5% FPtCl diode. In the inset the dependence of the luminance on current density is shown and the black straight line is a fit to the data for the current range of the maximal external quantum efficiency

The performance of the double layer architecture devices improved significantly in comparison to the single layer ones, an example for the OLED with FPtCl as an emitter is presented in figure 8.3.6. The luminous efficacy and the luminous power efficacy achieved 0.94 cd/A and 0.18 lm/W, respectively, which is almost six times better than the luminous efficacy and four times better than the luminous power efficacy of the single layer device. A summary of the results obtained for all three diodes is presented in table 8.3.2.

The dependence of luminance on current density for the double layer device is different than that for the single layer OLED. In the latter case (cf. the inset of fig. 8.3.4) we observed that the luminance points were mostly below a straight line, while now the linear dependence starts from the lowest values of the current (figure 8.3.6 inset). Thus, the external quantum efficiency boosts from 0.05% for the single layer device to 0.28% for the double layer one. The luminous efficacy achieved 0.94 cd/A and 0.18 lm/W of the luminous power efficacy. Reproducibility of measurements was good, confirming the stability of the device. The turn-on voltage increased from 7V to 12V due to higher thickness of the double layer diode in comparison to the single layer device.

Table 8.3.2. Performance of the devices based on MePtCl, MePtNCS and FPtCl, with layer structure in the form of PVK-h / 65% PVK : 30% PBD : 5% Pt complex

	MePtCl	**MePtNCS**	**FPtCl**
V_{on} / V	18	15	12
$\eta_{ext}{}^{a}$ / %	0.23	0.21	0.28
L^{b} / cd m^{-2}	21	17	91
$\eta_{lc}{}^{b}$ / cd A^{-1}	0.68	0.62	0.94
$\eta_{p}{}^{b}$ / lm W^{-1}	0.097	0.11	0.18
L_{max} / cd m^{-2}	195	161	755
CIE (*x*, *y*)	(0.37, 0.58)	(0.39, 0.55)	(0.32, 0.61)

[a] The maximal external quantum efficiency. [b] At the maximum of external quantum efficiency

At this point we will discuss in more detail behaviour of the external quantum efficiency by applying theoretical models that explain a decrease of η_{ext}. In figure 8.3.7 the external quantum efficiency is shown as a function of current density in double logarithmic scale. The experimental data were explained by the triplet-triplet annihilation model (TTA), as proposed by Baldo and co-workers [149] and Kalinowski and co-workers [150].

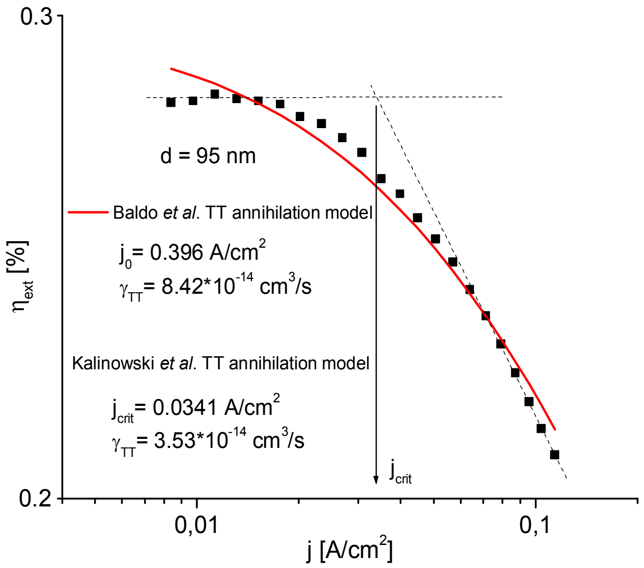

Figure 8.3.7. The external quantum efficiency as a function of current density. The red line shows the best fit to formula 8.3.2

The model is derived from the comparison between two kinetic formulas, without and with TTA operating mechanism:

$$\frac{dT}{dt}=\frac{j}{ed}-k_rT\ ,\ \frac{dT}{dt}=\frac{j}{ed}-k_rT-\frac{1}{2}\gamma_{TT}T^2\ , \tag{8.3.1}$$

where T is the concentration of triplet excitons, j denotes the current density, e stands for the elementary charge, d is the thickness of recombination zone, k_r denotes the radiative decay rate constant and γ_{TT} is the bimolecular rate constant describing annihilation of triplets. From steady state solutions we obtain [149]

$$\frac{\eta_{ext}}{\eta_{ext}^0}=\frac{j_0}{4j}\left(\sqrt{1+\frac{8j}{j_0}}-1\right),\ j_0=\frac{4edk_r^2}{\gamma_{TT}}\ , \tag{8.3.2}$$

where η_{ext}/η_{ext}^0 is the ratio of the external quantum efficiencies with and without triplet annihilation, respectively, and j_0 is the onset current density at which $\eta_{ext}=\eta_{ext}^0/2$. Taking the k_r value of FPtCl from table 8.3.1 and assuming the recombination zone in the top layer of the device (d = 165 nm - 50 nm (PEDOT:PSS) - 20 nm (PVK-h) = 95 nm) we obtain $\gamma_{TT} = 8.4\cdot10^{-14}$ cm^3/s from the best fit to the data in figure 8.3.7.

Calculation of the triplet annihilation constant on the base of the second method requires application of formula

$$\gamma_{TT}=\frac{ed}{j_{crit}}\left(\frac{R_{out}\eta_{PL}}{2\eta_{ext}\tau_0}\right)^{-2}\ , \tag{8.3.3}$$

where j_{crit} corresponds to the current density at which horizontal line representing the maximal low-current level of η_{ext} intersects with a line fitted to the data with operating TTA (see figure

8.3.7), R_{out} is the outcoupling factor (=0.2), η_{PL} denotes the PL quantum yield and τ_0 denotes the intrinsic lifetime. For the recombination zone width of 95 nm and the values of η_{PL} and τ_0 taken from table 8.3.1 we get $\gamma_{TT} = 3.5 \cdot 10^{-14}$ cm^3/s.

It is worth to compare the obtained results with values of γ_{TT} for phosphorescent materials calculated by other authors. In table 8.3.3 the annihilation constants for molecules PtOEP, Ir(ppy)$_3$ and our FPtCl are gathered.

Table 8.3.3. Triplet-triplet annihilation constants for the selected phosphorescent emitters

	γ_{TT} [cm^3/s]
PtOEP	$3 \cdot 10^{-14}$ [149]
Ir(ppy)$_3$	$3 \cdot 10^{-12}$ [121]
Ir(ppy)$_3$	$1 \cdot 10^{-14} \le \gamma_{TT} \le 2.5 \cdot 10^{-13}$ [150]
FPtCl	$8.4 \cdot 10^{-14}$ (eq. 8.3.2) $3.5 \cdot 10^{-14}$ (eq. 8.3.3)

From the table it is seen that our values are in reasonable agreement with those obtained previously and that the γ_{TT} values calculated for FPtCl with the use of the two methods are consistent with each other.

Finally, we should consider possible origins of uncertainty of our γ_{TT} estimation. These are the assumed values of recombination zone thickness and the lifetime of emitting states. The exact thickness of the recombination zone is difficult to determine and we assumed that it spreads over the whole emissive layer. The influence of the recombination zone thickness on the values of γ_{TT} for Ir(ppy)$_3$ was examined in reference [150] where d was assumed to change from 2 nm (recombination at the interface) to 50 nm (homogenous recombination in the whole emissive layer). As a result, the annihilation constant changes more than one order of magnitude (see table 8.3.3). The lifetime of triplets can have even greater impact on the final result since this quantity appears in the second power in the employed formulae. Applied by us the radiative rate constant k_r was measured for a solution and with optical excitation but, optimally, it should be derived for a solid state under electrical excitation.

Another possible explanation of a decrease (roll-off) in η_{ext} of organic LEDs is an interaction of triplet excitons with polarons (the Tq annihilation) which is described by equation 8.3.4, where n_t is the density of trapped charge carriers and γ_{Tq} denotes the second-order triplet-polaron interaction rate constant.

$$\frac{dT}{dt} = \frac{j}{ed} - \left(k_r + \gamma_{Tq} n_t\right) T \tag{8.3.4}$$

Based on equations 8.3.1 and 8.3.4 we calculate the ratio of the external quantum efficiencies with and without Tq annihilation. The resulting formula is

$$\frac{\eta_{ext}}{\eta_{ext}^{0}} = \frac{1}{1 + \frac{\gamma_{Tq}}{k_r} n_t} . \tag{8.3.5}$$

Based on the assumption that the maximal total charge *Q* injected into a device under space charge limited current (SCLC) conditions can be expressed as *Q* ≈ *CU*, where *C* is the electrical capacitance of the sample and *U* is the applied voltage, the density of filled traps should be proportional to the applied voltage *U* [40]

$$n_t = aU , \tag{8.3.6}$$

with a being a constant. From the SCLC theory we know also the relation between the current density *j* passing through a device and the applied voltage

$$j = AU^{l+1}, \tag{8.3.7}$$

where l is the dimensionless parameter describing the assumed exponential distribution in energy of traps. After substitutions we obtain a formula for external quantum efficiency with operating Tq annihilation mechanism, dependent on the current density, [149]

$$\frac{\eta_{ext}}{\eta_{ext}^{0}} = \frac{1}{1 + \alpha j^{\frac{1}{l+1}}} . \tag{8.3.8}$$

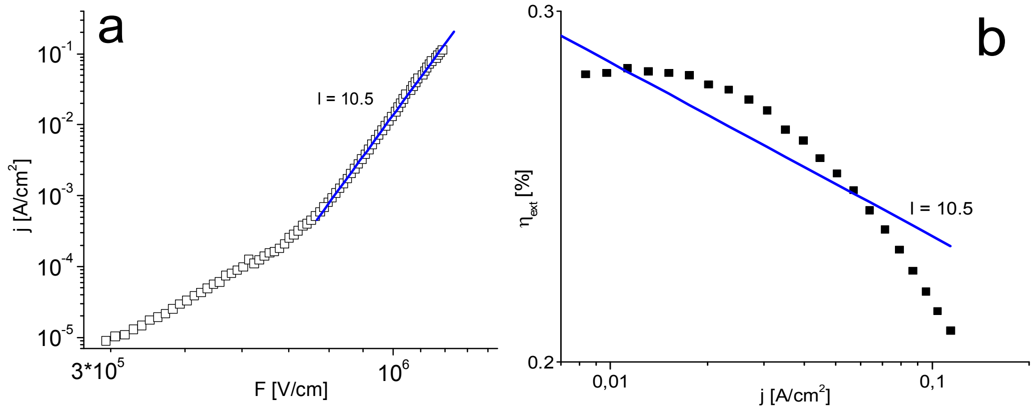

Figure 8.3.8. (a) The current density as a function of external electric field. The solid line shows the best fit to the experimental data, using formula 8.3.7, with parameter *l*, as indicated in the figure. (b) The external quantum efficiency as a function of the current density and the best fit using formula 8.3.8

Figure 8.3.8a shows in a double logarithmic scale the dependence of the current density *j* on the applied external electric field *F,* while figure 8.3.8b presents the external quantum efficiency η_{ext} as a function of the current density. In the figure with the current density two regions can be identified. Each one could be fit with a straight line, according to formula 8.3.7, however in the low-field range the current is most probably controlled by barrier potential at the electrodes. For the high-field regime in turn the current is volume-controlled and linear fit gives l

= 10.5. Subsequently, the η_{ext} roll-off was fit with formula 8.3.8 assuming l = 10.5. Poor agreement of the model and the experimental data can be noticed suggesting that the Tq annihilation is not dominant mechanism responsible for the η_{ext} roll-off.

From the parameter l we are able to calculate the energy of trap levels present in our system, according to formula $E_l = lkT$, where E_l describes the exponential distribution in energy of trap states, k stands for Boltzman's constant and T is temperature expressed in kelvins. For l = 10.5 we obtain E_l = 0.26 eV corresponding to rather deep energy traps.

Using another approach to the Tq-based η_{ext} roll-off we can calculate the γ_{Tq} rate constant from the best fit to formula [150]

$$\eta_{ext} = \frac{2}{3}\frac{P_T R_{out}(1-\eta)\eta_{PL} et}{\varepsilon_0 \varepsilon_r \gamma_{Tq} \tau_0}\frac{w_e}{d}\frac{1}{F}, \tag{8.3.9}$$

where P_T is the probability of triplet excited state formation under electrical excitation (for Pt complexes $P_T \approx 1$), η denotes the probability of charge pair dissociation (we assume $\eta = \eta_0 \Omega \approx \Omega = 0.1$ for this range of electric field), t stands for the device thickness, ε_0 is the permittivity of vacuum, ε_r (=3) denotes the dielectric constant of an organic film, w_e stands for the emission zone thickness, d denotes the recombination zone width and F is the external electric field strength and all other symbols have previously defined meanings. In figure 8.3.9 the external quantum efficiency as a function of the inverse external electric field and the best fit to formula 8.3.9 are presented.

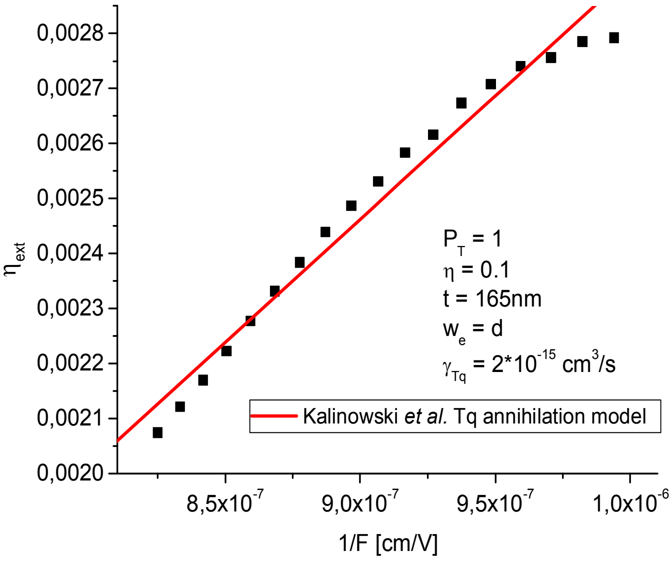

Figure 8.3.9. The external quantum efficiency as a function of 1/F. The red line is the best fit to the experimental data on the base of formula 8.3.9

Again a poor agreement between the model and the experimental data is visible. The obtained value of $\gamma_{Tq} = 2\cdot10^{-15}$ cm^3/s is two, three orders of magnitude lower than those calculated for other phosphorescent complexes [150, 151]. Concluding this part we can summarize that the triplet-polaron annihilation process is not adequate to describe the external quantum efficiency roll-off.

The last case we will analyse is a decrease of external quantum efficiency due to an electric field induced dissociation of (e-h) pairs formed during bimolecular recombination of injected carriers. For this purpose we calculate the probability of exciton formation R in the presence of dissociation process dependent on external electric field $\Omega(F)$, described by formula 4.29 in chapter 4.13,

$$R = 1 - \Omega(F). \tag{8.3.10}$$

We assume here that the most significant influence of the field is on the separation process of a charge pair. The obtained curves were normalized to the maximum of the external quantum efficiency. The results of calculations for different ratios of r_0/r_c (the distance between coulombically correlated charge pair divided by Onsager radius) are presented in figure 8.3.10 together with the measured external quantum efficiency η_{ext}.

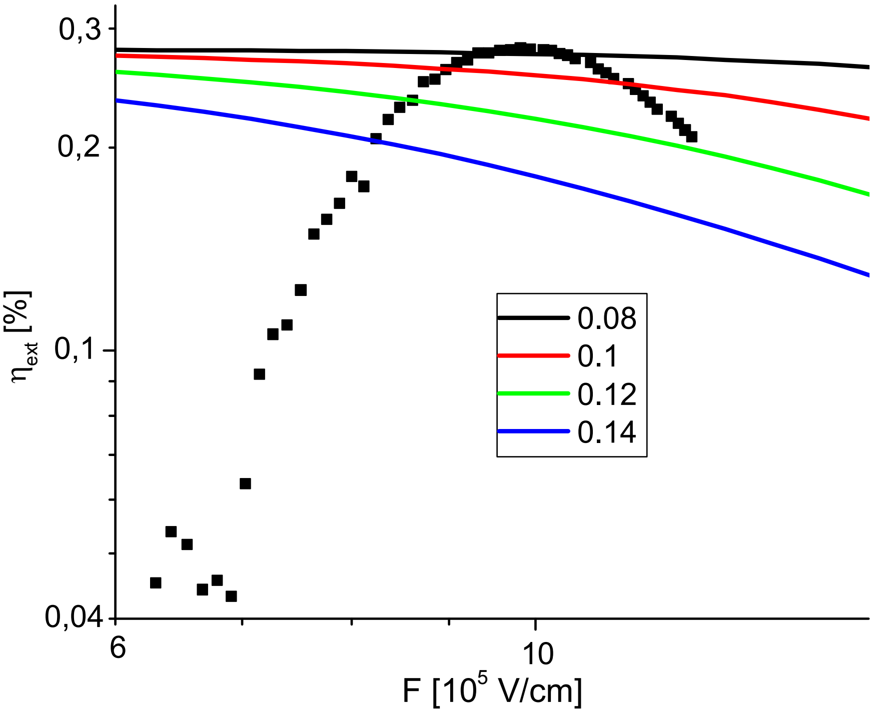

Figure 8.3.10. The external quantum efficiency (points) as a function of external electric field. The theoretical curves (solid lines) were calculated according to the Onsager model for various values of r_0/r_c as indicated in the figure

As can be seen in the figure, the decrease of the external quantum efficiency does not follow the theoretical curves, therefore, the field assisted charge pair dissociation is rather not the main reason for lowering of the η_{ext}.

Another property of the external quantum efficiency shown in figure 8.3.10 is its well pronounced initial growth with applied external electric field. This behaviour can be explained by the injection controlled EL (ICEL) of the device which takes place when the transition time of charge carriers through the recombination zone, τ_t,is shorter than the recombination time of charge carriers of the opposite signs, τ_{rec} [41]. As a consequence, the probability of charge carrier passage through the recombination zone without recombination is higher than that of recombination within it (see formula 5.1). Therefore, EL is here only a side effect of current flow and η_{ext} is proportional to the product of the hole and electron injection currents. With increasing density of current the probability that the charges of opposite signs meet within the recombination zone becomes higher and at the same time the probability of charge carrier passage through the device diminishes. At some point τ_t becomes higher than τ_{rec} and the device achieves the volume controlled EL (VCEL) regime. The evidence proving the transition from the ICEL to VCEL mechanism and associated with that transition change in device efficiency can be found by comparing the current density in figure 8.3.8a and η_{ext} in figure 8.3.10. We notice that for the current density in the low-field range the external quantum efficiency grows while for l=10.5 the η_{ext} reaches its maximum. The non-perfect agreement between the electric field value at which the current density switches from ICEL to VCEL mode ($F \approx 7.5*10^5$ V/cm) and the position of the η_{ext} maximum ($F \approx 10^6$ V/cm) is due to the fact that in this simple analysis we neglect other effects influencing external quantum efficiency. Those are the change in hole and electron current densities with increasing applied field and resulting change in the recombination zone thickness.

Among all devices the best performance in terms of parameters presented in table 8.3.2 was shown by the diode with FPtCl complex as an emitter. It has the lowest turn-on voltage (despite similar thickness of the diodes) and a four times higher luminance (also the maximal one) from the presented OLEDs. It is worth to note that though the efficiencies obtained here are lower than those of diodes with similar complex but built by thermal evaporation [152], they are still one order of magnitude higher than those of OLEDs built by the spin-coating technique and based on the substituted 4,4'-stilbenoid N^C^N platinum(II) [153].

In the last row of table 8.3.2 the chromaticity coordinates of the three spectra from figure 8.3.5 are presented. The purest green colour is obtained for the OLED with FPtCl (compare the values of *y* coordinate). The worse colour purity of two other emitters is due to the presence of the spectral component centred around 600 nm which now we will discuss in more detail.

In figure 8.3.11 the spectra of two double-layer diodes are presented as recorded for the fresh devices and devices after some operation time. The presence of a long-wave component of the spectra is observed, denoted by red lines in the figure. This component we associate not with the platinum complexes, but rather with the PVK luminescence. A proof for this is shown in figure 8.3.12, where the EL spectra of a diode containing solely PVK as an emitting layer recorded at different operating voltages are presented. Here, with increasing voltage the intensity of the band centred around 600 nm becomes higher. This emission was assigned by different authors to polymer phosphorescence [41], triplet excimers [117] and electromers [127, 154] of PVK.

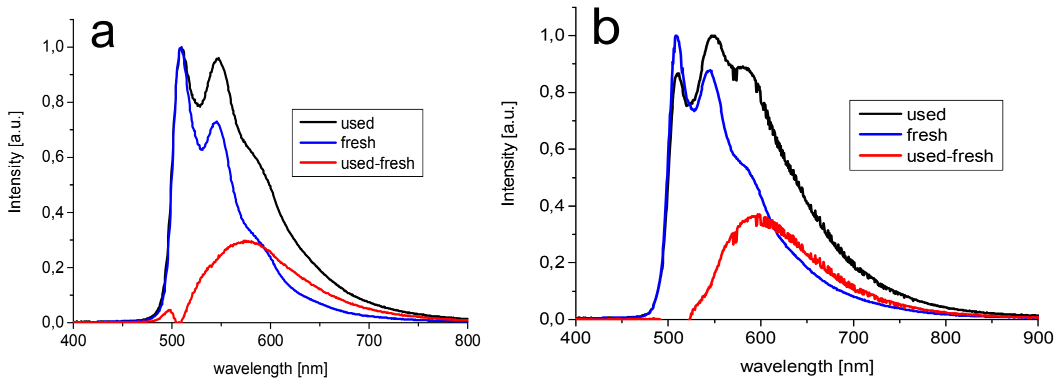

Figure 8.3.11. EL spectra of fresh and used up double layer devices with FPtCl (a) and MePtCl (b) as emitters. The red spectra were obtained by subtraction from the spectrum of the used up device the spectrum of the fresh one

We can also give a qualitative explanation of different influence of the PVK red emitting state on the EL spectra of the OLEDs with three platinum complexes. In figure 8.3.5 we notice that the strongest change in the spectrum is observed for the diode with MePtNCS, the moderate one is recorded for the device with MePtCl, while the spectrum of the OLED with FPtCl is the least affected. The same order is also perceived in the energies of the HOMO levels of the complexes with that of MePtNCS being the shallowest and with the level of FPtCl being the deepest (figure 8.3.5). We can suspect that those two features are somehow related to each other, because the LUMO levels of the complexes as well as other properties of discussed devices are similar. Therefore, an explanation of the observed behaviour may be as follows.

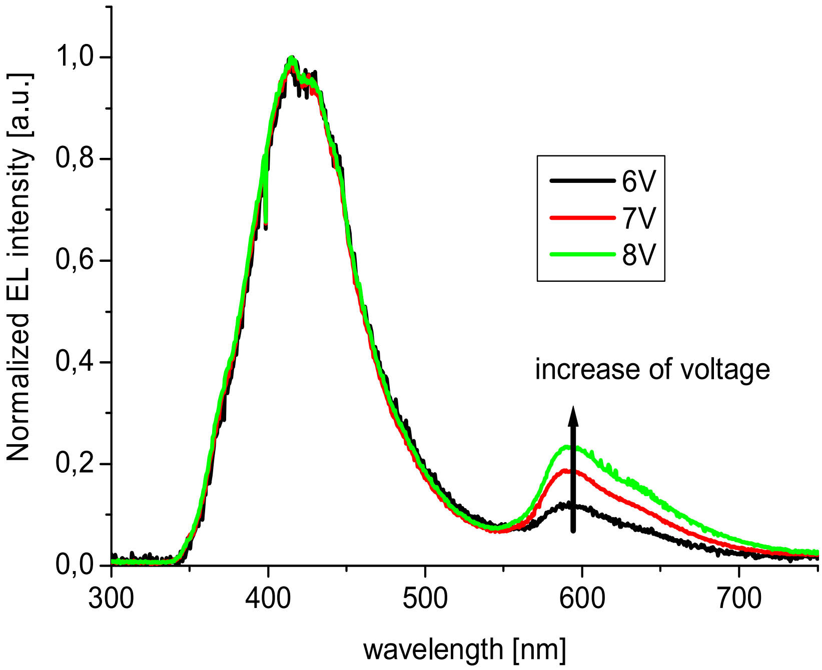

Figure 8.3.12. EL spectra of a single layer OLED with neat PVK as emitting layer

After injection from the cathode electrons travel easily towards the centre of a diode due to high concentration (of 30%) of an electron transporting material (PBD) and LUMO energy levels of the phosphorescent molecules being comparable to those of PBD, which prevents creation of electron traps. From the other side the holes move in PVK-h layer (HTL) and arrive at the interface with the emitting layer (EML). In the case of the diode with FPtCl the holes get easily into the emissive layer because the HOMO level of the complex does not create any traps for this kind of charge carriers. Therefore, the excitons are formed predominantly within a bulk of the emitting layer and the observed emission is either due to energy transfer from the matrix to the dopant or direct trapping in emitting centres. In the case of complexes with shallower HOMO levels the situation is, however, different since the holes are trapped close to the HTL/ETL interface which implies various consequences. The highly concentrated holes attract electrons to the interface zone and excitons predominantly there will be formed. They can diffuse in both directions, however, their movement towards the cathode is somehow impeded due to the presence of traps. We note here that even if the platinum complexes had high hole mobilities in solid state it could not help in their transport because of too low concentration of the dopants [155]. Therefore, excitons may enter from the interface zone into the HTL layer and recombine there. Nonetheless, the blue emission of PVK-h is not observed because the high LUMO level of PVK-h does not allow creation of singlet excitons in HTL. However, even if PVK-h singlet excited states were created, the long range energy transfer to the platinum complex would hinder the blue emission of PVK-h. Only possible emission from the HTL layer is therefore from the PVK-h triplet excimers. Since this is a parasitic red emission of low quantum yield it should limit the efficiency of the green Pt complex component of a diode spectrum. Consequently, the trend observed in the external quantum efficiencies (table 8.3.2) is consistent with the energy positions of the HOMO levels in those three Pt complexes.

Because FPtCl complex revealed the best performance as an emitter, it was decided to employ this one in a WOLED. However, first it was necessary to check its ability to emit red light from excimers under electrical excitation. Such a possibility was suggested by results of PL measurements carried out on the solutions at different concentrations and by results obtained by other authors on similar complexes [59]. To test this hypothesis single layer OLEDs were built, containing different concentrations of FPtCl in PVK:PBD matrix, their spectra and corresponding chromaticity coordinates are presented in figure 8.3.13. By changing the dopant concentration from 10% to 50% it was possible to tune the emission colour from green to red. For a diode containing 40% FPtCl the balanced green and red emission was observed and the same composition was employed for the construction of a double layer WOLED, as described below.

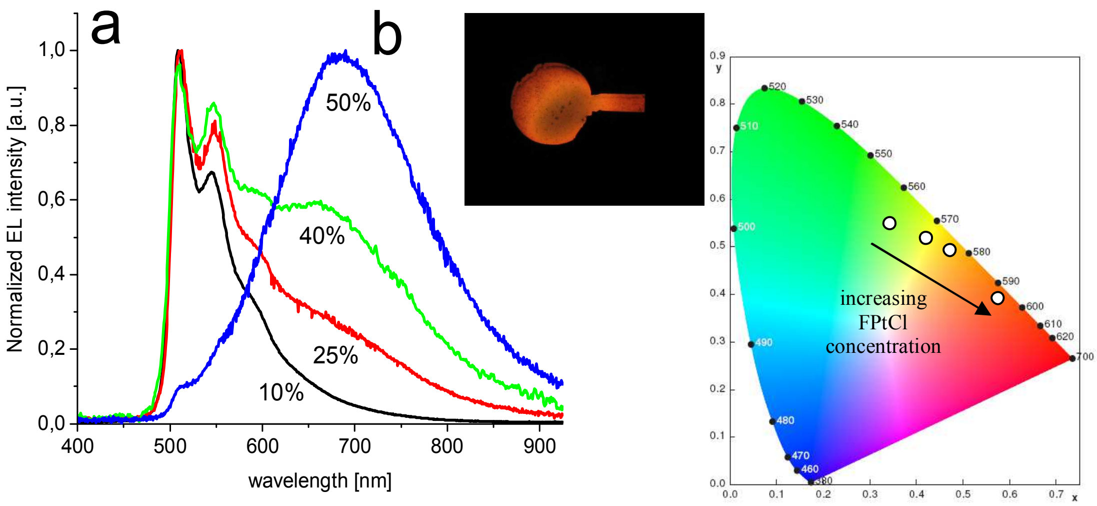

Figure 8.3.13. (a) EL spectra of single layer OLEDs with different concentrations of FPtCl dispersed in PVK:PBD matrix; (b) a photograph of emitting device containing 50% FPtCl. The chromaticity coordinates of the spectra from (a) are also indicated

In the following we present results obtained for a double layer WOLED prepared by spin-coating technique. Initially, the WOLEDs with bottom layers containing either PVK-h or PVK-h:PBD were tested but no blue emission was observed. Therefore, it was decided to introduce polyfluorene (PFO) as an efficient blue emitter [156]. The final device had the following structure, ITO/ PEDOT:PSS / 52% PVK-h : 48% PFO / 40% PVK : 20% PBD : 40% FPtCl / Ca / Al. The energy levels of the employed compounds are presented in figure 8.3.14.

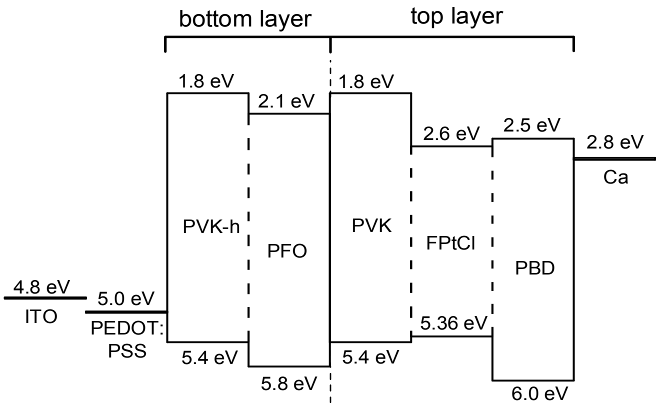

Figure 8.3.14. HOMO and LUMO levels of materials used in the double layer WOLED

The bottom layer consists here of PVK-h and PFO mixture and serves as the blue-emitting and hole-transporting layer. PVK-h has the HOMO below the energy level of PEDOT:PSS which facilitates injection of holes to PFO while the latter material ensures the relatively high hole mobility [157]. The top layer consists of highly concentrated FPtCl dispersed in a PVK:PBD matrix. A rather good fit of the HOMO and LUMO levels of the complex and the compounds which form the matrix provides a decent charge transport.

The EL spectrum of the WOLED and its chromaticity coordinates are presented in figure 8.3.15. The shoulder around 415 nm most likely takes origin from the residual PFO α phase

[158, 159] and becomes almost eliminated after a thermal treatment of the bottom layer (for more details of the device building procedure see chapter 7.2). The sharp peaks at 438 nm and 465 nm correspond to vibronic 0 → 0 and 0 → 1 transitions of a newly formed, after thermal treatment, β phase of PFO.

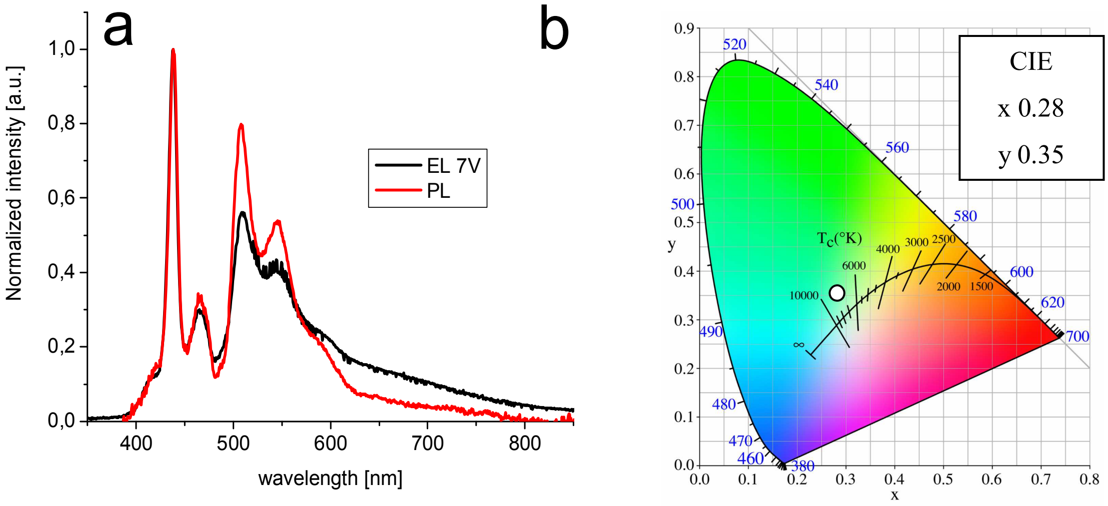

Figure 8.3.15. Comparison between the EL at 7V and PL (λ_{exc}= 325 nm) spectra of the WOLED (a); CIE coordinates of the EL spectrum (b)

Due to the high concentration of FPtCl complex a two-colour emission was observed from the top layer. The peaks located at 509 nm and 544 nm together with the shoulder at 590 nm originate from the emission of single FPtCl molecules while the tail seen for longer wavelengths results from the phosphorescence of the complex excimer. The lower intensity of the excimer band in the WOLED in comparison to the single layer OLED, both with 40% FPtCl concentration, is most likely caused by partial dissolution of the bottom layer during deposition of the second film, as confirmed by AFM thickness measurements (figure 8.3.16). In this process the FPtCl molecules penetrate the bottom layer increasing a dispersion of the complex at the interface which affects the balance between the accessible monomer and excimer states.

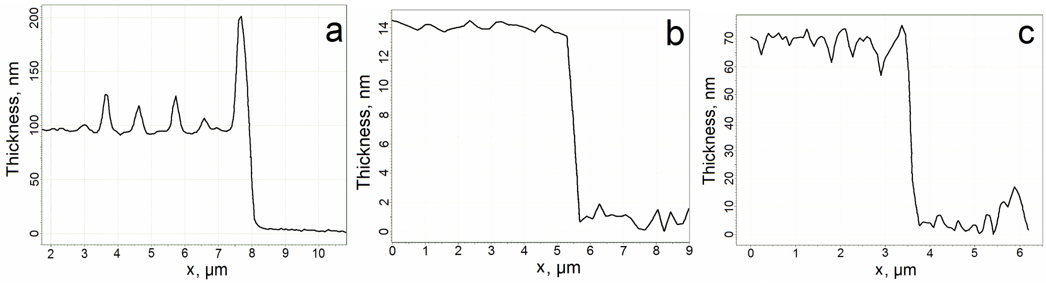

Figure 8.3.16. AFM thickness profiles of 52% PVK-h : 48% PFO film, (90±9) nm (a); 40% PVK : 20% PBD : 40% FPtCl film, (15±2) nm (b); 52% PVK-h : 48% PFO / 40% PVK : 20% PBD ; 40% FPtCl film, (63±6) nm (c)

In our diode the emitted blue light can leave the device directly or after reflection from the cathode. In the second case, however, the light being partially absorbed can excite the Pt(II) complex due to the overlap of the FPtCl absorption spectrum and the emission spectra of the compounds of the bottom layer (figure 8.3.17).

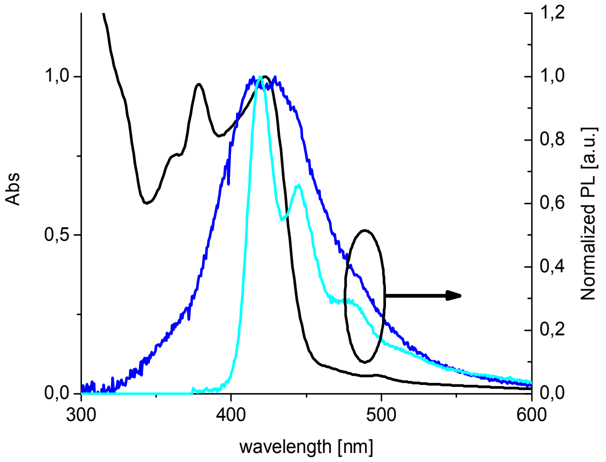

Figure 8.3.17. Normalized absorption spectrum of FPtCl in dichloromethane (black line) and PL spectra of films of PFO (cyan line) and PVK:PBD (blue line). Excitation wavelengths were 325 nm and 320 nm for PFO and PVK:PBD, respectively

The fluorescent blue emission of PFO from the bottom layer combined with the green and red phosphorescence (originating from monomers and excimers of the complex, respectively) generate white light, since the emission of the top layer is not absorbed by the polymers of the bottom one and, thus, exits the device freely. The Commission Internationale de l'Eclairage (CIE) coordinates of the EL spectrum are x = 0.28, y = 0.35 and the CCT is equal to 8145 K, whereas the CRI equals to 74 and the η_{ext} remains as high as about $4 \cdot 10^{-4}$ %. The low efficiency of the device is caused by rather high concentration of the dopant being a source of concentration quenching. Additionally, the excimer states are generally known as those of low emission efficiency in comparison to the monomers.

In figure 8.3.15a the photoluminescence spectrum of the WOLED is confronted with the electroluminescent one. The spectra, being normalized at the PFO maximum, reveal a difference in the green-red region with reversed intensities of the monomer and excimer emission. A probable explanation of this phenomenon originates from the different mechanisms responsible for exciton and excimer generation in these two types of luminescence. In PL the sample was excited through ITO/PEDOT:PSS layer, therefore the blue emission should be the most intense one. Additionally, it is expected that partial dissolution of the PVK-h:PFO bottom layer during spin-coating of the second layer allows penetration of the complex and increased dispersion of FPtCl molecules. As a consequence, in PL excitation the main emission is observed from the bottom layer containing PVK-h:PFO and the monomers of FPtCl. In the case of EL, excitation of emitting states is more uniform within the device because charge carriers must travel through the OLED in order to create emitting states. Therefore, somehow more balanced emission from blue and green emitting monomers, and red emitting excimers is observed, together creating white light.

9. SUMMARY AND CONCLUSIONS

This thesis deals with three different concepts of obtaining white light from the OLEDs. They are based on the fluorescence or phosphorescence of single molecules as well as mixed fluorescence or phosphorescence of single emitters and excimers.

The first approach of white colour creation comprises different generations of dendronic molecules with pyrene antennae acting as energy donors, and styrylpiridinium derivative molecule as energy acceptor. It is shown that in solution the blue emission of pyrene monomer, green emission of pyrene excimer and red emission of acceptor moiety can be achieved contemporarily from a single dendronic molecule founding the corner stone for a white light-emitting OLED with single dye. The proper mixture of dendronic and donor molecules placed in a bipolar matrix achieves the maximal external quantum efficiency of 0.05%, the CCT of 4260 K and the CIE chromaticity coordinates being (0.36, 0.34) which correspond closely to the equal energy white.

The second approach employs the tetrakis β-diketonate complexes of terbium and europium as green and red emitter, respectively. The complexes were characterized photophysicaly and were tested in single colour emitting devices. Then they were mixed and placed in a bipolar matrix creating the white light emitting OLEDs with blue-emission component from the matrix. The WOLED exhibits the maximal external quantum efficiency equal to 0.01%, the CIE chromaticity coordinates at 14 V of (0.33, 0.38), the CCT = 5460 K and CRI = 81 providing natural daylight with good colour reproduction.

In the thesis the kinetics of energy transfer from the materials creating the matrix of the WOLED to the europium complex is also described. The relevant model includes the exciton diffusion in the matrix as preceding the energy transfer to the acceptor. Based on this assumption the diffusion coefficients of singlet excitons in the matrix and their diffusion path lengths are determined.

The third approach involves an application of organic platinum complexes emitting from monomers and excimers. Photophysical properties of the complexes were measured and subsequently the emitters were tested in single and double-layer green-emitting OLEDs. For the most efficient device, mechanisms responsible for the decrease in external quantum efficiency are discussed and the experimental results are compared with theoretical models (the triplet-triplet annihilation, triplet-polaron annihilation, dissociation of charge pairs caused by external electric field). On this basis the annihilation bimolecular kinetic constant is determined for the triplet-triplet annihilation process which was identified as the main reason for the external quantum efficiency reduction with current density increase. Finally, a double-layer white light-emitting diode was built and characterized, employing emissions of monomer and excimer of the platinum complex from the top layer and blue emission from the bottom one. The EL spectrum possesses the CIE coordinates, $x = 0.28$, $y = 0.35$ and the CCT equal to 8145 K, the CRI equal to 74 and $\eta_{ext} \approx 4\cdot10^{-4}\%$.

In appendix A the calculation of colour rendering index is explained while in appendix B the formulae for the parameters describing performance of a device are derived.

It is highly probable that large-area sources of light manufactured from solutions and deposited on flexible substrates will determine the future of the illumination industry. Indeed, industrial application of such a technology would take a full advantage of many beneficial properties of organic materials which, together with its low production costs, should boost a rapid development of the branch. Nevertheless, any improvement of contemporary WOLEDs requires the possession of more suitable materials as well as profound understanding of phenomena occurring in these devices. The present thesis shall contribute to these goals by investigating the excitonic effects in electroluminescent WOLEDs based on three types of new emitters prepared by spin-coating technique. In the author's opinion the obtained results should bring the organic LEDs closer to the brilliant future they deserve so much.

10. ACKNOWLEDGEMENTS

Firstly, I address my thanks to my advisor, dr hab. inż. Waldemar Stampor, prof. nadzw. PG. Starting from that it was his idea how to forge this thesis from my research work, through a process of writing and till the revision of the manuscript, his help, the comprehensive knowledge about physics and permanent accessibility were essential for finishing this thesis.

I would like also to thank professor Jan Kalinowski for giving me an opportunity to visit research facilities in Italy, without which the experimental results included in this thesis would not have been obtained.

I appreciate the hospitality of professor Riccardo Tubino and professor Francesco Meinardi, heads of the group at the Università degli Studi di Milano-Bicocca where I walked the first steps as an independent experimental physicist. I am also grateful to dr inż. Jakub Mężyk for a guidance at the beginning of my work and to dr Agnieszka Mech for providing lanthanide complexes used in this thesis. I thank Jakub and Agnieszka for our conversations in polish during my stay abroad.

Then my gratitude goes to my co-advisor, Ph.D. Chiara Botta, and to Umberto Giovanella from Istituto per lo Studio delle Macromolecole (ISMAC) for teaching me about photophysics of organic materials and about organic light-emitting diodes. I appreciate also working with dr inż. Dariusz Kotowski and the possibility of using my mother language also in ISMAC. Due to the same reason I am grateful to dr Marta Mróz.

Special thanks deserves Marina Babushkina for supporting my pursuit to achieve the Ph.D. Hearing about her progress in writing her thesis was stimulating to continue my enterprise. I am grateful also for providing polymer TPD used in this work and many conversations.

Ester Rossi is appreciated for synthesis of platinum complexes employed in devices described in this thesis.

The participation of dr inż. Piotr Grygiel in the revision of the thesis is kindly recognized.

I want to thank all co-authors of our publications for the joint development of the manuscripts.

Finally, I want to show my gratitude to my parents who always encouraged me to study and showed me that with hard work it is possible to achieve goals we dream about.

11. APPENDIX A

Now we present in detail how to calculate the colour rendering index using as an example the spectrum presented below. The relevant data of the spectrum can be found at the end of the appendix.

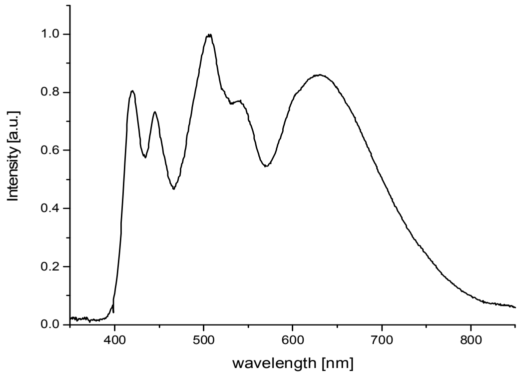

Figure A1. The spectrum used for CRI calculation

We start with determination of the *CIE* coordinates, x_s and y_s, of the spectrum, the procedure has already been described in chapter 6. For the above spectrum we obtain x_s=0.3438, y_s=0.3520. Now we transform the result into the *CIE* 1960 chromaticity coordinates (formulae 6.3, chapter 6), getting u_s=0.2104 and v_s=0.3231. Then we calculate the *CCT* of the spectrum. Using [65] we obtain 5053K, while applying [66] gives 5059K. We will take an average of both and so we set CCT_s=5056K. From Planck's law we generate the black body spectrum having the same temperature as our source and we find its chromaticity coordinates u_P and v_P. We obtain u_P=0.2114, v_p=0.3230 and from formula 6.4 the *DC* is equal to $1 \cdot 10^{-3}$, fulfilling condition $< 5.4 \cdot 10^{-3}$ which is required for an accurate CRI result. Now we have to determine the reference spectrum. In the case that temperature of our source is below 5000K as a reference illuminant a black body radiator having temperature of the tested source serves. If CCT is equal to or higher than 5000K (as in our case) a reference spectrum *S(λ)* will be the one of the standard illuminant D, consisting of the linear combination of three spectra [69, 70]

$$S(\lambda) = S_0(\lambda) + M_1 S_1(\lambda) + M_2 S_2(\lambda)\,,$$

where

$$M_1 = \frac{-1.3515 - 1.7703 x_D + 5.9114 y_D}{M}, M_2 = \frac{0.03 - 31.4424 x_D + 30.0717 y_D}{M},$$

$$M = 0.0241 + 0.2562 x_D - 0.7341 y_D\,,\ \ y_D = -3x_D^2 + 2.87 x_D - 0.275$$

and

$$x_D = 0.244063 + 0.09911\frac{10^3}{T} + 2.9678\frac{10^6}{T^2} - 4.607\frac{10^9}{T^3} \quad \text{for } 4{,}000\text{K} \le T \le 7{,}000\text{K}$$

or

$$x_D = 0.23704 + 0.24748\frac{10^3}{T} + 1.9018\frac{10^6}{T^2} - 2.0064\frac{10^9}{T^3} \quad \text{for } 7{,}000\text{K} \le T \le 25{,}000\text{K}.$$

For T = 5056 K we get:
$x_D = 0.3441$, $y_D = 0.3574$,
$M = -0.1501$, $M_1 = -1.0118$, $M_2 = 0.2882$.

The day light components data $S_0(\lambda)$, $S_1(\lambda)$ and $S_2(\lambda)$ are listed in table A3 at the end of the appendix and are displayed in figure A2 together with the reference illuminant spectrum $S(\lambda)$.

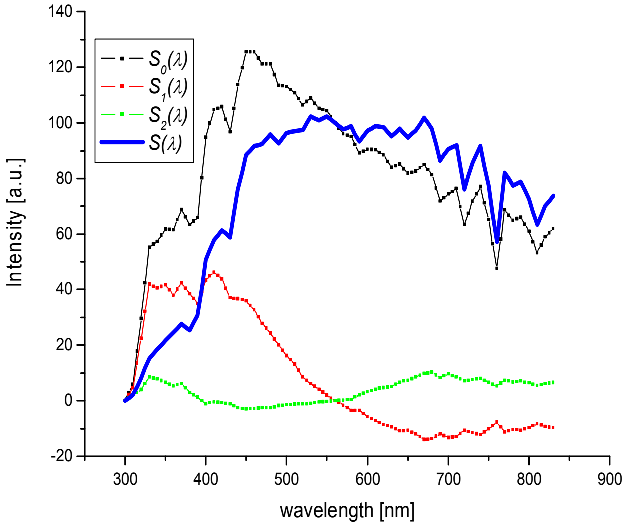

Figure A2. The reference illuminant spectrum $S(\lambda)$, having temperature 5056K, and its components $S_0(\lambda)$, $S_1(\lambda)$ and $S_2(\lambda)$

Having determined the reference illuminant spectrum we have to calculate its coordinates in the *CIE 1960* chromaticity diagram and we obtain u_r=0.2086 and v_r=0.3249. It is also necessary to calculate the Y tristimulus value of the tested and the reference source. We get Y_s = 15.5706 and Y_r = 2100.2549 from formula 6.1 in chapter 6 (the latter value depends on units we choose for the reference spectrum). Now we are ready to simulate illumination of eight test colour samples (TCSs) by the reference source and by the one of which the CRI we are searching. Tabulated TCSs reflectance spectra can be found at the end of the appendix (table A2).

First we multiply the tested spectrum from figure A1 by TCS1 reflectance spectrum and calculate chromaticity coordinates u_{s1}, v_{s1}, and also the $\tilde{Y}_{s1}$ tristimulus value. We get u_{s1}=0.2584, v_{s1}=0.3316, $\tilde{Y}_{s1}$ = 4.7462. In calculations it is required to normalize the Y_s (Y_r) value to 100 and properly all subsequent Y_{si} (Y_{ri}) (i=1,..,8 for each TCS). We apply formula

$$Y_{si} = \frac{100\widetilde{Y}_{si}}{Y_s},$$

obtaining for the first TCS Y_{s1}=30.4819. Now similarly we repeat the procedure for the reference spectrum. The values we obtained are u_{r1}=0.2524, v_{r1}=0.3336 and Y_{r1}=30.3879.

Subsequently, we apply von Kries chromatic transformation according to the following formulas [69, 70]

$$u'_{si} = \frac{10.872 + 0.404\frac{c_r c_{si}}{c_s} - 4\frac{d_r d_{si}}{d_s}}{16.518 + 1.481\frac{c_r c_{si}}{c_s} - \frac{d_r d_{si}}{d_s}}, \quad v'_{si} = \frac{5.52}{16.518 + 1.481\frac{c_r c_{si}}{c_s} - \frac{d_r d_{si}}{d_s}}, \; i=1,..,8,$$

where

$$c_r = \frac{4 - u_r - 10v_r}{v_r}, \qquad d_r = \frac{1.708v_r + 0.404 - 1.481u_r}{v_r},$$

$$c_s = \frac{4 - u_s - 10v_s}{v_s}, \qquad d_s = \frac{1.708v_s + 0.404 - 1.481u_s}{v_s},$$

$$c_{si} = \frac{4 - u_{si} - 10v_{si}}{v_{si}}, \qquad d_{si} = \frac{1.708v_{si} + 0.404 - 1.481u_{si}}{v_{si}}, \; i=1,..,8.$$

Now it is necessary to perform calculations in the *CIE 1964* colour space. To do this we use formulas

$$W^*_{ri} = 25\sqrt[3]{Y_{ri}} - 17, \qquad W^*_{si} = 25\sqrt[3]{Y_{si}} - 17,$$

$$U^*_{ri} = 13W^*_{ri}(u_{ri} - u_r), \qquad U^*_{si} = 13W^*_{si}(u'_{si} - u_r),$$

$$V^*_{ri} = 13W^*_{ri}(v_{ri} - v_r), \qquad V^*_{si} = 13W^*_{si}(v'_{si} - v_r), \; i=1,..,8.$$

From the obtained values we are able to calculate the colour difference between the chromatically adapted samples and those illuminated by the reference source. We apply formula

$$\Delta E_i = \sqrt{(W^*_{ri} - W^*_{si})^2 + (U^*_{ri} - U^*_{si})^2 + (V^*_{ri} - V^*_{si})^2}, \; i=1,..,8.$$

Finally, we find the special CRI from formula

$$R_i = 100 - 4.6\Delta E_i, \; i=1,..,8.$$

Now we repeat the procedure for TCS2, TCS3,...,TCS8. Having eight special R_i we take an average of them to determine the general colour rendering index

$$R_a = \frac{1}{8}\sum_{i=1}^{8} R_i \, .$$

For our spectrum we obtain R_a = 87, which is a very good result for illumination light sources. In the table below the chromaticity coordinates, the Y tristimulus values and the special CRIs obtained for eight TCSs illuminated by the tested and the reference source are gathered.

Table A1. Chromaticity parameters for the spectrum from figure A1

		TCS1	**TCS2**	**TCS3**	**TCS4**	**TCS5**	**TCS6**	**TCS7**	**TCS8**
Tested	*u*	0.2584	0.2335	0.1982	0.1595	0.1689	0.1808	0.2262	0.2553
	v	0.3316	0.3479	0.3605	0.3439	0.3168	0.2922	0.2941	0.3061
	Y	30.4819	29.0887	29.9432	29.1203	30.4270	29.6977	29.7731	32.4265
Reference	*u*	0.2524	0.2297	0.1972	0.1631	0.1712	0.1815	0.2226	0.2493
	v	0.3336	0.3494	0.3619	0.3440	0.3175	0.2929	0.2964	0.3082
	Y	30.3879	29.2807	30.5593	29.0160	30.2700	29.1560	29.3777	31.7862
R_i		83.03	92.04	95.38	78.24	82.50	87.04	92.48	81.44

Table A2. The test spectrum as a function of wavelength together with reflectance spectra of TCS*i* (*i* =1,..., 8)

wavelength	**Test spectrum**	**TCS1**	**TCS2**	**TCS3**	**TCS4**	**TCS5**	**TCS6**	**TCS7**	**TCS8**
[nm]	**[a.u.]**								
380	0,01681	0,219	0,07	0,065	0,074	0,295	0,151	0,378	0,104
385	0,01797	0,239	0,079	0,068	0,083	0,306	0,203	0,459	0,129
390	0,02036	0,252	0,089	0,07	0,093	0,31	0,265	0,524	0,17
395	0,04673	0,256	0,101	0,072	0,105	0,312	0,339	0,546	0,24
400	0,10803	0,256	0,111	0,073	0,116	0,313	0,41	0,551	0,319
405	0,23612	0,254	0,116	0,073	0,121	0,315	0,464	0,555	0,416
410	0,48702	0,252	0,118	0,074	0,124	0,319	0,492	0,559	0,462

415	0,7194	0,248	0,12	0,074	0,126	0,322	0,508	0,56	0,482
420	0,80509	0,244	0,121	0,074	0,128	0,326	0,517	0,561	0,49
425	0,72242	0,24	0,122	0,073	0,131	0,33	0,524	0,558	0,488
430	0,61048	0,237	0,122	0,073	0,135	0,334	0,531	0,556	0,482
435	0,57933	0,232	0,122	0,073	0,139	0,339	0,538	0,551	0,473
440	0,66339	0,23	0,123	0,073	0,144	0,346	0,544	0,544	0,462
445	0,73019	0,226	0,124	0,073	0,151	0,352	0,551	0,535	0,45
450	0,67157	0,225	0,127	0,074	0,161	0,36	0,556	0,522	0,439
455	0,58386	0,222	0,128	0,075	0,172	0,369	0,556	0,506	0,426
460	0,5136	0,22	0,131	0,077	0,186	0,381	0,554	0,488	0,413
465	0,47569	0,218	0,134	0,08	0,205	0,394	0,549	0,469	0,397
470	0,48879	0,216	0,138	0,085	0,229	0,403	0,541	0,448	0,382
475	0,54281	0,214	0,143	0,094	0,254	0,41	0,531	0,429	0,366
480	0,6234	0,214	0,15	0,109	0,281	0,415	0,519	0,408	0,352
485	0,70899	0,214	0,159	0,126	0,308	0,418	0,504	0,385	0,337
490	0,78994	0,216	0,174	0,148	0,332	0,419	0,488	0,363	0,325
495	0,87782	0,218	0,19	0,172	0,352	0,417	0,469	0,341	0,31
500	0,95456	0,223	0,207	0,198	0,37	0,413	0,45	0,324	0,299
505	0,99054	0,225	0,225	0,221	0,383	0,409	0,431	0,311	0,289
510	0,96989	0,226	0,242	0,241	0,39	0,403	0,414	0,301	0,283
515	0,89754	0,226	0,253	0,26	0,394	0,396	0,395	0,291	0,276
520	0,81132	0,225	0,26	0,278	0,395	0,389	0,377	0,283	0,27
525	0,78647	0,225	0,264	0,302	0,392	0,381	0,358	0,273	0,262
530	0,76077	0,227	0,267	0,339	0,385	0,372	0,341	0,265	0,256
535	0,76572	0,23	0,269	0,37	0,377	0,363	0,325	0,26	0,251
540	0,7691	0,236	0,272	0,392	0,367	0,353	0,309	0,257	0,25

545	0,75128	0,245	0,276	0,399	0,354	0,342	0,293	0,257	0,251
550	0,71723	0,253	0,282	0,4	0,341	0,331	0,279	0,259	0,254
555	0,66707	0,262	0,289	0,393	0,327	0,32	0,265	0,26	0,258
560	0,6005	0,272	0,299	0,38	0,312	0,308	0,253	0,26	0,264
565	0,56266	0,283	0,309	0,365	0,296	0,296	0,241	0,258	0,269
570	0,54706	0,298	0,322	0,349	0,28	0,284	0,234	0,256	0,272
575	0,55498	0,318	0,329	0,332	0,263	0,271	0,227	0,254	0,274
580	0,58909	0,341	0,335	0,315	0,247	0,26	0,225	0,254	0,278
585	0,6338	0,367	0,339	0,299	0,229	0,247	0,222	0,259	0,284
590	0,68315	0,39	0,341	0,285	0,214	0,232	0,221	0,27	0,295
595	0,73536	0,409	0,341	0,272	0,198	0,22	0,22	0,284	0,316
600	0,77575	0,424	0,342	0,264	0,185	0,21	0,22	0,302	0,348
605	0,79802	0,435	0,342	0,257	0,175	0,2	0,22	0,324	0,384
610	0,81575	0,442	0,342	0,252	0,169	0,194	0,22	0,344	0,434
615	0,83471	0,448	0,341	0,247	0,164	0,189	0,22	0,362	0,482
620	0,85036	0,45	0,341	0,241	0,16	0,185	0,223	0,377	0,528
625	0,85442	0,451	0,339	0,235	0,156	0,183	0,227	0,389	0,568
630	0,86001	0,451	0,339	0,229	0,154	0,18	0,233	0,4	0,604
635	0,85655	0,451	0,338	0,224	0,152	0,177	0,239	0,41	0,629
640	0,84671	0,451	0,338	0,22	0,151	0,176	0,244	0,42	0,648
645	0,83458	0,451	0,337	0,217	0,149	0,175	0,251	0,429	0,663
650	0,81239	0,45	0,336	0,216	0,148	0,175	0,258	0,438	0,676
655	0,78822	0,45	0,335	0,216	0,148	0,175	0,263	0,445	0,685
660	0,76195	0,451	0,334	0,219	0,148	0,175	0,268	0,452	0,693
665	0,74125	0,451	0,332	0,224	0,149	0,177	0,273	0,457	0,7
670	0,71286	0,453	0,332	0,23	0,151	0,18	0,278	0,462	0,705

675	0,67306	0,454	0,331	0,238	0,154	0,183	0,281	0,466	0,709
680	0,63951	0,455	0,331	0,251	0,158	0,186	0,283	0,468	0,712
685	0,60736	0,457	0,33	0,269	0,162	0,189	0,286	0,47	0,715
690	0,5725	0,458	0,329	0,288	0,165	0,192	0,291	0,473	0,717
695	0,53703	0,46	0,328	0,312	0,168	0,195	0,296	0,477	0,719
700	0,50459	0,462	0,328	0,34	0,17	0,199	0,302	0,483	0,721
705	0,46978	0,463	0,327	0,366	0,171	0,2	0,313	0,489	0,72
710	0,43774	0,464	0,326	0,39	0,17	0,199	0,325	0,496	0,719
715	0,40804	0,465	0,325	0,412	0,168	0,198	0,338	0,503	0,722
720	0,38278	0,466	0,324	0,431	0,166	0,196	0,351	0,511	0,725
725	0,35521	0,466	0,324	0,447	0,164	0,195	0,364	0,518	0,727
730	0,32801	0,466	0,324	0,46	0,164	0,195	0,376	0,525	0,729
735	0,30236	0,466	0,323	0,472	0,165	0,196	0,389	0,532	0,73
740	0,28065	0,467	0,322	0,481	0,168	0,197	0,401	0,539	0,73
745	0,26315	0,467	0,321	0,488	0,172	0,2	0,413	0,546	0,73
750	0,24352	0,467	0,32	0,493	0,177	0,203	0,425	0,553	0,73
755	0,22194	0,467	0,318	0,497	0,181	0,205	0,436	0,559	0,73
760	0,20352	0,467	0,316	0,5	0,185	0,208	0,447	0,565	0,73
765	0,18339	0,467	0,315	0,502	0,189	0,212	0,458	0,57	0,73
770	0,16599	0,467	0,315	0,502	0,192	0,215	0,469	0,575	0,73
775	0,15343	0,467	0,314	0,51	0,194	0,217	0,477	0,578	0,73
780	0,14084	0,467	0,314	0,516	0,197	0,219	0,485	0,581	0,73

Table A3. The day light components' spectra $S_0(\lambda)$, $S_1(\lambda)$ and $S_2(\lambda)$

λ [nm]	**$S_0(\lambda)$**	**$S_1(\lambda)$**	**$S_2(\lambda)$**
300	0,04	0,02	0,00
305	3,02	2,26	1,00
310	6,00	4,50	2,00
315	17,80	13,45	3,00
320	29,60	22,40	4,00
325	42,45	32,20	6,25
330	55,30	42,00	8,50
335	56,30	41,30	8,15
340	57,30	40,60	7,80
345	59,55	41,10	7,25
350	61,80	41,60	6,70
355	61,65	39,80	6,00
360	61,50	38,00	5,30
365	65,15	40,20	5,70
370	68,80	42,40	6,10
375	66,10	40,45	4,55
380	63,40	38,50	3,00
385	64,60	36,75	2,10
390	65,80	35,00	1,20
395	80,30	39,20	0,05
400	94,80	43,40	-1,10
405	99,80	44,85	-0,80
410	104,80	46,30	-0,50
415	105,35	45,10	-0,60

420	105,90	43,90	-0,70
425	101,35	40,50	-0,95
430	96,80	37,10	-1,20
435	105,35	36,90	-1,90
440	113,90	36,70	-2,60
445	119,75	36,30	-2,75
450	125,60	35,90	-2,90
455	125,55	34,25	-2,85
460	125,50	32,60	-2,80
465	123,40	30,25	-2,70
470	121,30	27,90	-2,60
475	121,30	26,10	-2,60
480	121,30	24,30	-2,60
485	117,40	22,20	-2,20
490	113,50	20,10	-1,80
495	113,30	18,15	-1,65
500	113,10	16,20	-1,50
505	111,95	14,70	-1,40
510	110,80	13,20	-1,30
515	108,65	10,90	-1,25
520	106,50	8,60	-1,20
525	107,65	7,35	-1,10
530	108,80	6,10	-1,00
535	107,05	5,15	-0,75
540	105,30	4,20	-0,50
545	104,85	3,05	-0,40

550	104,40	1,90	-0,30
555	102,20	0,95	-0,15
560	100,00	0,00	0,00
565	98,00	-0,80	0,10
570	96,00	-1,60	0,20
575	95,55	-2,55	0,35
580	95,10	-3,50	0,50
585	92,10	-3,50	1,30
590	89,10	-3,50	2,10
595	89,80	-4,65	2,65
600	90,50	-5,80	3,20
605	90,40	-6,50	3,65
610	90,30	-7,20	4,10
615	89,35	-7,90	4,40
620	88,40	-8,60	4,70
625	86,20	-9,05	4,90
630	84,00	-9,50	5,10
635	84,55	-10,20	5,90
640	85,10	-10,90	6,70
645	83,50	-10,80	7,00
650	81,90	-10,70	7,30
655	82,25	-11,35	7,95
660	82,60	-12,00	8,60
665	83,75	-13,00	9,20
670	84,90	-14,00	9,80
675	83,10	-13,80	10,00

680	81,30	-13,60	10,20
685	76,60	-12,80	9,25
690	71,90	-12,00	8,30
695	73,10	-12,65	8,95
700	74,30	-13,30	9,60
705	75,35	-13,10	9,05
710	76,40	-12,90	8,50
715	69,85	-11,75	7,75
720	63,30	-10,60	7,00
725	67,50	-11,10	7,30
730	71,70	-11,60	7,60
735	74,35	-11,90	7,80
740	77,00	-12,20	8,00
745	71,10	-11,20	7,35
750	65,20	-10,20	6,70
755	56,45	-9,00	5,95
760	47,70	-7,80	5,20
765	58,15	-9,50	6,30
770	68,60	-11,20	7,40
775	66,80	-10,80	7,10
780	65,00	-10,40	6,80
785	65,50	-10,50	6,90
790	66,00	-10,60	7,00
795	63,50	-10,15	6,70
800	61,00	-9,70	6,40
805	57,15	-9,00	5,95

810	53,30	-8,30	5,50
815	56,10	-8,80	5,80
820	58,90	-9,30	6,10
825	60,40	-9,55	6,30
830	61,90	-9,80	6,50

12. APPENDIX B

In this chapter we derive basic formulae for the parameters describing performance quality of OLEDs. First we give some general remarks about radiation emission. In figure B1 a source of light is presented having the area *S* and emitting into the solid angle determined by the detection area *A* at the distance *r*. We assume here that S<<A. In general, intensity of radiation depends on angles *θ* and *φ*, however, we assume that the intensity is axially symmetric, *i.e.* does not depend on the azimuthal coordinate *φ*.

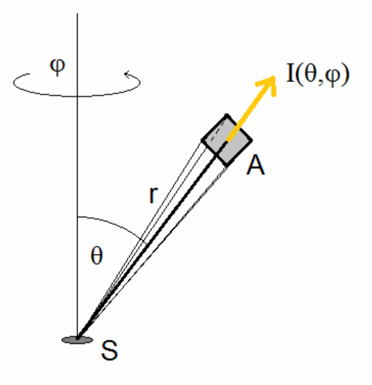

Figure B1. Geometrical parameters used to describe radiation of a flat light source

Moreover, OLEDs belong to a group of Lambert-type sources which means their EL intensity depends on the cosine of angle *θ*. Therefore, we can write formula for the intensity as

$$I(\theta,\varphi) = I_0 \cos\theta \,.$$

Subsequently, we calculate the radiant flux Φ of a source. Since a device emits in a forward direction we will integrate the intensity over the whole half-sphere

$$\Phi[W] = \int_0^{2\pi}\int_0^{\frac{\pi}{2}} I(\theta,\varphi)\sin\theta d\theta d\varphi = \int_0^{2\pi}\int_0^{\frac{\pi}{2}} I_0 \sin\theta\cos\theta d\theta d\varphi = \pi I_0\left[sr\cdot\frac{W}{sr}\right].$$

Now we can calculate the external quantum efficiency defined as the ratio of number of photons emitted from a device to the number of injected charge carriers

$$\eta_{ext} = \frac{N_{ph}}{N_e}\,.$$

The number of photons we find from formula

$$N_{ph} = \frac{\Phi}{h\nu} = \frac{\lambda_{av}\Phi}{hc}\,,$$

while the number of electrons is equal to the current passing through a device, *I*, divided by the elementary charge

$$N_e = \frac{I}{e}.$$

In our experimental setup for detection the calibrated photodiode was used which means that the radiant flux was automatically integrated over all wavelengths. Therefore, in the formula for photons number we put the wavelength corresponding to the average energy of emitted photons.

In order to find the wavelength of the average energy of emitted photons we use a photodiode response plot presented below (figure B2). We will take an advantage of almost linear shape of the curve in the visible range and we assume that the response depends linearly on wavelength in the interesting for us spectral range.

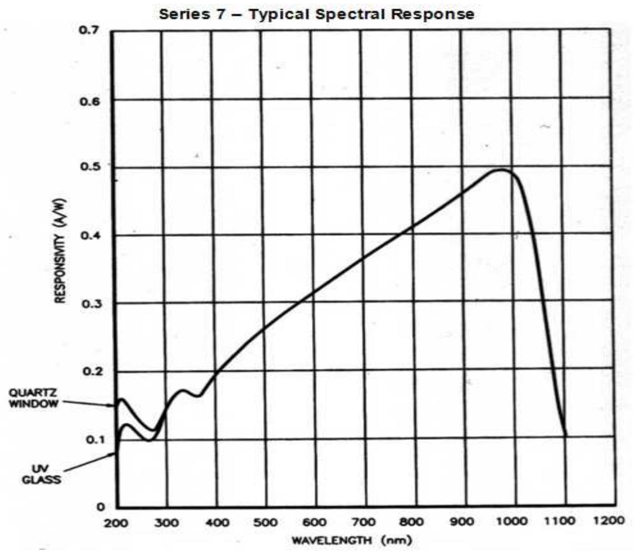

Figure B2. Spectral response of the photodiode used to measure light intensity

To find the average energy wavelength we divide intensity values of an EL spectrum by *hc/λ* for each wavelength and then we integrate the whole spectrum. Subsequently, we start integration of the division from the smallest value of wavelength until the integral value is equal to 1/2 of that for the whole spectrum. The wavelength for which it happens is the average energy wavelength of the spectrum. We assume here that a shape of an EL spectrum does not change with driving current which is usually the case for stable OLEDs.

The intensity of radiation is equal to the power registered by the photodiode P_{det} divided by the solid angle Ω (the photodiode is placed in the centre of the azimuthal axis and perpendicular to the emission direction of a device)

$$I_0 = \frac{P_{\mathrm{det}}}{\Omega}.$$

The power of radiation we can derive from the response function of the photodiode at the average energy of emission, R_{ph}, and the value of current generated in a detector I_{ph}

$$P_{\det} = \frac{I_{ph}}{R_{ph}}.$$

After substitutions we obtain formula for η_{ext}

$$\eta_{ext} = \frac{\pi\lambda_{av} e r^2 I_{ph}}{hcAIR_{ph}},$$

where we used for solid angle

$$\Omega = \frac{A}{r^2}.$$

In a special case when a detector is placed directly on the surface of a flat light source (r = 0), the power received by a photodiode is equal to the radiant flux of an OLED, *i.e.* $P_{\det} = \Phi$. In this case the formula for the external quantum efficiency simplifies to

$$\eta_{ext} = \frac{\lambda_{av} e I_{ph}}{hcIR_{ph}}.$$

At this point we give formulae employing photometric units describing radiation. We start from determination of the luminous flux Φ_v for a half-sphere of a lambertian source expressed as

$$\Phi_v[lm] = \pi I_v[sr \cdot cd],$$

where I_v is the luminous intensity expressed in general as

$$I_v[cd] = 683.002 \int_{380}^{780} \bar{y}(\lambda) I_0(\lambda) d\lambda,$$

with $\bar{y}(\lambda)$ being photopic response of the standard observer function. Using the average photon energy we can rewrite the formula as

$$I_v = 683.002\bar{y}(\lambda_{av}) I_0 = 683.002\bar{y}(\lambda_{av}) \frac{I_{ph} r^2}{R_{ph} A}.$$

For r = 0 the formula is as follows

$$I_v = 683.002\bar{y}(\lambda_{av}) \frac{I_{ph}}{\pi R_{ph}}.$$

Now we are ready to define the luminance L of a source from a distance r to a detector

$$L\left[\frac{cd}{m^2}\right]=\frac{I_v}{S}=\frac{683.002\,\overline{y}(\lambda_{av})I_{ph}r^2}{AR_{ph}S}$$

or

$$L\left[\frac{cd}{m^2}\right]=\frac{I_v}{S}=\frac{683.002\,\overline{y}(\lambda_{av})I_{ph}}{\pi R_{ph}S}$$

for a photodiode placed on the surface of a flat OLED source.

From the above we find the luminous efficacy η_l

$$\eta_l\left[\frac{cd}{A}\right]=\frac{LS}{I}$$

and the luminous power efficacy η_p, defined as the ratio of the luminous flux to the electrical power driving a device

$$\eta_p\left[\frac{lm}{W}\right]=\frac{\pi LS}{IU}=\frac{\pi\eta_{lc}}{U},$$

where U is the voltage applied to a diode.

13. REFERENCES

[1] A. B. Bernanose, M. Comte, P. Vouaux, *J. Chim. Physique* 50 (1953) 64 (in French)

[2] A. Bernanose, P. Vouaux, *J. Chim. Physique* 50 (1953) 261

[3] M. Pope, H. P. Kallmann, P. Magnante, *J. Chem. Phys*. 38 (1963) 2042

[4] W. Helfrich, W. G. Schneider, *Phys. Rev. Lett.* 14 (1965) 229

[5] C. W. Tang, S. A. VanSlyke, *Appl. Phys. Lett.* 51 (1987) 913

[6] C. W. Tang, S. A. VanSlyke, C. H. Chen, *J. Appl. Phys*. 65 (1989) 3610

[7] R. H. Partridge, *Polymer* 24 (1983) 733

[8] R. H. Partridge, *Polymer* 24 (1983) 739

[9] R. H. Partridge, *Polymer* 24 (1983) 748

[10] R. H. Partridge, *Polymer* 24 (1983) 755

[11] J. H. Burroughes, D. D. C. Bradley, A. R. Brown, R. N. Marks, K. Mackay, R. H. Friend, P. L. Burn, A. B. Holmes, *Nature* 347 (1990) 539

[12] J. Kido, K. Hongawa, K. Okuyama, K. Nagai, *Appl. Phys. Lett*. 64 (1994) 815

[13] M. A. Baldo, D. F. O'Brien, Y. You, A. Shostikov, S. Sibley, M. E. Thompson, S. R. Forrest, *Nature* 395 (1998) 151

[14] A. Endo, K. Sato, K. Yoshimura, T. Kai, A. Kawada, H. Miyazaki, C. Adachi, *Appl. Phys. Lett.* 98 (2011) 083302

[15] H. Uoyama, K. Goushi, K. Shizu, H. Nomura, C. Adachi, *Nature* 492 (2012) 234

[16] Y. Tao, K. Yuan, T. Chen, P. Xu, H. Li, R. Chen, C. Zheng, L. Zhang, W. Huang, *Adv. Mater*. 26 (2014) 7931

[17] S. Reineke, *Nature Photonics* 8 (2014) 269

[18] S. Zhang, L. Yao, Q. Peng, W. Li, Y. Pan, R. Xiao, Y. Gao, C. Gu, Z. Wang, P. Lu, F. Li, S. Su, B. Yang, Y. Ma, *Adv. Funct. Mater.* 25 (2015) 1755

[19] M. Flämmich, J. Frischeisen, D. S. Setz, D. Michaelis, B. C. Krummacher, T. D. Schmidt, W. Brütting, N. Danz, *Org. Electron*. 12 (2011) 1663

[20] K.-H. Kim, C.-K. Moon, J.-H. Lee, S.-Y. Kim, J.-J. Kim, *Adv. Mater*. 26 (2014) 3844

[21] J.-H. Jou, S. Kumar, A. Agrawal, T.-H. Li, S. Sahoo, *J. Mater. Chem. C* 3 (2015) 2974

[22] J.-i. Nishide, H. Nakanotani, Y. Hiraga, C. Adachi, *Appl. Phys. Lett.* 104 (2014) 233304

[23] T. Higuchi, H. Nakanotani, C. Adachi, *Adv. Mater.* 27 (2015) 2019

[24] M. Pfeiffer, "Controlled Doping of Organic Vacuum Deposited Dye Layers: Basics and Applications" PhD thesis, TU Dresden (1999)

[25] P. W. Atkins, R. S. Friedman, "Molecular Quantum Mechanics", Oxford University Press, 1997

[26] S. B. Nam, D. C. Reynolds, C. W. Litton, R. J. Almassy, T. C. Collins, C. M. Wolfe, *Phys. Rev. B* 13 (1976) 761

[27] J. Frenkel, *Phys. Rev.* 37 (1931) 17

[28] J. B. Birks, “Photophysics of aromatic molecules”, Wiley, 1970

[29] T. Förster, *Discuss. Faraday Soc.* 27 (1959) 7

[30] S. E. Braslavsky, E. Fron, H. B. Rodrìguez, E. San Romàn, G. D. Scholes, G. Schweitzer, B. Valeur, J. Wirz, *Photochem. Photobiol. Sci.* 7 (2008) 1444

[31] D. L. Dexter, *J. Chem. Phys.* 21 (1953) 836

[32] N. L. Vekshin, "Energy Transfer In Macromolecules", The Society of Photo-Optical Instrumentation Engineers, 1997

[33] G. Giro, M. Cocchi, J. Kalinowski, P. Di Marco, V. Fattori, *Chem. Phys. Lett*. 318 (2000) 137

[34] S. I. Weissman, *J. Chem. Phys*. 10 (1942) 214

[35] L. Onsager, *Phys. Rev.* 54 (1938) 554

[36] N. J. Turro, V. Ramamurthy, J. C. Scaiano, "Principles of molecular photochemistry. An introduction", University Science Books, 2009

[37] B. Dick, B. Nickel, *Chem. Phys.* 78 (1983) 1

[38] D. Y. Kondakov, T. D. Pawlik, T. K. Hatwar, J. P. Spindler, *J. Appl. Phys.* 106 (2009) 124510

[39] A. P. Monkman, *ISRN Materials Science*, vol. 2013, article ID 670130

[40] M. Pope, C. E. Swenberg, "Electronic Processes in Organic Crystals and Polymers", Oxford University Press, 1999

[41] J. Kalinowski, *J. Phys. D* 32 (1999) R179

[42] M. Pfeiffer, S. R. Forrest, K. Leo, M. E. Thompson, *Adv. Mater.* 14 (2002) 1633

[43] K. Walzer, B. Maenning, M. Pfeiffer, K. Leo, *Chem. Rev*. 107 (2007) 1233

[44] G. He, M. Pfeiffer, K. Leo, M. Hofmann, J. Birnstock, R. Pudzich, J. Salbeck, *Appl. Phys. Lett*. 85 (2004) 3911

[45] J. Kido, M. Kimura, K. Nagi, *Science* 267 (1995) 1332

[46] T. Tsutsui, M. Terai, *Appl. Phys. Lett.* 84 (2004) 440

[47] M. Terai, K. Fujita, T. Tsutsui, *Jpn. J. Appl. Phys.* 44 (2005) L1059

[48] M. Terai T. Tsutsui, *Appl. Phys. Lett.* 90 (2007) 083502

[49] M. C. Gather, A. Köhnen, A. Falcou, H. Becker, K. Meerholz, *Adv. Funct. Mater.* 17 (2007) 191

[50] http://en.wikipedia.org/wiki/Grassmann%27s_law_%28optics%29#cite_note-0

[51] T. W. Lee, T. Noh, B. K. Choi, M. S. Kim, D. W. Shin, J. Kido, *Appl. Phys. Lett.* 92 (2008) 043301

[52] M. C. Gather, S. Köber, S. Heun, K. Meerholz, *J. Appl. Phys.* 106 (2009) 24506

[53] H. J. Bolink, F. De Angelis, E. Baranoff, C. Klein, S. Fantacci, E. Coronado, M. Sessolo, K. Kalyanasundaram, M. Grätzel, K. Nazeeruddin, *Chem. Comm.* (2009) 4672

[54] S. Li, G. Zhong W. Zhu, F. Li, J. Pan, W. Huang, H. Tian, *J. Mater. Chem.* 15 (2005) 3221

[55] S. H. Kim, S. Park, J. E. Kwon, S. Y. Park, *Adv. Funct. Mater.* 21 (2011) 644

[56] U. Giovanella, W. Mróz, P. Foggi, P. Fabbrizzi, S. Cicchi, C. Botta, *ChemPhysChem* 11 (2010) 683

[57] J. Liu, Q. Zhou, Y. Cheng, Y. Geng, L. Wang, D. Ma, X. Jing, F. Wang, *Adv. Funct. Mater.* 16 (2006) 957

[58] D. A. Poulsen, B. J. Kim, B. Ma, C. S. Zonte, J. M. J. Frèchet, *Adv. Mater.* 22 (2010) 77

[59] J. Kalinowski, M. Cocchi, D. Virgili, V. Fattori, J. A. G. Williams, *Adv. Mater.* 19 (2007) 4000

[60] W. Mróz, C. Botta, U. Giovanella, E. Rossi, A. Colombo, C. Dragonetti, D. Roberto, R. Ugo, A. Valore, J. A. G. Williams, *J. Mater. Chem.* 21 (2011) 8653

[61] B. W. Jones, "Life in the Solar System and Beyond", Springer, 2004

[62] *International Lighting Vocabulary* CIE 017.4-1987, *ISBN 978 3 900734 07 7*

[63] D. B. Judd, *J. Opt. Soc. Am.* 25 (1935) 24

[64] D. L. MacAdam, *J. Opt. Soc. Am.* 27 (1937) 294

[65] C. S. McCamy, *Col. Res. & App.* 17 (1992) 142

[66] J. Hernàndez-Andrès, R. L. Lee, Jr., J. Romero, *Appl. Opt.* 38 (1999) 5703

[67] See Appendix A for the data

[68] T. Azuma, E. Barthès, H. D. Einhorn, M. Halstead, C. W. Jerome, J. de Kerf, J. Krtil, W. Münch, J. L. Ouweitjes, M. Richter, G. Siljeholm, CIE 13.3-1995

[69] J. Schanda, "COLORIMETRY: Understanding the CIE System", Wiley, 2007

[70] N. A. R. Robertson, "COLORIMETRY: Fundamentals and Applications", Wiley, 2005

[71] L. Qian, Y. Zheng, K. R. Choudhury, D. Bera, F. So, J. Xue, P. H. Holloway, *Nano Today* 5 (2010) 384

[72] M. A. Baldo, D. F. O'Brien, M. E. Thompson, S. R. Forrest, *Phys. Rev. B* 60 (1999) 14422

[73] M. Segal, M. A. Baldo, R. J. Holmes, S. R. Forrest, Z. G. Soos, *Phys. Rev. B* 68 (2003) 075211

[74] C. Adachi, M. A. Baldo, M. E. Thompson, S. R. Forrest, *J. Appl. Phys.* 90 (2001) 5048

[75] Y. Kawamura, K. Goushi, J. Brooks, J. J. Brown, H. Sasabe, C. Adachi, *Appl. Phys. Lett.* 86 (2005) 071104

[76] Y. Cao, I. D. Parker, G. Yu, C. Zhang, A. J. Heeger, *Nature* 397 (1999) 414

[77] Z. Shuai, D. Beljonne, R. J. Silbey, J. L. Brédas, *Phys. Rev. Lett.* 84 (2000) 131

[78] M. Wohlgenannt, K. Tandon, S. Mazumdar, S. Ramasesha, Z. V. Vardeny, *Nature* 409 (2001) 494

[79] J. S. Wilson, A. S. Dhoot, A. J. A. B. Seeley, M. S. Khan, A. Köhler, R. H. Friend, *Nature* 413 (2001) 828

[80] C.-G. Zhen, Z.-K. Chen, Q.-D. Liu, Y.-F. Dai, R. Y. C. Shin, S.-Y. Chang, J. Kieffer, *Adv. Mater.* 21 (2009) 2425

[81] C.-G. Zhen, Y.-F. Dai, W.-J. Zeng, Z. Ma, Z.-K. Chen, J. Kieffer, *Adv. Funct. Mater.* 21 (2011) 699

[82] K. Okumoto, H. Kanno, Y. Hamaa, H. Takahashi, K. Shibata, *Appl. Phys. Lett.* 89 (2006) 063504

[83] S. Nowy, J. Frischeisen, W. Brütting, *Proc. SPIE* 7415 (2009) 74151C

[84] H. K. Kim, S.-H. Cho, J. R. Oh, Y.-H. Lee, J.-H. Lee, J.-G. Lee, S.-K. Kim, Y.-I. Park, J.-W. Park, Y. R. Do, *Org. Electron.* 11 (2010) 137

[85] Y. Sun, S. R. Forrest, *Nature Photon.* 2 (2008) 483

[86] Y. R. Do, Y.-C. Kim, Y.-W. Song, Y.-H. Lee, *J. Appl. Phys.* 96 (2004) 7629

[87] K. Saxena, D. S. Mehta, V. K. Rai, R. Srivastava, G. Chauhan, M. N. Kamalasanan, *J. Lum.* 128 (2008) 525

[88] W. H. Koo, S. M. Jeong, F. Araoka, K. Ishikawa, S. Nishimura, T. Toyooka, H. Takezoe, *Nature Photon.* 4 (2010) 222

[89] Y. Sun, S. R. Forrest, *J. Appl. Phys.* 100 (2006) 073106

[90] F. Galeotti, W. Mróz, G. Scavia, C. Botta, *Org. Electron.* 14 (2013) 212

[91] J. H. Lambert, "Photometria", Bavarian State Library, 1765

[92] T. Tsutsui, N. Takada, S. Saito, E. Ogino, *Appl. Phys. Lett.* 65 (1994) 1868

[93] C. Fèry, B. Racine, D. Vaufrey, H. Doyeux, S. Cinà, *Appl. Phys. Lett.* 87 (2005) 213502

[94] F. So, D. Kondakov, *Adv. Mater.* 22 (2010) 3762

[95] T. Tsujimura, ‘‘OLED displays: fundamentals and applications’’, Wiley, 2012

[96] B. W. D’Andrade, S. R. Forrest, *Adv. Mater.* 16 (2004) 1585

[97] https://en.wikipedia.org/wiki/Luminous_efficacy

[98] https://en.wikipedia.org/wiki/List_of_light_sources

[99] S. Cicchi, P. Fabbrizzi, G. Ghini, A. Brandi, P. Foggi, A. Marcelli, R. Righini, C. Botta, *Chem. Eur. J.* 15 (2009) 754

[100] J. Mezyk, W. Mróz, A. Mech, U. Giovanella, F. Meinardi, C. Botta, B. Vercelli, R. Tubino, *Phys. Chem. Chem. Phys.* 11 (2009) 10152

[101] M. Montalti, A. Credi, L. Prodi, M. T. Gandolfi, "Handbook of Photochemistry", CRC Press, 2006

[102] J. R. Lakowicz, "Principles of Fluorescence Spectroscopy", Springer, 2006

[103] J. W. Eastman, *Photochem. Photobiol.* 6 (1967) 55

[104] M. Fischer, J. Georges, *Chem. Phys. Lett.* 260 (1996) 115

[105] J. A. G. Williams, A. Beeby, E. S. Davies, J. A. Weinstein, C. Wilson, *Inorg. Chem*. 42 (2003) 8609

[106] J. C. de Mello, H. F. Wittman, R. H. Friend, *Adv. Mater.* 9 (1997) 230

[107] F. M. Winnik, *Chem. Rev.* 93 (1993) 587

[108] G. Jones, V. I. Vullev, *J. Phys. Chem. A* 105 (2001) 6402

[109] H. Ephardt, P. Fromherz, *J. Phys. Chem.* 97 (1993) 4540

[110] H. Tong, Y. Dong, M. Häußler, Y. Hong, J. W. Y. Lam, H. H-Y. Sung, I. D. Williams, H. S. Kwok, B. Z. Tang, *Chem. Phys. Lett.* 428 (2006) 326

[111] P. Fromherz, *J. Phys. Chem.* 99 (1995) 7188

[112] A. K. Bhowmik, A. Dharmadhikari, M. Thakur, *Appl. Phys. Lett.* 79 (2001) 716

[113] C.-H. Yang, T.-F. Guo, I.-W. Sun, *J. Lum.* 124 (2007) 93

[114] L. Li , Z. Zhang , W. Long, A. Tong, *Spectrochimica Acta Part A* 56 (2001) 385

[115] Z.-X. Zhang, L.-D. Li, Y.-L. Wu, J.-M. Liu, *Luminescence* 20 (2005) 370

[116] X. Liu, J. K. Thomas, *Chem. Mater.* 6 (1994) 2303

[117] L. Qian, D. Bera, P. H. Holloway, *Appl. Phys. Lett.* 90 (2007) 103511

[118] H. Benten, J. Guo, H. Ohkita, S. Ito, M. Yamamoto, N. Sakumoto, K. Hori, Y. Tohda, K. Tani, *J. Phys. Chem. B* 111 (2007) 10905

[119] P. Furuta, J. Brooks, M. E. Thompson, J. M. J. Fréchet, *J. Am. Chem. Soc.* 125 (2003) 13165

[120] U. Giovanella, C. Botta, A. Papagni, R. Tubino, L. Miozzo, *Appl. Phys. Lett.* 87 (2005) 171910

[121] S. Reineke, K. Walzer, K. Leo, *Phys. Rev. B* 75 (2007) 125328

[122] M. F. Pepitone, G. G. Jernigan, J. S. Melinger, O.-K. Kim, *Org. Lett.* 9 (2007) 801

[123] L. Brauge, G. Vériot, G. Franc, R. Deloncle, A.-M. Caminade, J.-P. Majoral, *Tetrahedron* 62 (2006) 11891

[124] W. F. Sager, N. Filipescu, F. A. Serafin, *J. Phys. Chem*. 69 (1965) 1092

[125] N. S. Baek, M. K. Nah, Y. H. Kim, H. K. Kim, *J. Lum.* 127 (2007) 707

[126] S. Sato, M. Wada, *Bull. Chem. Soc. Jap.* 43 (1970) 1955

[127] X. Jiang, R. A. Register, K. A. Killeen, M. E. Thompson, F. Pschenitzka, T. R. Hebner, J. C. Sturm, *J. Appl. Phys*. 91 (2002) 6717

[128] P. de Sainte Claire, *J. Phys. Chem. B* 110 (2006) 7334

[129] M. Yokota, O. Tanimoto, *J. Phys. Soc. Jap.* 22 (1967) 779

[130] J. Mężyk, J. Kalinowski, F. Meinardi, R. Tubino, *Chem. Phys. Lett.* 395 (2004) 321

[131] R. R. Lunt, N. C. Giebink, A. A. Belak, J. B. Benziger, S. R. Forrest, *J. Appl. Phys.* 105 (2009) 053711

[132] S.-P. Yang, D. Huang, D.-Y. Ge, B.-Y. Liu, L.-S. Wang, G.-S. Fu, *Chin. Phys. Lett*. 28 (2011) 087101

[133] D. E. Markov, C. Tanase, P. W. M. Blom, J. Wildeman, *Phys. Rev. B* 72 (2005) 045217

[134] R. C. Powell, Z. G. Soos, *J. Lum*. 11 (1975) 1

[135] S. J. Farley, D. L. Rochester, A. L. Thompson, J. A. K. Howard, J. A. G. Williams, *Inorg. Chem*. 44 (2005) 9690

[136] A. F. Rausch, L. Murphy, J. A. G. Williams, H. Yersin, *Inorg. Chem*. 48 (2009) 11407

[137] W. Mróz, K. Falkowski, M. Miśnik, E. Rossi, M. Balordi, W. Stampor, *Org. Electron*. 14 (2013) 2880

[138] M. Cocchi, J. Kalinowski, V. Fattori, J. A. G. Williams, L. Murphy, *Appl. Phys. Lett*., 94 (2009) 073309

[139] W.-C. Chang, A. T. Hu, J.-P. Duan, D. K. Rayabarapu, C.-H. Cheng, *J. Organometallic Chem*. 689 (2004) 4882

[140] T. Sajoto, P. I. Djurovich, A. Tamayo, M. Yousufuddin, R. Bau, M. E. Thompson, *Inorg. Chem*. 44 (2005) 7992

[141] W. Mróz, R. Ragni, F. Galeotti, E. Mesto, C. Botta, L. De Cola, G. M. Farinola, U. Giovanella, *J. Mater. Chem. C* 3 (2015) 7506

[142] F. Babudri, G. M. Farinola, F. Naso, R. Ragni, *Chem. Commun*. (2007) 1003

[143] D. L. Rochester, S. Develay, S. Záliš, J. A. G. Williams, *Dalton Trans*. (2009) 1728

[144] W. Sotoyama, T. Satoh, H. Sato, A. Matsuura, N. Sawatari, *J. Phys. Chem. A* 109 (2005) 9760

[145] W. Holzer, A. Penzkofer, T. Tsuboi, *Chem. Phys*. 308 (2005) 93

[146] F. C. Bos, D. M. Burland, *Phys. Rev. Lett*. 58 (1987) 152

[147] U. Giovanella, P. Betti, C. Botta, S. Destri, J. Moreau, M. Pasini, W. Porzio, B. Vercelli, A. Bolognesi, *Chem. Mater*. 23 (2011) 810

[148] S. Nowy, N. A. Reinke, J. Frischeisen, W. Brüttig, *Proc. SPIE* 6999 (2008) 69992V

[149] M. A. Baldo, C. Adachi, S. R. Forrest, *Phys. Rev. B* 62 (2000) 10967

[150] J. Kalinowski, W. Stampor, J. Mężyk, M. Cocchi, D. Virgili, V. Fattori, P. Di Marco, *Phys. Rev. B* 66 (2002) 235321

[151] C. Murawski, K. Leo, M. C. Gather, *Adv. Mater*. 25 (2013) 6801

[152] M. Cocchi, D. Virgili, V. Fattori, D. L. Rochester, J. A. G. Williams, *Adv. Funct. Mater*. 17 (2007) 285

[153] G. D. Batema, M. Lutz, A. L. Spek, C. A. van Walree, C. de Mello Donegá, A. Meijerink, R. W. A. Havenith, J. Pérez-Moreno, K. Clays, M. Büchel, A. van Dijken, D. L. Bryce, G. P. M. van Klink, G. van Koten, *Organometallics* 27 (2008) 1690

[154] T. Ye, J. Chen, D. Ma, *Phys. Chem. Chem. Phys*. 12 (2010) 15410

[155] D. M. Pai, J. F. Yanus, M. Stolka, *J. Phys. Chem*. 88 (1984) 4714

[156] A. W. Grice, D. D. C. Bradley, M. T. Bernis, M. Inbasekaran, W. W. Wu, E. P. Woo, *Appl. Phys. Lett*. 73 (1998) 629

[157] M. Redecker, D. D. C. Bradley, M. Inbasekaran, E. P. Woo, *Appl. Phys. Lett*. 73 (1998) 1565

[158] A. J. Cadby, P. A. Lane, H. Mellor, S. J. Martin, M. Grell, C. Giebeler, D. D. C. Bradley, M. Wohlgenannt, C. An, Z. V. Vardeny, *Phys. Rev. B* 62 (2000) 15604

[159] M. Grell, D. D. C. Bradley, X. Long, T. Chamberlain, M. Inbasekaran, E. P. Woo, M. Soliman, *Acta Polym*. 49 (1998) 439